5-2012

Improved Techniques For Acquisition And Analysis Of Dynamic Contrast-Enhanced Magnetic Resonance Imaging For Detecting Vascular Permeability In The Central Nervous System

Cheukkai Hui

The TMC LIBRARY
Health Sciences Resource Center

IMPROVED TECHNIQUES FOR ACQUISITION AND ANALYSIS OF DYNAMIC CONTRAST-

ENHANCED MAGNETIC RESONANCE IMAGING FOR DETECTING VASCULAR

PERMEABILITY IN THE CENTRAL NERVOUS SYSTEM

by

Cheukkai Becket Hui, M.A., B.S.

APPROVED:

_____

Supervisory Professor, Ponnada A. Narayana, Ph.D.

_____

Khader M. Hasan, Ph.D.

_____

F. Gerard Moeller, M.D.

_____

R. Jason Stafford, Ph.D.

_____

Richard E. Wendt, III, Ph.D.

APPROVED:

_____

Dean, The University of Texas

Graduate School of Biomedical Sciences at Houston

IMPROVED TECHNIQUES FOR ACQUISITION AND ANALYSIS OF DYNAMIC CONTRAST-

ENHANCED MAGNETIC RESONANCE IMAGING FOR DETECTING VASCULAR

PERMEABILITY IN THE CENTRAL NERVOUS SYSTEM

A

DISSERTATION

Presented to the Faculty of

The University of Texas

Health Science Center at Houston

and

The University of Texas

M. D. Anderson Cancer Center

Graduate School of Biomedical Sciences

in Partial Fulfillment

of the Requirements

for the Degree of

DOCTOR OF PHILOSOPHY

by

Cheukkai Becket Hui, M.A., B.S.

Houston Texas

May 2012

Acknowledgements

IMPROVED TECHNIQUES FOR ACQUISITION AND ANALYSIS OF DYNAMIC CONTRAST-ENHANCED MAGNETIC RESONANCE IMAGING FOR DETECTING VASCULAR PERMEABILITY IN THE CENTRAL NERVOUS SYSTEM

Publication No._____

Cheukkai Becket Hui, M.A., B.S.

Supervisory Professor, Ponnada A. Narayana, Ph.D.

Dynamic contrast-enhanced magnetic resonance imaging (DCE-MRI) is a noninvasive technique for quantitative assessment of the integrity of blood-brain barrier and blood-spinal cord barrier (BSCB) in the presence of central nervous system pathologies. However, the results of DCE-MRI show substantial variability. The high variability can be caused by a number of factors including inaccurate T_1 estimation, insufficient temporal resolution and poor contrast-to-noise ratio. My thesis work is to develop improved methods to reduce the variability of DCE-MRI results. To obtain fast and accurate T_1 map, the Look-Locker acquisition technique was implemented with a novel and truly centric k-space segmentation scheme. In addition, an original multi-step curve fitting procedure was developed to increase the accuracy of T_1 estimation. A view sharing acquisition method was implemented to increase temporal resolution, and a novel normalization method was introduced to reduce image artifacts. Finally, a new clustering algorithm was developed to reduce apparent noise in the DCE-MRI data. The performance of these proposed methods was verified by simulations and phantom studies. As part of this work, the proposed techniques were applied to an in vivo DCE-MRI study of experimental spinal cord injury (SCI). These methods have shown robust results and allow quantitative assessment of regions with very low vascular permeability. In conclusion, applications of the improved DCE-MRI acquisition and analysis methods developed in this thesis work can improve the accuracy of the DCE-MRI results.

Table of Contents

List of Figures

List of Tables

List of Abbreviations

acqtp	Acquisition time point
AFI	Actual flip angle imaging
AIF	Arterial input function
B_1	Radio frequency Field
BBB	Blood-brain barrier
BLAST	Broad-use linear acquisition speed-up technique
BSCB	Blood-spinal cord barrier
CNR	Contrast-to-noise ratio
CNS	Central nervous system
CPA	Curve pattern analysis
CSF	Cerebrospinal fluid
CV	Coefficient of variation
DCE-MRI	Dynamic contrast-enhanced MRI
DPSS	Discrete prolate spheroidal sequences
EES	Extravascular extracellular space
FA	Fractional anisotropy
FOV	Field-of-view
Gd	Gadolinium
GM	Gray matter
IRSE	Inversion recovery spin echo
MRI	Magnetic resonance imaging
RF	Radio frequency
RMS	Root mean square
ROI	Region of interest
SNR	Signal-to-noise ratio
SPGR	Spoiled gradient echo
T_1	Spin-lattice relaxation time
T_2	Spin-spin relaxation time
T7	Thoracic level 7
TE	Echo time
TI	Inversion time
TR	Repetition time
TRICKS	Time-resolved imaging of contrast kinetics

VFA   Variable flip angle

WM   White matter

CHAPTER 1

INTRODUCTION

1.1 Motivations

Dynamic contrast-enhanced magnetic resonance imaging (DCE-MRI) is a MRI technique to investigate the vascular structure and function. The current applications of DCE-MRI include cancer imaging [1,2], angiogenesis study [3,4], and inflammatory pathology that affects the blood-brain barrier (BBB) [5-7] and blood-spinal cord barrier (BSCB) [8,9]. Compared to other medical imaging modalities, DCE-MRI has the advantage of good spatial resolution and is free from ionizing radiation. The most common contrast agent in DCE-MRI is the gadolinium (Gd)-labeled tracer. Gd is paramagnetic and can interact with nearby water protons to reduce the spin-lattice relaxation time (T_1) of neighboring tissue. DCE-MRI can provide quantitative information of the micro-vascular permeability. Following administration of the Gd tracer, a series of T_1-weighted images are acquired repeatedly. The change of tracer concentration as a function of time is computed from the T_1-weighted images. By applying appropriate pharmacokinetic model to the dynamics of tracer concentration, the transfer rates of Gd tracer can be estimated as a quantitative measure of the vascular permeability.

However, substantial variability in the pharmacokinetic parameters has been observed in DCE-MRI analyses [10-12]. The variability is worse in the central nervous system (CNS) because the presence of BBB and BSCB prevent Gd tracer from entering the parenchymal tissue. This leads to relatively small increase in intensity and can aggravate the inconsistency in the DCE-MRI results. The main purpose of this thesis work is to point out some of the weaknesses in the acquisition and analysis of DCE-MRI; and develop new methods to overcome some of these limitations to improve accuracy of the results. This leads to the following central objective:

Central Objective

Develop improved acquisition and analysis techniques of DCE-MRI for detecting micro-vascular permeability in the CNS as a result of pathology. These improved techniques should enhance the data quality and the accuracy of the DCE-MRI results.

1.2 Specific Aims

The specific aims to achieve my central objective are listed below:

Implement an improved 3D Look-Locker sequence and develop a multi-step curve fitting procedure to acquire accurate T_1 map. T_1 value is a necessary parameter to compute tracer concentration from the DCE-MRI images. Fast and accurate T_1 mapping technique can therefore improve the DCE-MRI results.

Implement 3D view-sharing acquisition and reconstruct the images using a novel normalization factor to acquire rapid T_1 weighted images in dynamic contrast-enhanced MRI. Insufficient temporal resolution can lead to inconsistent DCE-MRI results. View sharing acquisition can increase the temporal resolution of the DCE-MRI images.

Develop a local search clustering algorithm that groups similar concentration-time curves into clusters for reducing apparent noise and enhancing the accuracy of dynamic contrast-enhanced MRI parameters. The voxel-by-voxel analysis that is commonly employed in the DCE-MRI analysis is susceptible to noise and could lead to spurious results. Suitable clustering technique can reduce apparent noise without losing inherent heterogeneity of permeability within the tissue.

Apply the improved dynamic contrast-enhanced MRI techniques to study the permeability of blood-spinal cord barrier in experimental spinal cord injury. Compromise BSCB is one of the secondary pathologies of spinal cord injury. The role of BSCB in experimental spinal cord injury is a major area of research in our laboratory.

1.3 Background

1.3.1 Two-Compartment Tracer Kinetic Model

The most commonly used tracer kinetic model in the DCE-MRI analysis is the two-compartment Kety model [13,14]. This model is based on the Gd tracer leakage from the vasculature into the extravascular extracellular space (EES). This tracer influx rate between the blood plasma and EES is determined by the transfer constant K^{trans}. The tracer can flow from the EES back to the vasculature. The tracer flux rate between the EES and the blood plasma is the rate constant k_{ep}. The transfer constant K^{trans} is the amount of influx tracer per unit time, whereas the rate constant k_{ep} is the amount of out-flow tracer per unit time divided by the EES fractional volume v_e. The two-compartment model is depicted in Fig. 1.1.

Based on the two-compartment model, the change in tracer concentration in the tissue, C_{tis} can be described by the following equation:

$$\frac{dC_{tis}}{dt} = K^{trans}C_{pl} - k_{ep}C_{tis} \tag{1.1}$$

In this differential equation, the tracer concentration in the plasma, C_{pl} serves as a source function of tracer. The solution of Eq. 1.1 is expressed as:

$$C_{tis}(t) = K^{trans} \int_0^t e^{-k_{ep}(t-t')}C_{pl}(t')dt' \tag{1.2}$$

By determining the tracer concentration-time course, $C_{tis}(t)$ from the DCE-MRI data, the pharmacokinetic parameters can be estimated by fitting Eq. 1.2 to the data.
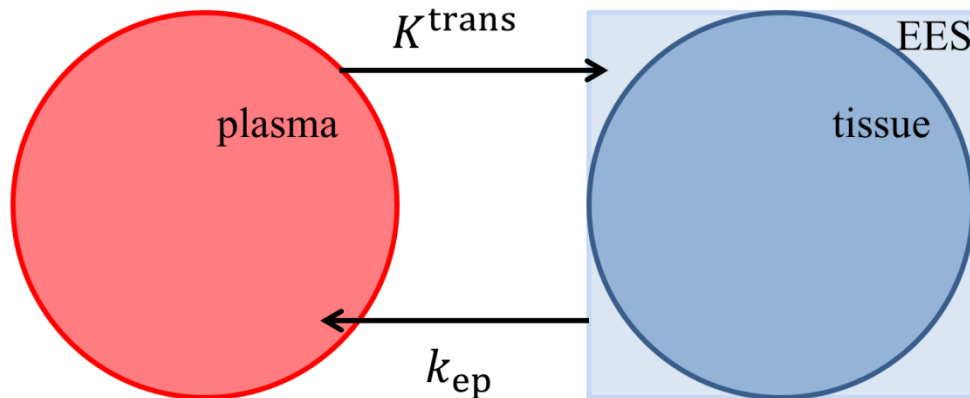
Figure 1.1 Two-compartment pharmacokinetic model that describes the dynamics of tracer concentration. The tracer can flow between the plasma and the EES of tissue at the rates K^{trans} and k_{ep}.

1.3.2 Pre-Contrast T_1 measurement in DCE-MRI

DCE-MRI studies exploit the reduction in the T_1 relaxation time as a result of the leakage of the contrast agent into the parenchyma. Therefore, DCE-MRI involves acquisition of T_1-weighted images. Spoiled gradient echo (SPGR) sequence is commonly used to acquire the T_1-weighted images in the DCE-MRI protocol. Under steady state condition, the signal, S acquired with SPGR sequence can be expressed as:

$$S = k_S \frac{1 - e^{-\text{TR}/T_1}}{1 - \cos \alpha \, e^{-\text{TR}/T_1}} \sin \alpha \, e^{-\text{TE}/T_2} \tag{1.3}$$

where TR and TE are the repetition and echo times, α is the flip angle, T_2 is the spin-spin or transverse relaxation time, and k_S is a weighting constant. Since $\text{TE} \ll T_2$, the last exponential term in Eq. 1.3 is considered to be unity. Assuming $\text{TR} \ll T_1$, under first order approximation, Eq. 1.3 can be written as:

$$S \cong k_S \frac{\sin \alpha}{1 - \cos \alpha} \left(\frac{\text{TR}}{T_1}\right) = k_C (R_1 \cdot \text{TR}) \tag{1.4}$$

where $R_1 = 1/T_1$ is the T_1 relaxation rate. After tracer administration, the T_1 value is reduced. Conversely, R_1 is increased by the paramagnetic Gd and the change in R_1 can be approximated by the following equation:

$$\Delta R_1 \cong \Delta r1_\rho \cdot C_{\text{Gd}} \tag{1.5}$$

C_{Gd} is the tracer concentration and $\Delta r1_\rho$ is the change in T_1 relaxation rate per unit tracer concentration. In the presence of tracer, the change in the post-contrast signal from the pre-contrast signal can be approximated as:

$$\Delta S \cong k_C \left(\Delta r_{1,\rho} \cdot C_{\text{Gd}} \cdot \text{TR}\right) \tag{1.6}$$

Let $T_{1,0}$ be the intrinsic relaxation time and S_0 the pre-contrast signal. The tracer concentration at time t after tracer administration can then be calculated from Eq. 1.6 and Eq. 1.4:

$$C_{\text{Gd}}(t) \cong \frac{1}{\Delta r_{1,\rho} \cdot T_{1,0}} \left(\frac{S(t) - S_0}{S_0}\right) \tag{1.7}$$

Therefore, measurement of tracer concentration requires calculating the fractional change in the signal following tracer administration, the change in T_1 relaxation rate per tracer concentration $\Delta r_{1,\rho}$ and the intrinsic $T_{1,0}$. Generally, $\Delta r_{1,\rho}$ is assumed to be constant within the range of anatomical T_1 values and can be determined in a separate study. However, $T_{1,0}$ values are considerably different among different tissue types and different pathologies. Applying a universal $T_{1,0}$ to Eq. 1.7 is therefore inappropriate and can lead to incorrect tracer concentration measurement. For this reason, the concurrent intrinsic T_1 map is essential to obtain accurate tracer concentration for quantitative DCE-MRI.

1.3.3 Extended DCE-MRI Model

In earlier studies, it was assumed that the change of signal was only due to the tracer in the EES and that the intravascular tracer had no contribution [14,15]. In reality, the signal change arises from Gd tracer in both the EES and the capillaries. Within any region of interest (ROI), the tracer concentration is composed of the tissue component and the blood component:

$$\left((1 - f_b) \cdot C_{tis}(t) + f_b \cdot C_b(t)\right) \cong \frac{1}{\Delta r_{1,\rho} \cdot T_{1,0}} \left(\frac{S(t) - S_0}{S_0}\right) \tag{1.8}$$

where $C_{tis}(t)$ and $C_b(t)$ are the tracer concentration in the tissue and in blood. f_b is the proton fraction of blood in the ROI in which:

$$f_b = \frac{v_b \cdot \rho_b^0}{(1 - v_b) \cdot \rho_{tis}^0 + v_b \cdot \rho_b^0} \tag{1.9}$$

v_b is the fractional volume of plasma in the ROI, and ρ_{tis}^0 and ρ_b^0 are the inherent proton densities of tissue and blood respectively.

Eq. 1.8 is mathematically identical to the formula described in some studies [16,17] in which the concentration $C_{Gd}(t)$ was modified as follow:

$$C_{Gd}(t) = (1 - v_b) \cdot C_{tis}(t) + v_b \cdot C_b(t) \tag{1.10}$$

According to this model, however, Gd tracer is not separated into compartments within the ROI. This would imply that tracer confined in the vessel can also affect the tissue relaxation. This would violate the two-compartment model. Therefore, using the plasma volume fraction v_b as included in Eq. 1.10 is incorrect. The plasma proton fraction f_b as in Eq. 1.8 will be used hereafter in this work instead.

Combining Eq. 1.2 and Eq. 1.8, the pharmacokinetic parameters can be computed by fitting the following equation to the DCE-MRI data with three parameters: K^{trans}, k_{ep} and f_b.

$$\frac{S(t) - S_0}{S_0} = \Delta r_{1,\rho} \cdot T_{1,0} \cdot \left(f_b \cdot C_b(t) + (1 - f_b) \cdot K^{trans} \int_0^t e^{-k_{ep}(t-t')} C_{pl}(t') dt'\right) \tag{1.11}$$

1.3.4 Variability in DCE-MRI Analysis

It has been demonstrated that the estimated pharmacokinetic parameters show considerable variations. A study by Buckley found systematic errors in the estimated K^{trans} and f_b using three different pharmacokinetic models [10]. In clinical studies, large within-patient variance of the K^{trans} and k_{ep} estimates was observed in different tumor types and in normal tissues [11,18]. In addition to the uncertainty from the multi-parameter nonlinear curve fitting employed in DCE-MRI, insufficient temporal resolution and low signal-to-noise ratio (SNR) are both considered to be factors in the observed high variability.

Previous studies have shown temporal resolution can have large effect on the accuracy of the estimation [19-21]. The estimation error is sensitive to the temporal resolution because of the rapid change in image enhancement following tracer administration. To improve curve fitting accuracy, it is necessary to maximize the sampling rate of the DCE-MRI acquisition.

Image acquisition in DCE-MRI usually employs very short TR to reduce the acquisition time. This however will reduce the SNR of the images. The situation is worse in CNS imaging where the intensity change is expected to be low because of the presence of barrier. The combination of low SNR and small signal change will further impair the accuracy of the estimated parameters. Consequently, reducing the noise of DCE-MRI data is essential for accurate estimation of pharmacokinetic parameters.

1.3.5 Spinal Cord Injury

SCI is the traumatic insult to the spinal cord and is a major health problem both in the USA and worldwide. Compromised BSCB integrity is observed during the secondary phase of the SCI that occurs subsequent to the initial traumatic insult [9,22,23]. The compromised BSCB increases transportation of substances from the vasculature to the spinal cord microenvironment. These substances may include potentially harmful molecules and cells that have adverse effects on the spinal cord. It is important to study the spatial and temporal extent of the BSCB permeability after SCI for proper patient management. DCE-MRI is the preferred modality to investigate the permeability of BSCB because it is minimally invasive. Improvement in the DCE-MRI analysis can enhance our understanding of the role of BSCB compromise on the evolution of secondary injury.

1.4 Methods and Materials

        The focus of this thesis work is on techniques development of DCE-MRI as well as its in vivo application. The techniques include MRI pulse sequence programming and developing software routines for various data analyses. These methods were verified by simulations and MRI studies on both phantoms and animals. All MRI protocols were performed on a USR70/30 horizontal bore 7T MR scanner (Bruker BioSpin, Karlsruhe, Germany). MRI pulse sequences were implemented on the ParaVision 5.1 software package (Bruker BioSpin, Karlsruhe, Germany). Data processing and computer simulations were written in IDL 8.1 (ITT Visual Information Solutions, Boulder, CO). Curve fitting procedures were performed using the MPFIT routines [24].

CHAPTER 2

IMPROVED LOOK-LOCKER ACQUISITION SCHEME AND CURVE FITTING PROCEDURE FOR T$_1$ ESTIMATION

2.1 Introduction

The T_1 relaxation time is one of the most fundamental parameters in MRI. The accurate measurement of T_1 is particularly important in various quantitative MRI techniques, including arterial spin labeling for perfusion assessments and DCE-MRI for determination of micro-vascular permeability. As described in Eq. 1.7, calculation of the tracer concentration requires the intrinsic T_1 value. Therefore, it is necessary to include T_1 map acquisition in each DCE-MRI protocol.

Traditionally, T_1 map is generated through the inversion recovery spin echo (IRSE) method. In this method, after the inversion pulse, spin echo signal is acquired at different inversion times (TI) to sample the magnetization recovery. And the IRSE is considered to be the gold standard for T_1 measurement [25]. However, T_1 measurement based on IRSE involves long scan time and is generally impractical for in vivo study. Different methods have been proposed to accelerate T_1 measurement and can be divided into two approaches: 1) excitation using variable flip angles [26] and 2) fast sampling of the inversion recovery curve [27].

The variable flip angle (VFA) method requires a set of SPGR images acquired with a minimum of two different flip angles. Because short TR is employed during SPGR acquisition, VFA method can significantly reduce the acquisition time compared to the IRSE sequence. However, the uncertainty in the flip angle due to the radio frequency field (B_1) inhomogeneity results in significant error to the T_1 estimation [28,29]. To accommodate the effect of B_1 inhomogeneity, a separate B_1 map acquisition is usually required. In addition, the choice of flip angles can also impact the accuracy of T_1 measurement in VFA [30,31].

The Look-Locker [32] technique is a widely used fast T_1 mapping method. In this method, the inversion recovery data are acquired by continuously sampling the recovering magnetization using very small flip angle following spin inversion. The continuous data sampling can significantly reduce acquisition time. Multi-slice 2D LL acquisition [33-35] has the time advantage over 3D LL acquisition but suffers from low SNR and unwanted cross-talk. In order to reduce the acquisition time of 3D imaging, Henderson et al. [36] presented a 3D LL method that is as time efficient as the 2D LL sequence [37]. Many variants have since been proposed to improve the quality of 3D LL T_1 mapping [31,37-40]. Conventional 3D LL encoding scheme is centrically segmented along one phase encoding direction. However, 1D centric segmentation is not optimal and can introduce reconstruction artifacts that degrade the accuracy T_1 measurements.

One of the uncertainties associated with LL T_1 estimation arises from the B_1 inhomogeneity. If the transmitted radio frequency (RF) angles are different from the ones applied to curve fitting, the final T_1 estimation will be incorrect. Some studies [33,34] have suggested obtaining the actual flip angle map by multi-parameter curve fitting to the LL data. Then, the flip angle map is smoothed by simple averaging. The smoothed angle is considered to be the actual angle and is applied to the final curve

fitting. This method however fails to remove the incorrect angles and these false angles can still affect the accuracy of the results.

To reduce the reconstruction artifacts during Look-Locker acquisition, I propose to modify the 3D LL acquisition so that the k-space segmentation is centric encoded along both phase encoding directions. I also propose a multi-step curve fitting algorithm in which the RF angles are smoothed and filtered based on the χ^2 weighting. This procedure can help remove the incorrect angles from entering the final curve fitting and can improve the accuracy of T_1 mapping.

2.2 Innovations

2.2.1 3D Look-Locker Elliptical Centric Segmentation Scheme

In the 3D LL acquisition, an inversion pulse is first applied to invert the longitudinal magnetization. A train of small flip angle RF pulses are then applied to collect SPGR images continuously during the magnetization recovery. However, because different k-space lines are sampled at different magnetization states, artifacts will occur in the reconstructed signal. Traditionally, the k_y lines for a given k_z are centrically acquired to reduce the reconstruction artifacts but that is not optimal. It has been demonstrated that elliptical centric encoding segmentation can produce images superior to those obtained from single direction centric encoding segmentation [41]. Therefore, I implemented the elliptical centric segmentation in 3D LL acquisition to minimize reconstruction artifacts.

Fig. 2.1 illustrates the proposed 3D LL pulse sequence. The k-space is scanned in multiple shots. After each inversion pulse, multiple lines (N_{TL}) in k-space and the entire set of time points (N_{time}) are acquired. k-space lines within one shot are acquired one after another from the center toward the periphery of k-space. Acquisition is then followed by the same group of k-space lines at the next time point, so on and so forth. Comparison between the traditional LL acquisition scheme and the elliptical
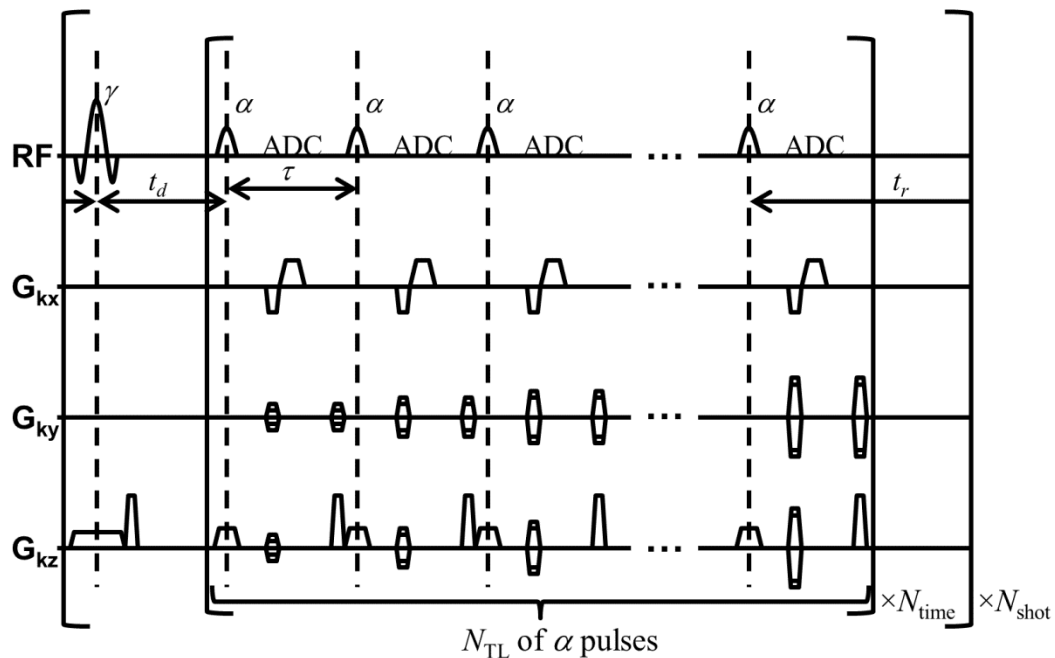
Figure 2.1 Schematic diagram of the 3D LL sequence. The acquisition is divided into multiple shots. Within each shot (external bracket), N_{TL} of k-space lines are sampled at each time point (internal bracket). During reconstruction, all k-space lines within the internal bracket form a single image.
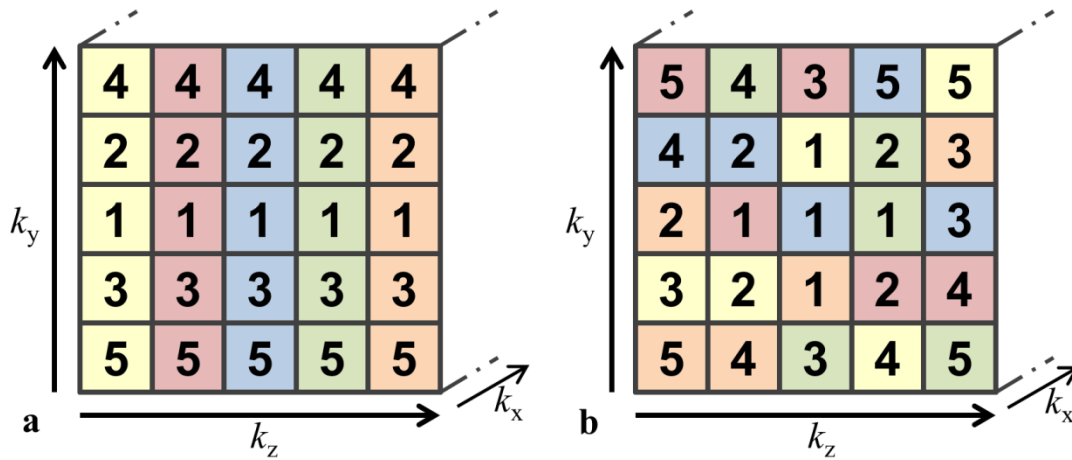
Figure 2.2 Examples of different k-space segmentation schemes in the LL sequence. k_y and k_z are the two phase encoding directions whereas k_x is the fully sampled frequency encoding direction. The different background colors represent different shots i.e. data with the same background are acquired after the same inversion pulse. The numbers represent the order in which they are acquired within the shot. The acquisition time point at which data 1 are taken is assigned as the effective acquisition time point of the reconstructed signal. a) The traditional centric acquisition scheme is limited to k_y centric encoding only. b) The proposed centric encoding scheme ensures that the center most data in both k_y and k_z are all acquired at the same acquisition time point.

centric acquisition scheme is shown in Fig. 2.2. Since an image from LL acquisition is composed of k-space data acquired at different acquisition time points (acqtp), the choice of the effective acqtp of the image is important in the curve fitting procedure. Since the center of k-space contributes most to the signal intensity, the acqtp where the center of k-space is sampled (i.e. $\text{acqtp} = \{1, N_{TL} + 1, 2N_{TL} + 1 \dots \}$) is assigned as the effective acqtp of the reconstructed image. Comparing the two segmentation methods, the elliptical segmentation ensures k-space data at the most central will have the same acqtp and thus will improve curve fitting accuracy.

Assuming perfect spoiling of the transverse magnetization and that the acquisition has reached steady state, the transverse magnetization at acqtp n of a LL acquisition can be derived and expressed as follow:

$$
M_\perp(n) = \sin \alpha \, M_0 \left\{ \frac{F_E(1 - F_1)}{F_0} \right.
$$
$$
+ \frac{F_1}{(1 - \cos \gamma \cos \alpha \, EdErF_2)} \left[1 - (1 - \cos \gamma)Ed - \cos \gamma \, EdEr \right.
$$
$$
\left. \left. + \frac{\cos \gamma \cos \alpha \, EdErF_E(1 - F_2)}{F_0} \right] \right\}
\tag{2.1}
$$

where

$$E\tau = \exp(-\tau/T_1)$$
$$Ed = \exp(-t_d/T_1)$$
$$Er = \exp(-t_r/T_1)$$
$$F_0 = 1 - \cos\alpha \cdot E\tau$$
$$F_1 = (\cos\alpha \cdot E\tau)^{n-1}$$
$$F_2 = (\cos\alpha \cdot E\tau)^{N_{tot}-1}$$
$$F_E = 1 - E\tau$$

α and γ are the flip and inversion angles respectively and M_0 is the equilibrium magnetization. The delay time τ, t_d and t_r are defined in Fig. 2.1. The derivation of Eq. 2.1 is presented in the Appendix.

2.2.2 Multi-Step Curve Fitting Procedure with Chi-Square Weighted Angle Map Filtering

The T_1 values can be estimated by fitting the LL data in Eq. 2.1 with only M_0 and T_1, provided that the RF angles are known. However, the actual RF pulse angles are not necessarily the same as the prescribed angles. In addition, the flip angles show spatial dependence because of B_1 inhomogeneity. Incorrect angles can lead to inaccuracy in the estimated T_1 values. Curve fitting using four parameters α, γ, M_0 and T_1 can take into account the variation in the actual angles. However, the increased number of parameters in the curve fitting makes it very sensitive to data fluctuation and can also produce incorrect T_1. To solve this problem, I developed a multi-step curve fitting method that uses the χ^2 weighting to remove the incorrect angle estimates.

First, a four-parameter fit is used on a coarse resolution image series (e.g. $4\times4\times4$-voxel average) to obtain the initial α and γ maps. Since both angles are expected to vary smoothly, the use of coarse resolution is justified. Assuming that the correct angle estimates can produce better fit to the curve, the angle that yields high χ^2 is likely to be incorrect and should be removed; whereas angle that yields low χ^2 should be weighted more. Therefore, the angle maps are averaged and filtered based on their respective χ^2 weightings of the fit. The angle in each voxel is computed within an averaging kernel using the following equation:

$$\angle = \left\{ \frac{\sum_i (2.0\bar{E} - E_i)\angle_i}{\sum_i (2.0\bar{E} - E_i)} \middle| E_i < 2.0\bar{E} \right\} \tag{2.2}$$

where

$$E_i = \bar{\sigma}_i\sqrt{\chi_i^2}$$

χ_i^2 represents the weighting of the fit in region i, $\bar{\sigma}_i$ is the average standard deviation of the corresponding signals. $\bar{E}$ is the mean of all E_j within the kernel. Instead of directly using χ_i^2, the

modified form E_i is used to remove the contribution from the signal standard deviation. This is because the signal standard deviation is mostly a result of different tissue types as the averaging kernel is composed of multiple voxels. The signal standard deviation has relatively small influence on the curve fitting accuracy but can change the χ^2 value dramatically and therefore should be removed. The summation only includes non-zero angles that have its corresponding E_i below $2.0\bar{E}$. Generally, about 5% of data can be considered to be spurious statistically. The factor 2.0 was chosen because it was found empirically that about 7% of angles would be discarded with this factor. The maps of the angles are further smoothed with a median filter (e.g. $5 \times 5 \times 5$ kernel) to further remove any unphysical fluctuation. Using the smoothed α and γ maps as the actual angle maps, the final full resolution T_1 map is calculated using the two-parameter curve fit with M_0 and T_1.

2.3 Methods and Materials

2.3.1 Simulations

A 3D digital image with $64 \times 64 \times 64$ voxels was created to investigate the effectiveness of the proposed LL modifications. The image was composed of structures with four basic shapes and each structure is assigned a unique T1 value: a sphere (800 msec), a cube (1000 msec), a cylinder (2800 msec) and an ellipsoid (1200 msec). The T_1 value in each voxel was then randomized with a Gaussian distribution with a standard deviation of 100 msec. In addition, each of the four structures has a different magnitude to create edges between them. The T1 map of the 3D image is depicted in Fig. 2.3a.

The evolution of magnetization during a LL acquisition was simulated using Eq. 2.1 with the following parameters: $\tau = 8$ msec, $t_d = 10$ msec, $t_r = 1000$ msec, $\alpha = 8°$, $N_{\text{time}} = 10$, $N_{\text{TL}} = 16$. These parameters were similar to those used in the actual LL study. Two types of noise were added to the simulated images: intensity based Gaussian noise, and uniformly distributed white noise. Gaussian noise with standard deviation of 1%, 2.5%, 5%, or 10% of the image intensity was applied. White noise was generated with standard deviation equaled 0.5% or 1% of the mean intensity of the image at the first acquisition time point (highest intensity among all time points). An example of the simulated LL image is shown in Fig. 2.3b. The k-space data were then computed at all 160 acquisition time points. k-space segmentation was performed using both the traditional 1D centric encoding and the elliptical centric encoding methods. The segmented LL data were reconstructed and T_1 maps were calculated using the reconstructed images.

a   b
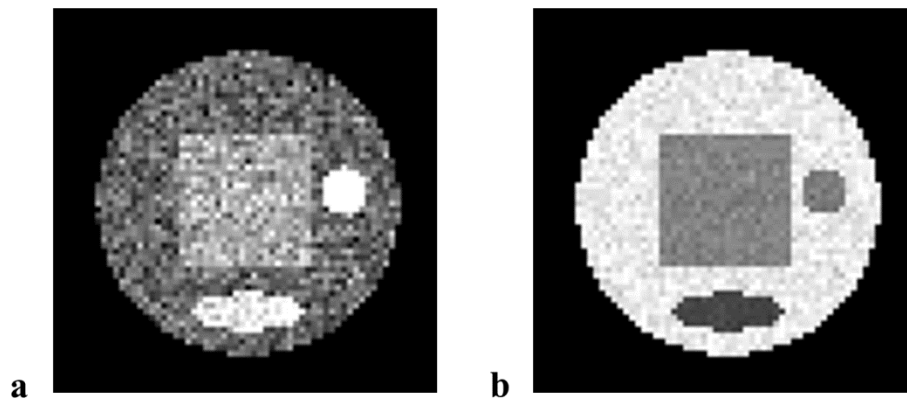
Figure 2.3 Digital phantom with four structures used for simulations. a) Representative slice of the T_1 map; b) corresponding LL image with the addition of 5% Gaussian noise and 1% white noise at the first acquisition time point. Well defined edges can be seen in the LL image.

To investigate the performance of the proposed χ^2 weighted multi-step curve fitting procedure, an artificial B_1 field was created with a smoothly varying function:

$$B_1(x,y,z) = (1.5 - 0.025(x-32)^2)$$
$$\times (1.25 - 0.012(y-21)^2) \times (0.08 + 0.02(z-32)^4) \quad (2.3)$$

The spatially varying flip angle map was then calculated by multiplying Eq. 2.3 with nominal 8° flip angle. The simulated LL data were created with the same procedure except the nominal angle was replaced by this flip angle map. 5% Gaussian noise plus 1% white noise was used to create the noisy k-space data. After image reconstruction, T_1 was estimated using the multi-step curve fitting procedure with χ^2 weighted angle maps. For comparison, T_1 was also calculated using the simple averaging angle maps.

One of the factors that is often overlooked during LL acquisition protocol is the necessity of bringing the magnetization to steady state before data acquisition. Therefore, simulation was performed using the SpinWright Bloch equation simulator [42] to determine the number of dummy scans needed to bring the magnetization to steady state. The same parameters as stated above were employed for this simulation. T_1 values of 1200 msec, 1800 msec and 3000 msec were investigated.

Finally, simulations were performed to determine the effect of T_1 on the accuracy in DCE-MRI analysis. A 2D Shepp-Logan phantom (Fig. 2.4) was employed to simulate the DCE-MRI data. It has 64×64 pixels and is separated into six regions, each with different permeability parameters. The combinations of parameters used are listed in Table 2.1. A pixel-by-pixel variation of 120 msec was applied on the T_1 values and a 2.5% variation was applied on the permeability parameters. The DCE-MRI signals were computed using Eq. 1.11. The time resolution was set to 30 sec and 82 post-contrast data were created. After the DCE-MRI images were generated, 4% Gaussian noise plus 1% white noise were applied. All simulation parameters used were similar to those in the actual DCE-MRI study of SCI. When computing the tracer concentration, instead of applying the actual T_1 value, T_1 variations from -30% to +30% were used. Analysis was performed on each T_1 variation level to investigate the propagation of error from incorrect T_1 to the pharmacokinetic parameter estimates.
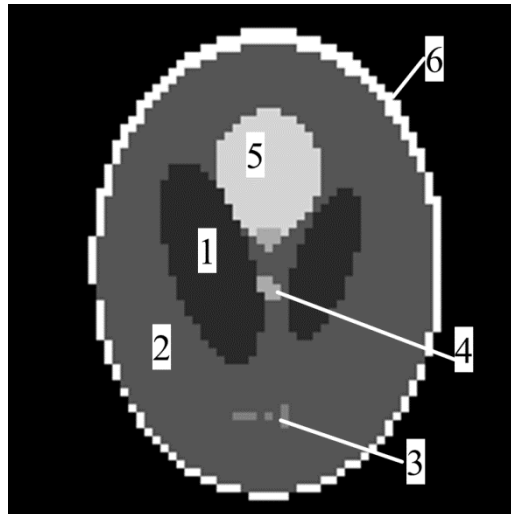
Figure 2.4 The 64×64 Shepp-Logan phantom used for simulation.

Table 2.1 The pharmacokinetic parameters applied to the Shepp-Logan phantom (Fig. 2.4).

region	f_b	K^{trans} (min^{-1})	k_{ep} (min^{-1})	T_1 (msec)
1	0.03	0.004	0.015	1200
2	0.01	0.012	0.072	1600
3	0.03	0.008	0.045	1200
4	0.03	0.003	0.012	800
5	0.08	0.004	0.033	2800
6	0.04	0.002	0.032	800

2.3.2 Phantom Study

   T1 map of a water phantom was acquired to assess the performance of the modified 3D LL sequence and the χ^2 weighted multi-step procedure. The phantom was created with 0.1 mM $NiCl_2$ doped water filling a 26 mm diameter plastic cylinder. The elliptical segmented LL acquisition was implemented on the MRI scanner. MRI scan was performed using a 71 mm diameter birdcage resonator for both RF transmission and signal reception. Different LL parameter combinations were used to examine the consistency of the LL method. In particular, the effects of different train length N_{TL} and number of time points N_{time} were investigated. The common acquisition parameters to all scans were: (TE = 2 msec, t_d = 10 msec, t_r = 1000 msec, α = 7.5°, N_{dummy} = 5, matrix size = $64 \times 64 \times 64$, field-of-view (FOV) = $40 \times 40 \times 40$ mm^3). Multi-step curve fitting procedure was employed to compute T_1 using the χ^2 weighted angle maps as well as the simple averaging angle maps for comparison. T_1 was also computed using an IRSE acquisition and it was considered to be the actual T_1 of the phantom. Only a single slice at the phantom center was acquired to reduce the total acquisition time. The acquisition parameters of the IRSE acquisition were: (TE/TR = 6.5/10,000 msec, TI = 50, 150, 300, 450, 600, 750, 900, 1050, 1250, 1500, 2000 msec, matrix size = 64×64, in-plane FOV = 40×40 mm^2, slice thickness = 2.5 mm).

   The transmitted flip angle in the LL sequence is affected by the B_1 inhomogeneity. The discrepancy between the nominal angle and the actual angle can affect the final T_1 estimation. One advantage of LL acquisition is that the actual flip angle can be estimated by the χ^2 weighted multi-step curve fitting procedure. Since the accuracy of the flip angle is important in T_1 estimation, it is necessary to acquire the actual B_1 inhomogeneity map to verify the estimated flip angle from the multi-step curve fitting procedure. For this purpose, the actual flip angle imaging (AFI) sequence was implemented [43,44] to map the B_1 inhomogeneity. The AFI acquisition involved two SPGR sequences with different TRs. Both RF spoiler and additional gradient spoiler as described in [43] were incorporated into the sequence to improve the quality of the B_1 map. The acquisition parameters employed were: (TE = 2 msec, TR = 20 msec and 100 msec, matrix size = $64 \times 32 \times 32$ interpolated to $64 \times 64 \times 64$, FOV same as in T_1 acquisition). Different flip angles were used to investigate their effect on the acquired B_1 map.

2.4 Results

2.4.1 Simulations

The performance of LL reconstruction was examined in two ways: its impacts on the image intensity at each acquisition time point and on the final T_1 estimation.

Table 2.2 summarizes the relative root mean square (RMS) errors of images at each acquisition time point with 2.5% Gaussian noise and 0.5% white noise. Table 2.3 summarizes the relative RMS error of images with 5% Gaussian noise and 1% white noise. The two noise levels represent approximately the range of noise in a normal 3D LL acquisition. The trend of RMS errors across all noise levels tested was similar. Large RMS error was observed in images 3 to 6, corresponding to acquisition time points 32, 49, 65 and 81. These images have low SNR because they were acquired around the null points of the inversion recovery curve. For the T_1 values chosen for the simulation, the null points were between acquisition time points 45 to 85. At the acquisition time point where the SNR is high, the average RMS error of the whole image using LL acquisition is comparable to that resulted from introducing noise to the images. This implies that at high SNR, the LL acquisition did not affect the overall image quality. However, the RMS error was noticeably higher using LL acquisition if the image SNR was low. In addition to low SNR, high RMS error was also observed at the edges between different intensity. Reconstruction artifact is more prominent at the edges because edges correspond to high spatial frequency. Since the high frequency components in LL acquisition are acquired at different magnetization from the center of k-space, the RMS error at the edges are higher. Fig. 2.5 shows an example of the LL signal obtained from an interface between two structures. It illustrates that the errors in image intensities can mislead the curve fitting procedure into providing a false inversion recovery curve. Comparing the elliptical segmented LL acquisition with the traditional encoding scheme, the elliptical segmentation scheme yielded smaller RMS error at the intensity interfaces.

Fig. 2.5 also shows that error in the image intensity can translate into error in the final T_1 estimation. In general, the T_1 estimation depends heavily on the data around the null point of the inversion recovery curve. Since the elliptical segmented LL acquisition yields smaller error surrounding the null point, it is expected to estimate T_1 more accurately than the traditional LL segmentation scheme. The average relative RMS error in T_1 estimation at different noise levels are plotted in Fig. 2.6. T_1 computation using the elliptical segmented data generally yielded smaller RMS error compared to using the traditional encoding data. In addition, greater improvement was observed at the edges with the elliptical segmentation scheme. The RMS error of both LL schemes however started to converge as the Gaussian noise level was increased to 10%.

The relative RMS errors of T_1 estimation in the presence of inhomogeneous B_1 were listed in Table 2.4. B_1 inhomogeneity increased the uncertainty in T_1 estimation. The elliptical segmented LL images reduced the T_1 estimation error by 2% at the edges and 1% overall compared to the traditional segmented LL images. The curve fitting procedure with χ^2 weighted filtering yielded errors that were about 0.3% lower overall and 0.6% lower at the edges compared to that using the simple averaging angle maps.

Using the SpinWright simulator, it is found that the number of required dummy scans in a LL acquisition depends on the intrinsic T_1 value of the sample. It was found that $N_{dummy} = 3$ was enough to drive the magnetization to within 0.1% difference in magnitude if the T_1 value was 1200 msec and $N_{dummy} = 5$ was needed for $T_1 = 1800$ msec. However, if the T_1 value was 3000 msec, $N_{dummy} = 7$ was needed to reach steady state. Since T_1 of in vivo brain structure is expected to be less than 1800 msec in a 7T MRI scanner, five dummy scans would suffice in the LL acquisition.

Table 2.5 summarizes the percent difference in the pharmacokinetic parameters when incorrect T_1 was applied to perform the analysis. Underestimation of T_1 (negative T_1 difference) caused increase in K^{trans} and f_b estimations. Both K^{trans} and f_b were changed by about the same factor when a particular T_1 bias was applied. k_{ep} did not appear to be affected by the incorrect T_1 at any bias level. Table 2.5 only showed results obtained from noiseless data. The average differences from data with noise (data not show) were almost identical to differences from noiseless data. The error introduced by noise would be added on to the bias introduced by the incorrect T_1.

Table 2.2 The relative RMS error of intensity at different acqtp between the original images and the images plus noise (org+n), the reconstructed images using the traditional LL sequence (trad LL), and the reconstructed images using the proposed 2D centric segmented LL sequence (cen LL). 2.5% Gaussian noise and 0.5% white noise was added to the images. Images 3 to 6 are around the null points of the inversion recovery curve and showed higher RMS error. The RMS error is generally higher at the edges compared to the whole image.

	org + n	trad LL		cen LL	
acqtp	whole	whole	edges	whole	Edges
1	2.6%	5.0%	7.7%	4.5%	6.4%
2	2.7%	5.8%	9.3%	5.1%	7.8%
3	3.4%	105.5%	35.1%	94.7%	35.3%
4	107.1%	1035.4%	1216.6%	980.7%	1086.2%
5	19.8%	65.7%	114.5%	60.0%	107.1%
6	62.8%	134.6%	206.9%	115.4%	159.3%
7	3.2%	3.9%	5.1%	3.9%	4.8%
8	2.9%	3.0%	3.5%	3.2%	3.7%
9	2.8%	2.7%	3.0%	2.9%	3.2%
10	2.7%	2.5%	2.7%	2.7%	2.9%

Table 2.3 The relative RMS error of intensity between the original images and org+n, trad LL, and cen LL. 5% Gaussian noise and 1% white noise was added to the images.

	org + n	trad LL		cen LL	
acqtp	whole	whole	edges	whole	edges
1	5.1%	5.8%	8.3%	5.6%	7.3%
2	5.4%	6.5%	9.7%	6.1%	8.4%
3	8.9%	104.9%	35.2%	92.4%	35.0%
4	214.1%	1073.7%	1239.7%	1029.4%	1112.8%
5	44.2%	88.8%	147.2%	71.5%	109.4%
6	138.0%	262.1%	369.3%	222.0%	307.7%
7	6.4%	7.0%	8.4%	7.4%	8.6%
8	5.8%	5.7%	6.3%	6.2%	6.7%
9	5.6%	5.2%	5.6%	5.7%	6.1%
10	5.5%	5.0%	5.2%	5.5%	5.7%
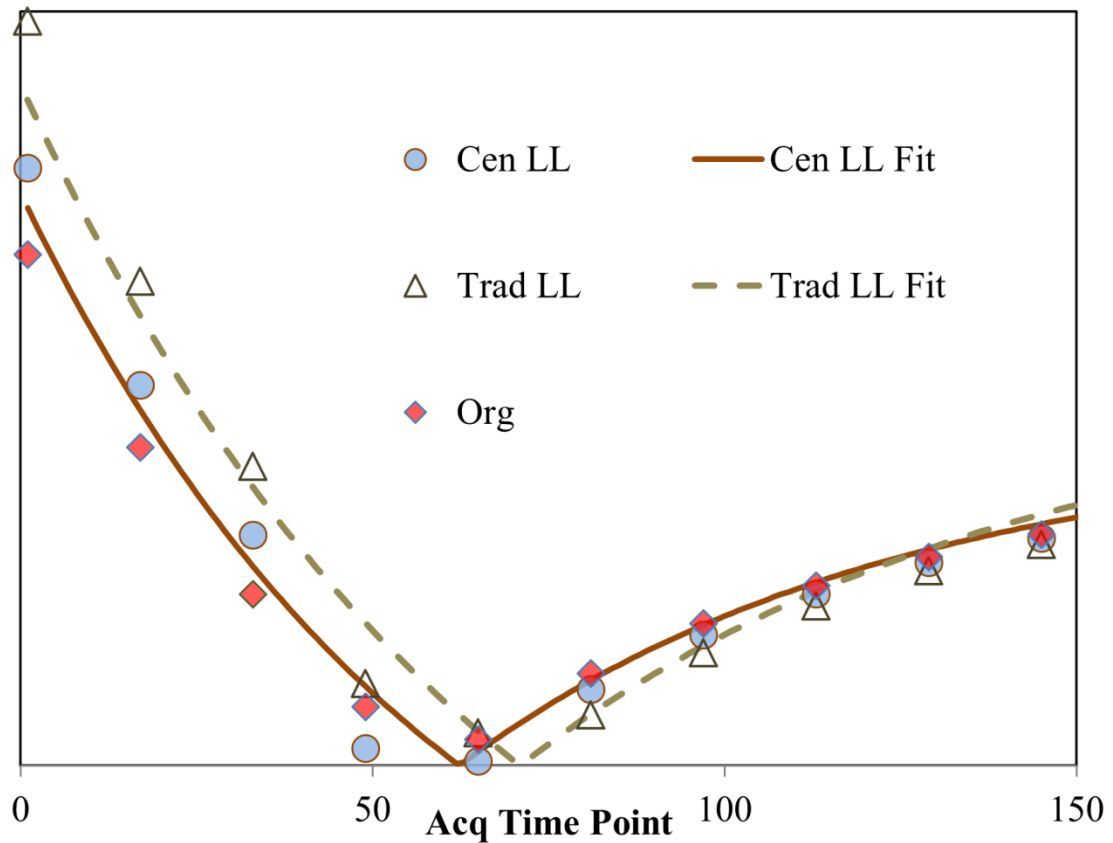
Figure 2.5 Representative simulated LL data obtained near the edge between the ellipsoid and the sphere in Fig. 2.3. The plot includes the original noiseless data (Org), the LL data using the tradition 1D segmentation (Trad LL) and using the elliptical centric segmentation (Cen LL). The inversion recovery curves fitted to the LL data showed deviations from the Org data and will cause error to the estimated T_1 value. The accuracy of T_1 estimation depends heavily on the data near the null point of the inversion recovery curve. On average, Cen LL data yielded smaller error surrounding the null point and thus yielded smaller error in the final T_1 estimation.
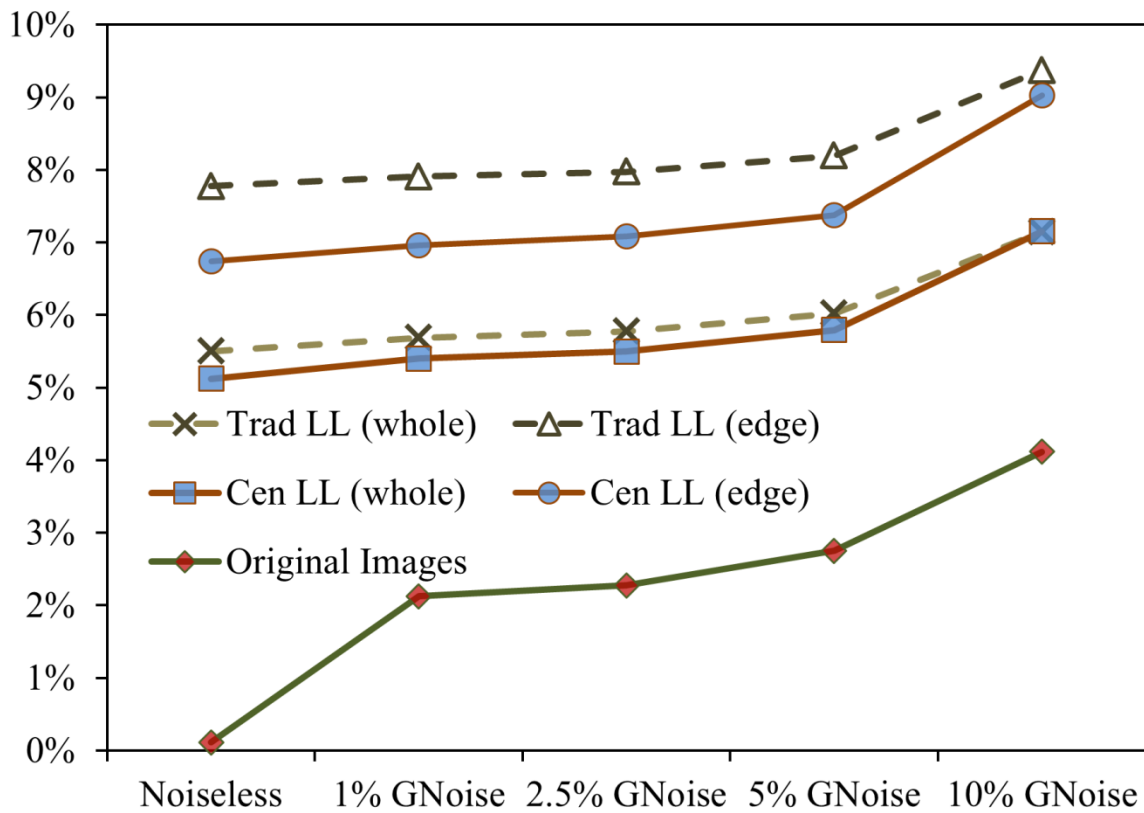
Figure 2.6 Relative RMS error (%) in T_1 estimation with 1% white noise and different levels of Gaussian noise. T_1 values were calculated from the original images, the reconstructed images using traditional 1D segmentation (Trad LL) and the elliptical centric segmentation (Cen LL). Both the average error of the entire image (whole) and the error at the edges (edge) are presented. On average, T_1 value estimated from Cen LL yielded smaller error compared to that computed from Trad LL. Addition of 0.5% white noise (data not shown) instead of 1% white noise also showed similar error pattern using different levels of Gaussian noise.

Table 2.4 The relative RMS error of the T_1 estimation from the simulated data. The reconstructed images were created with the traditional LL sequence (Trad LL) and the 2D centric segmented LL sequence (Cen LL). 5% Gaussian noise and 1% white noise was added to the images. Multi-step curve fitting procedures with simple averaging angle maps (simple avg.) and with χ^2 weighted angle maps (χ^2 wgt.) were performed to calculate the T_1 values.

	Trad LL		Cen LL	
	whole	edges	whole	edges
simple avg.	8.1%	12.1%	7.2%	10.0%
χ^2 wgt.	7.9%	11.5%	6.9%	9.4%

Table 2.5 The average relative differences between the estimated pharmacokinetic parameters and the truth (pixel-by-pixel analysis, noiseless data). Different levels of T_1 bias were applied to see its influence on the estimations.

T_1 diff.	f_b diff.	K^{trans} diff.	k_{ep} diff.
-30%	+42%	+44%	0%
-20%	+24%	+26%	0%
-10%	+11%	+11%	0%
+10%	-10%	-9%	0%
+20%	-17%	-17%	0%
+30%	-23%	-24%	0%

2.4.2 Phantom Study

Table 2.6 summarizes the average T_1 values of the Ni-doped water phantom using different LL parameters. The parameters were adjusted to ascertain that the acquisitions covered most of the inversion recovery curve. The T_1 estimated from the IRSE acquisition was equal to 781.4 ± 1.4 msec and would be considered as the "true" T_1. The T_1 estimations from the LL acquisitions agreed well with the true T_1 and were all within their respective standard deviations. Shorter train length and more time points in general can yield more precise result as suggested by the reduced standard deviation. Fig. 2.7 shows an example of the T_1 distribution with the use of the parameters listed in Table 2.6(a). Although the appearances of the T_1 map are similar using either of the methods in most cases, applying the χ^2 weighted angle maps would generally yield sharper T_1 distribution relative to the simple averaging angle map. In some cases, the variation in curve fitting may cause incorrect estimation of RF angles. The incorrect angle estimation can result in a non-Gaussian deviation as shown in Fig. 2.8. This T_1 deviation was observed using the simple averaging angle maps, but was removed when the χ^2 weighted angle maps were used. When only five time points were acquired as listed in Table 2.6(f), more noticeable T_1 error was observed. Moreover, a false 540 msec peak occurred in the histogram in Fig. 2.9a and a region of hypo intense area appeared in the T_1 image in Fig. 2.9b. Although the χ^2 weighted filtering did not remove this error completely, the amplitude of the low T_1 false peak was reduced significantly, suggested that it was more immune to the incorrect angle estimation.

Computed from the multi-step curve fitting procedure, almost all estimated inversion angles in the LL phantom study were between 179° and 180°. Unlike the inversion angle, the estimated flip angle was different from the prescribed value and varied spatially. Examples of the corresponding flip angle B_1 maps are depicted in Fig. 2.10. The B_1 acquisitions using AFI showed good reproducibility as all the computed B_1 maps were within 0.5% on average. The results in this experiment showed that the B_1 value (in percentage of the prescribed angle) was significantly different when different flip angle was applied to acquire the B_1 map, and the value of B_1 increased with decreasing applied flip angle. When 65° flip angle was applied, the average value of the B_1 map was $75 \pm 3\%$ of the prescribed 65°. The 45° and 25° AFI yielded an average B_1 of $86 \pm 3\%$ and $93 \pm 4\%$ respectively. The B_1 flip angle map computed from T_1 LL curve fitting also showed good reproducibility and appeared to show similar spatial pattern as the B_1 map acquired with AFI. The LL fitted B_1 map, which used flip angle of 7.5°, on average had B_1 value of $104 \pm 5\%$. Unfortunately, AFI method lacks the sensitivity to measure the B_1 values when the flip angle is very low or very high [44]. As a result, the 7.5° B_1 map (Fig. 2.10d, average $= 45 \pm 33\%$) failed to show meaningful inhomogeneity pattern.

Table 2.6 T_1 values estimated from Ni-doped water phantom with different LL parameters. The T_1 value was calculated using multi-step curve fitting procedure with simple averaging filtered angle maps (simple avg.) and with χ^2 weighted filtered angle maps (χ^2 wgt.) The IRSE acquisition yielded $T_1 = 781.4 \pm 1.4$ msec for the phantom.

LL parameters	simple avg.	χ^2 wgt.
(a) $N_{TL} = 16$, $\tau = 10$ ms, $N_{time} = 10$	780.0 ± 9.4 msec	780.4 ± 8.6 msec
(b) $N_{TL} = 8$, $\tau = 15$ ms, $N_{time} = 10$	779.4 ± 8.6 msec	779.8 ± 8.1 msec
(c) $N_{TL} = 4$, $\tau = 20$ ms, $N_{time} = 10$	780.0 ± 12.1 msec	776.0 ± 7.0 msec
(d) $N_{TL} = 16$, $\tau = 10$ ms, $N_{time} = 8$	778.2 ± 9.9 msec	778.6 ± 9.4 msec
(e) $N_{TL} = 16$, $\tau = 16.7$ ms, $N_{time} = 6$	782.1 ± 10.9 msec	783.2 ± 10.3 msec
(f) $N_{TL} = 16$, $\tau = 20$ ms, $N_{time} = 5$	742.8 ± 105.3 msec	768.4 ± 66.7 msec
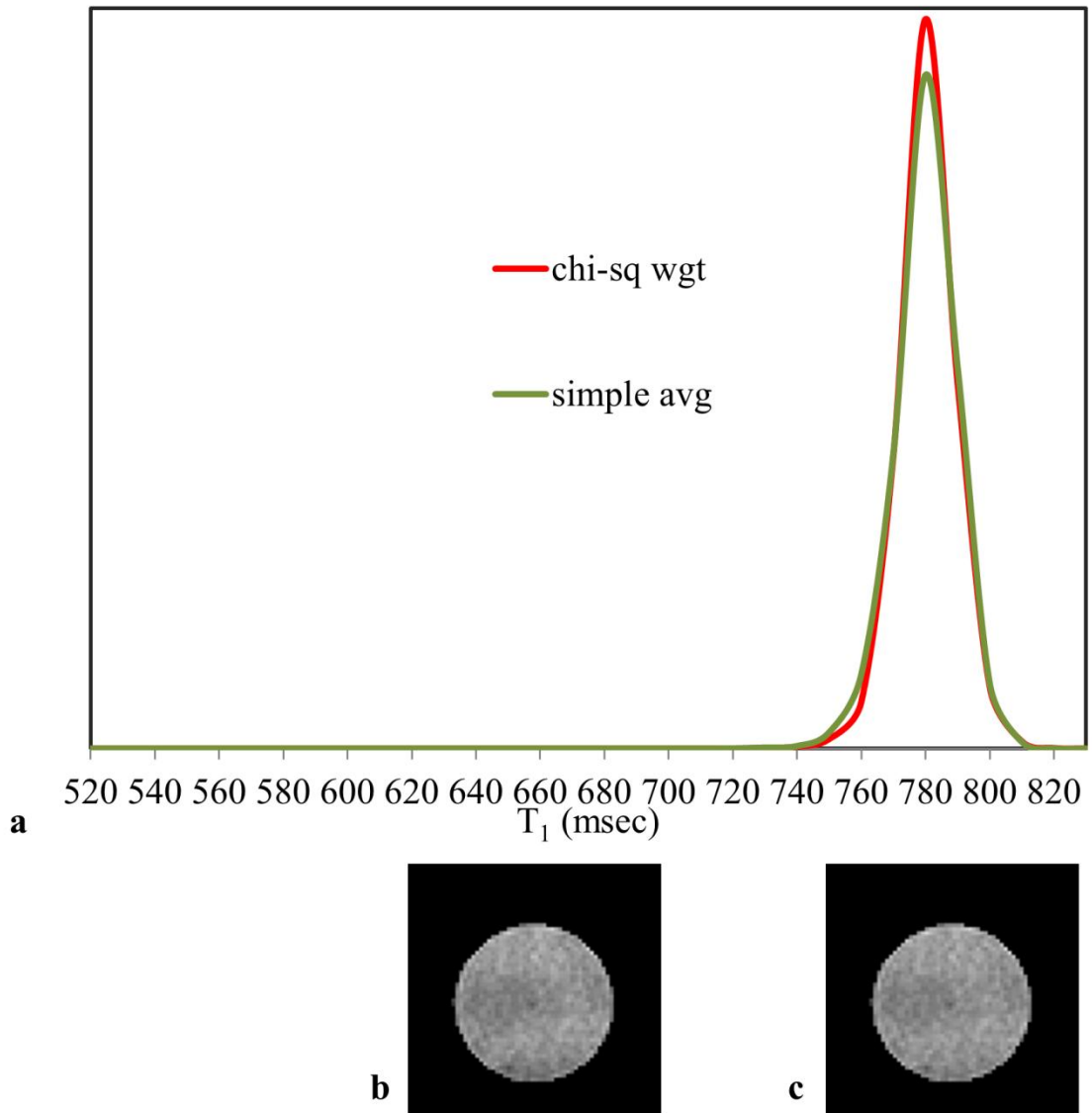
Figure 2.7 a) T_1 distribution of the Ni-doped water phantom from LL acquisition shown in Table 2.6(a) ($N_{TL} = 16$, $\tau = 10$ ms, $N_{time} = 10$). T_1 was estimated using multi-step curve fitting procedure with simple averaging angle map (simple avg) and χ^2 weighted filtered angle map (chi-sq wgt). The T_1 maps using simple avg and chi-sq wgt angle maps are shown in b and c respectively. Although the two T_1 maps appeared similar, the χ^2 weighted filtered angle map yielded sharper T_1 distribution.
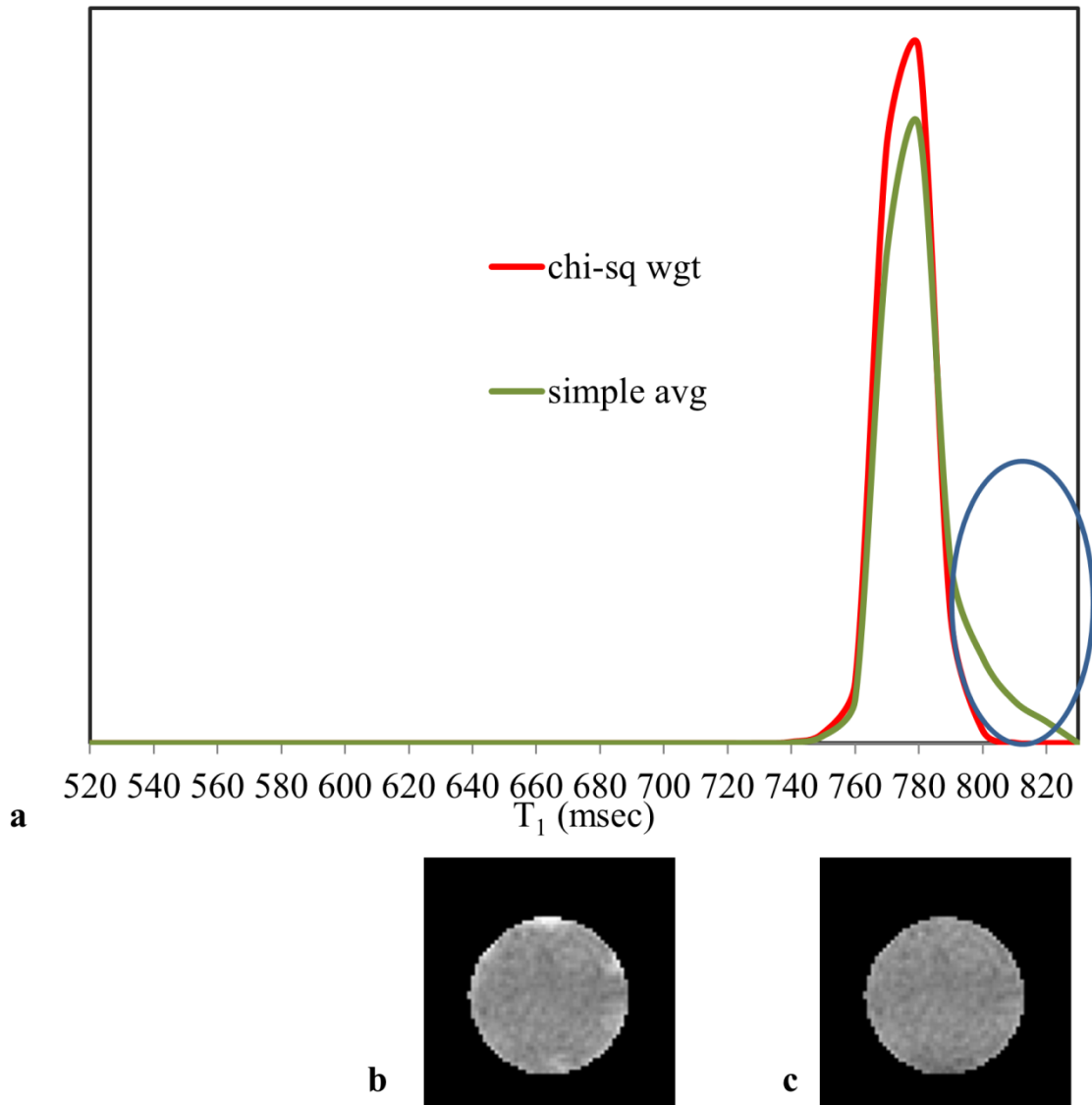
Figure 2.8 a) T_1 distribution of the Ni-doped water phantom from LL acquisition shown in Table 2.6(c) (N_{TL} = 4, τ = 20 ms, N_{time} = 10). The T_1 maps using simple avg and chi-sq wgt angle maps are shown in b and c respectively. Variation in curve fitting could result in incorrect estimation on the RF angle. Using simple avg angle map approach, the incorrect angle emerged as the non-Gaussian variation in the T_1 distribution (blue circle in a) and in the T_1 image (hyper intense region at the edges in b). Using the chi-sq wgt angle map, the non-Gaussian variation could be removed completely.
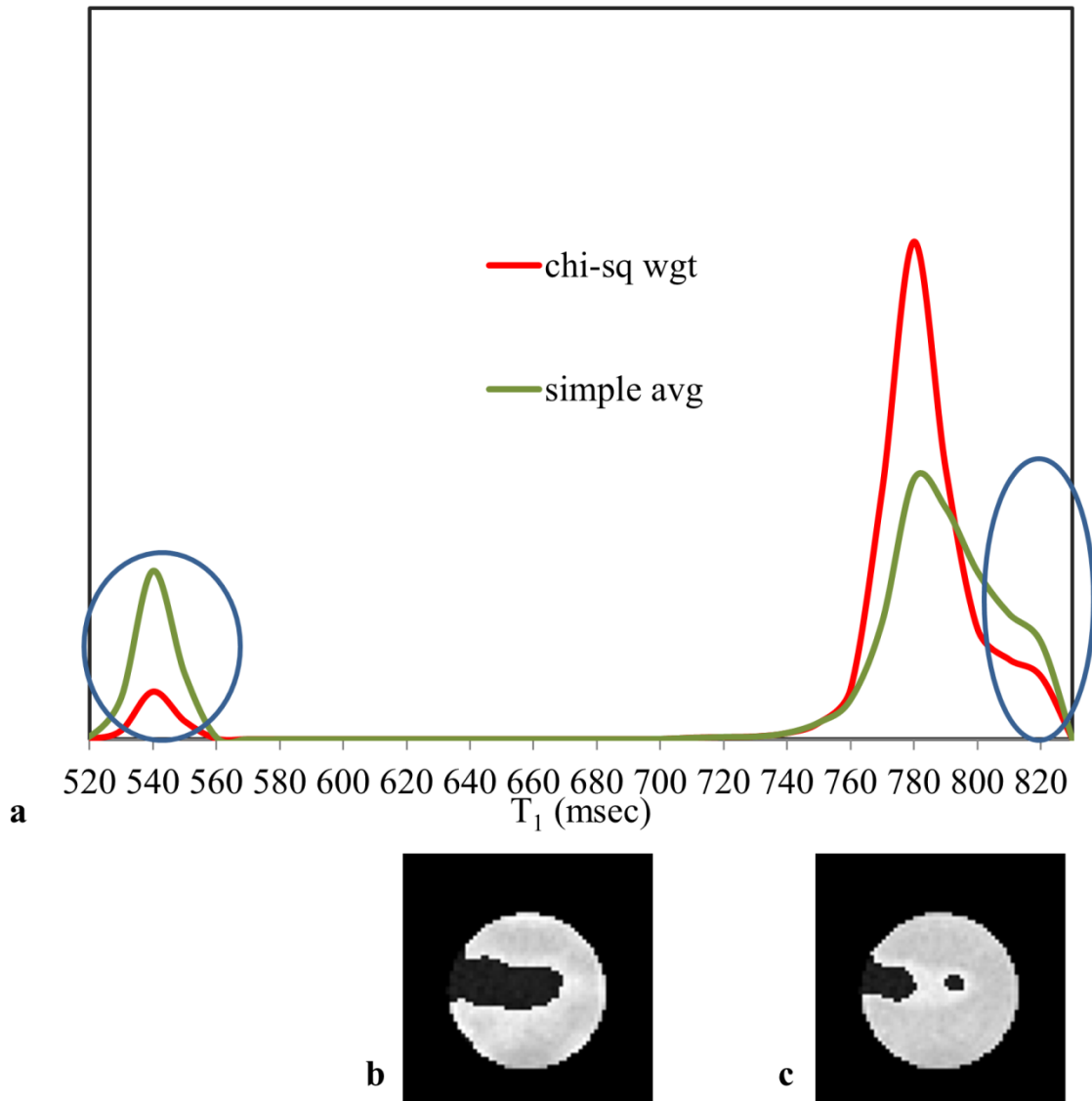
Figure 2.9 a) T$_1$ distribution of the Ni-doped water phantom from LL acquisition shown in Table 2.6(f) (N_{TL} = 16, τ = 20 ms, N_{time} = 5). The T$_1$ maps using simple avg and chi-sq wgt angle maps are shown in b and c respectively. Frequency of incorrect RF angle estimation increased with reduced number of LL acquisition time point N_{time}. In addition, the extent of the error also increased, manifested as the 540 msec peak. Although not being able to completely remove the contribution of the incorrect angles, the chi-sq wgt angle map could reduce the error.
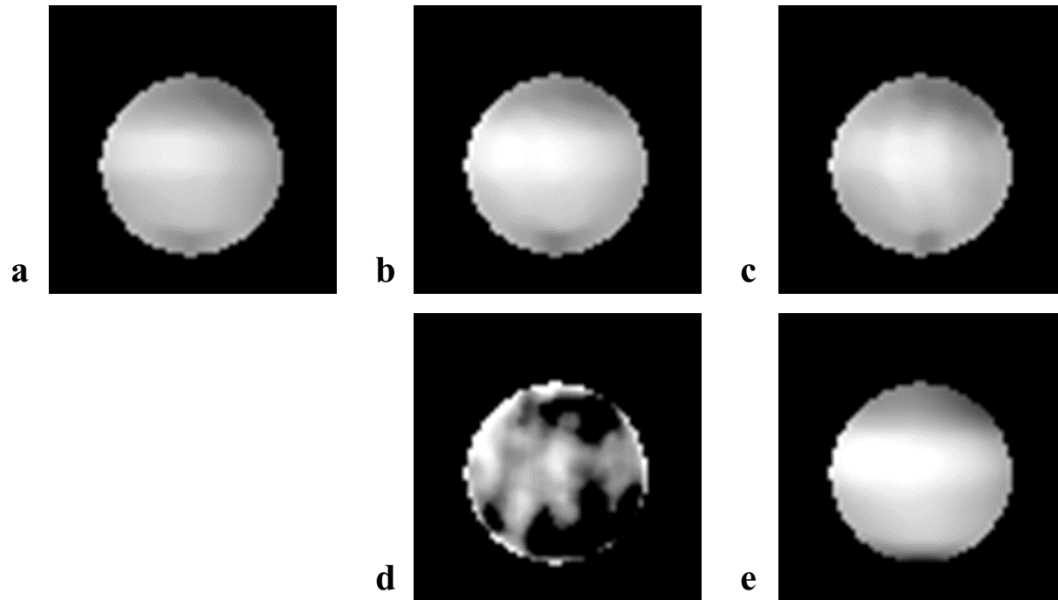
Figure 2.10 B_1 maps (not in the same window and level) of the Ni-doped water phantom using different acquisition parameters and methods. The B_1 maps acquired using AFI and flip angles of 65°, 45°, 25° and 7.5° are shown in a-d. e) B_1 map of the flip angle obtained from curve fitting of the T_1 LL data described in Table 2.6(a). a-c and e show similar spatial pattern. However, d appears to show an incorrect pattern because AFI technique is insensitive to low flip angle.

2.5 Discussion

The impact of intrinsic T_1 on the concentration-time curve is explained by Eq. 1.7. Underestimation of T_1 would lead to overestimation of tracer concentration which leads to higher K^{trans} and f_b estimates, and vice versa. Previous studies have found that error in T_1 can be detrimental to the result. Dale et al. found that K^{trans} estimates are more sensitive to T_1 error than to the intensity error in the DCE-MRI images [45]. Haacke et al. even suggested using a fixed T_1 to avoid T_1 estimation error [46]. Simulations in this work showed that the estimation error in K^{trans} was inversely proportional to the error in T_1 in a one-to-one ratio approximately. Therefore, it is important to minimize the error of T_1 estimation in order to reduce uncertainty in K^{trans}.

Inclusion of fast and accurate T_1 mapping technique such as the 3D LL acquisition is desirable in any DCE-MRI protocol. In this work, I implemented the elliptical centric encoding segmentation scheme for the LL method to improve the quality of the reconstructed images. In addition, a multi-step curve fitting procedure that utilizes χ^2 weighted filtering was implemented to improve the accuracy of T_1 computation. Computer simulations and phantom study were performed to verify the performance of these modifications.

The multi-shot 3D LL technique [36] can speed up total scan time by sampling multiple k-space lines in each shot. However, since different k-space lines for an image are acquired at different acquisition time points, the evolving magnetization will cause reconstruction artifacts along the phase encoding directions [36,47]. To reduce the reconstruction artifacts, I implemented the elliptical centric encoding segmentation scheme to acquire the LL data. This segmentation scheme ascertains that all the k-space lines closest to the center are acquired at the same magnetization state. This can reduce reconstruction artifacts because the center of k-space contains most intensity information. In addition, the effective acqtp is better correlated to the LL image under this segmentation scheme. This can further help the subsequent curve fitting procedure. The simulations show that the reconstruction artifacts are most prominent at the edges in images corresponding to time points surrounding the null point of the inversion recovery. Unfortunately, T_1 estimation is also more sensitive to the data points that are close to the null point. The elliptical segmentation scheme is shown to reduce the error around the null point. As a result, the T_1 values evaluated from the elliptical segmented LL images are more accurate compared to the traditional LL segmentation scheme. The improvement can be seen in LL images with up to 5% Gaussian noise level, which is within the expected noise level of 3D images. Therefore, applying the elliptical segmentation scheme can improve the image quality of in vivo T_1 mapping.

The actual flip angle received is always different from the prescribed angle and it varies spatially due to B_1 inhomogeneity [33]. In principle, B_1 inhomogeneity map can be acquired using different techniques [44,48-50] to correct for the actual RF angles. However, it is observed that the B_1 map depends on the applied flip angle and B_1 mapping technique is insensitive to small flip angle such

as the angle used in the LL acquisition. Therefore, it is important to accurately obtain the actual flip angle map from LL curve fitting. Similar to T_1 estimation, the accuracy of RF angle estimation is also sensitive to data fluctuation. Under the assumption that more accurate angle estimation can yield better curve fit, I developed the χ^2 weighted filtering procedure to obtain the angle maps of the LL acquisition. The filtering and smoothing are justified because the angle map is expected to be smooth and any rapid spatial variation is unlikely to be real. The simple averaging angle map as mentioned in [33] can dilute the error, but cannot remove it. Simulation has shown that using the χ^2 weighted angle maps produced more accurate results than simple averaging angle maps. In the phantom study, non-Gaussian deviation can be seen using the averaging angle map. The χ^2 weighted smoothing and filtering method was shown to provide more accurate and precise results by removing some of these incorrect angles.

There are several other factors to consider when performing the LL study. It was shown that the choice of TI can affect the result of T_1 estimation with IRSE sequence [51]. In this study, a 2% difference was seen in mean T_1 on the same phantom when using different set of TI's (data not shown). Similar discrepancy in mean T_1 was observed when different combination of τ and N_{time} were used in the LL acquisition. It is also found in the study that insufficient number of time points can increase the estimation error. In the phantom experiment, it appeared that at least six time points are needed to produce accurate result. Inadequate number of dummy scans can also affect the accuracy of the LL acquisition. Simulation showed that about five dummy scans are needed for in vivo LL T_1 study. In addition to scanning parameters, drifting field strength and temperature fluctuating can both change the intrinsic T_1 values and should be considered during T_1 mapping.

In this work, I designed an elliptical centric encoded k-space segmentation scheme to acquire LL data and it showed improvement in image quality in simulations. I programmed the acquisition sequence on the Bruker 7T MRI scanner and performed the phantom study with the implemented LL sequence. I also developed the multi-step curve fitting procedure to calculate the T_1 value from the LL data. This technique was shown to yield more accurate and precise results. The accurate T_1 map should provide more robust results in DCE-MRI.

CHAPTER 3

IMPLEMENTATION OF VIEW SHARING ACQUISITION IN DYNAMIC CONTRAST-ENHANCED MRI AND RECONSTRUCTION USING NORMALIZATION FACTOR

3.1 Introduction

It is known that the temporal resolution of the DCE-MRI image series has an influence on the estimation of pharmacokinetic parameters [19-21]. Poor temporal resolution in the post-contrast phase can introduce large uncertainty in the pharmacokinetic parameter estimates. Temporal resolution is especially important in the first few minutes following tracer administration, where the signal changes rapidly.

Multi-slice sequences [2,6,52-54] in general have scan time advantage over 3D imaging. These 2D imaging techniques however suffer from low SNR and must settle for large slice thickness. In addition, the interpretation can be affected by flow artifacts that are specific to 2D sequences. Conventional 3D sequences [5,55] have superior SNR, but its acquisition matrix size is usually small to accommodate reasonable temporal resolution. Small acquisition matrix however can lead to poor resolution and large truncation artifacts.

One solution to circumvent, to some extent, this trade-off of spatial and temporal resolution is to apply view sharing method. View sharing acquisition techniques can increase the temporal resolution in DCE-MRI without sacrificing the spatial resolution [56,57]. The acquisition time of view sharing technique is reduced by sampling only a portion of the k-space during each time point. And the spatial resolution is maintained by interpolating missing k-space from other time frames.

The keyhole imaging method was initially proposed to accelerate dynamic MRI acquisition [58,59]. In the keyhole technique, only the center of k-space is acquired during the dynamic phase. The full resolution images are then reconstructed using the outer k-space from a reference image. This acquisition scheme neglects the change in the outer k-space and can degrade the spatial resolution. Many newer view sharing techniques were implemented since then. To reduce the blurring problem, these techniques also acquire the outer k-space during the dynamic phase, but usually with lower sampling frequency. For example, Song et al. integrated the radial view-interleaved acquisition with k-space-weighted image contrast to improve the view sharing reconstruction [57]. The Unaliasing by Fourier-Encoding the Overlaps Using the Temporal Dimension [60] was proposed to accelerate 3D cardiac imaging. This method acquires data in an interleaved fashion and removes the aliasing artifacts with a k-space filtering procedure. The 3D k-t Broad-use Linear Acquisition Speed-up Technique (BLAST) [61,62] method was developed to reduce the aliasing artifact by applying a spatiotemporal filter derived from the low resolution training data.

The 3D Time-resolved imaging of contrast kinetics (TRICKS) is a method that is widely used in contrast angiography [63]. This method separates the k-space into multiple segments and the segments are sampled alternatively during the dynamic phase. Although this method has shown good results in angiography, the 3D TRICKS is designed to make qualitative examinations and is not optimized for quantitative DCE-MRI study.

In this work, a modified 3D elliptical encoded TRICKS acquisition method is implemented on the Bruker 7T MRI scanner. The acquisition order of the k-space segment is designed to better sample the DCE-MRI dynamic. In addition, a normalization factor is devised to scale the substituted k-space appropriately in order to improve the reconstruction quality of the DCE-MRI images. This method will enable the acquisition of high temporal resolution DCE-MRI images.

3.2 **Innovations**

3.2.1 View Sharing Acquisition

      The 3D TRICKS method divides the k-space into four segments that are sampled alternately to monitor the contrast dynamic [63]. Since the center of k-space contains more contrast information, central k-space is sampled more frequently than the outer k-space. Image at a particular time point is reconstructed using the current k-space segment and the missing k-space is filled from adjacent time points. Originally, the 3D TRICKS method only segments the k-space along a single phase encoding direction (k_y). Since then, elliptical segmentation is developed to improve the quality of the reconstructed images. My implementation of the view sharing acquisition was based on the 3D elliptical encoded TRICKS technique.

      Following tracer administration, the tracer circulates through the vasculature and results in increased intensity in the T_1 weighted images. Depending on the location and duration of the injection, the rapid increase in signal intensity can occur within few tens of seconds to couple of minutes after the initial administration. To simplify, this period is denoted as the tracer influx phase. The influx phase is particularly important in calculating the arterial input function (AIF). In my view sharing acquisition scheme, only the segment of center k-space is sampled during the influx phase in order to better capture the rapid signal changes. As an example, the view sharing acquisition scheme is illustrated in Fig. 3.1. The k-space is divided into four segments based on the distance from the center. Multiple fully sampled data are acquired before administering the tracer. After tracer administration, only one segment out of the four is acquired at each post-contrast time point. During the influx phase (first 1 min post-contrast), a series of segment 1 are acquired to sample the rapid intensity change. The outer segments are sampled alternatively with segment 1 thereafter, while segment 2 is sampled more frequently than segment 3 and 4.

3.2.2 k-space Normalization Factor

      The missing k-space in each post-contrast time point is filled with the k-space segments from other time points. Each missing segment is calculated from two adjacent time points, one before and one after the current time point. The substituted k-space data are usually interpolated based on the temporal distance between the time points. Assuming that the missing k-space of the current time point is more similar to the k-space of the closer time point, the k-space from the closer time point is weighted more in the calculation.
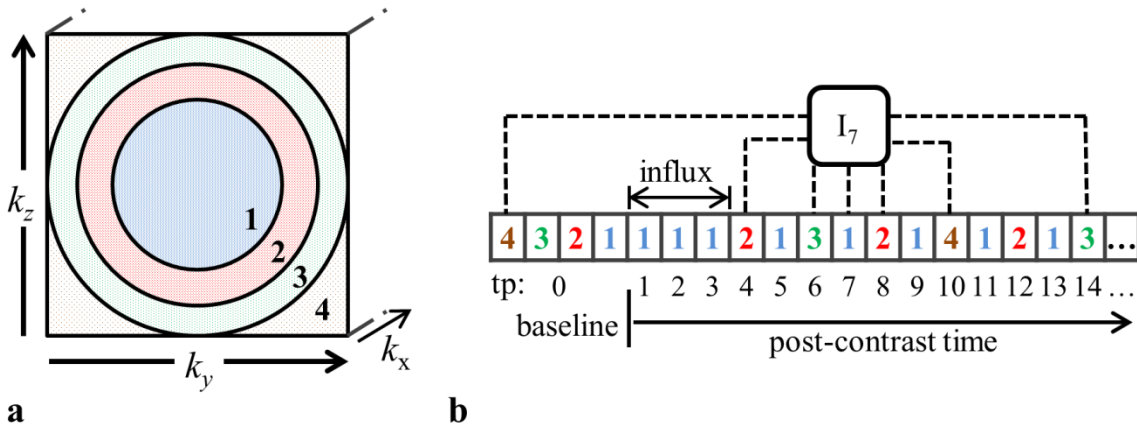
Figure 3.1 Modified 3D view sharing acquisition scheme. a) The elliptical k-space segmentation scheme. b) Acquisition order of the DCE-MRI. The number in a cell represents the segment number being acquired. The pre-contrast baseline image is fully sampled. During the influx phase, only segment 1 is acquired repeatedly, which allows more sampling of the fast changing signal. Each post-contrast image is reconstructed using the segment from its corresponding time point plus interpolation of other segments from neighboring time points. For example, image 7 requires segment 2 from time point 4 and 8, segment 3 from time point 6 and 14, and segment 4 from time point 0 and 10.

However, the signal is different at different time points due to the contrast agent. The k-space interpolation alone does not account for this change in signal, which may cause artifacts in the reconstructed images. In this work, I propose to normalize the substituted k-space data to account for the change in intensity. We consider the difference in signal between two time points i and j as:

$$S_j - S_i = f_N(i \rightarrow j) \cdot S_i$$

The proposed k-space normalization approach assumes that the signal difference of the entire image is approximately governed by a multiplication factor f_N. Under this assumption, the whole k-space would be altered by the same factor f_N. Since the central k-space is least affected by noise, the normalization factor would scale the center of k-space from the substituted time frames to the same magnitude as the center of k-space at the current time frame. The same scaling factor is applied to the entire substituted k-space data.

For notational purpose, the two substituted k-space segments R, that are needed to reconstruct image I_j at time point j, would be taken from time points j_R^+ and j_R^-. j_R^+ represents the forward time point where segment R is sampled that is closest to time point j and j_R^- represents the backward time point. The substituted data are then interpolated and normalized using the following equation:

$$k_R(j) = \frac{j - j_R^-}{j_R^+ - j_R^-} \cdot f_N(j_R^+) \cdot k_R(j_R^+) + \frac{j_R^+ - j}{j_R^+ - j_R^-} \cdot f_N(j_R^-) \cdot k_R(j_R^-)$$ (3.1)

where the first factor is the interpolation factor and the second factor:

$$f_N(j_R^\pm) = \frac{\sum_{cen}|k_R(j)|}{\sum_{cen}|k_R(j_R^\pm)|}$$ (3.2)

is the normalization factor. $\sum_{cen}|k_R(j)|$ represents the sum of the magnitude of the $3 \times 3 \times 3$ data encompassing the center of k-space. However, outer k-space segments lack the central k-space. Therefore, their center of k-space is approximated from the neighboring segment 1:

$$\sum_{cen}|k_R(i)| = \begin{cases} \sum_{cen}|k_1(i-1) + k_1(i+1)| & \text{if } R \neq 1 \\ \sum_{cen}|k_1(i)| & \text{if } R = 1 \end{cases}$$ (3.3)

The normalization factor is proposed to adjust the overall intensity in all the substituted segments to the intensity at the current time point in order to reduce reconstruction artifacts.

3.3 Methods and Materials

A phantom study was designed to assess the performance of the proposed normalization factor in DCE-MRI view sharing acquisition. The 3D digital phantom described in section 2.3.1 was used in this simulation study. The intensity change of the phantom was designed to simulate the signal change in the actual DCE-MRI study of SCI. Each object was assigned with a set of parameters: sphere ($f_b = 0.08$, $K^{trans} = 0.012 \text{min}^{-1}$, $k_{ep} = 0.02 \text{min}^{-1}$, $T_1 = 1200 \text{msec}$), cube ($f_b = 0.01$, $K^{trans} = 0.002 \text{min}^{-1}$, $k_{ep} = 0.005 \text{min}^{-1}$, $T_1 = 1000 \text{msec}$), cylinder ($f_b = 0.02$, $K^{trans} = 0.002 \text{min}^{-1}$, $k_{ep} = 0.045 \text{min}^{-1}$, $T_1 = 800 \text{msec}$) and ellipsoid ($f_b = 0.06$, $K^{trans} = 0.004 \text{min}^{-1}$, $k_{ep} = 0.018 \text{min}^{-1}$, $T_1 = 3200 \text{msec}$). The parameters were then randomized with a Gaussian distribution with a standard deviation of 2.5% for the pharmacokinetic parameters and 100 msec for T_1. Each of the four structures also has a different magnitude to create the effect of edges between them. A bi-exponential function was used to model the AIF [64]:

$$C_b(t) = 0.3e^{-0.22t} + 0.5e^{-0.02t} \tag{3.4}$$

These parameters of the AIF were obtained from the SCI experiment. Detail of the AIF extraction is described in section 5.3.1. DCE-MRI images were generated using Eq. 1.11. To simulate the sampling rate similar to that in the SCI experiment, a temporal resolution of 30 sec was chosen and 42 post-contrast images were simulated. The influx phase was set to 1 min; therefore segment 1 was acquired during the first two post-contrast time points. Different levels of Gaussian noise and white noise were applied to the images to investigate the effect of noise to the view sharing acquired data. Comparison was made between the traditional 3D TRICKS with single phase encoded segmentation, the 3D TICKS acquisition with elliptical segmentation, and the proposed elliptical segmented method with k-space normalization.

3.4 Results

The simulated DCE-MRI reconstructed images were compared to the noiseless original images. The relative RMS error was used as the metric to evaluate the performance of different view sharing acquisitions and reconstruction methods. The relative RMS error of the reconstructed images with 2.5% Gaussian noise and 0.5% white noise, which was approximately the lower noise limit in the 3D MRI images, are shown in Table 3.1. The RMS error of images with 5% Gaussian noise and 1% white noise, which was expected to be the upper noise limit of the 3D MRI images, are shown in Table 3.2. In general, the RMS error was highest at the first post-contrast time point for all acquisition methods. The RMS error then decreased as more segments were acquired and reached a plateau thereafter. On average, the view sharing acquisition scheme can reduce speckle noise because of temporal averaging using k-space data from two different time points. When the noise level was high (see Table 3.2), the noise reduction of temporal averaging masked the errors due to artifacts. All view sharing acquisition schemes produced images with RMS error less than the original-plus-noise images throughout all time points. However, at lower noise level (see Table 3.1), the RMS error from reconstruction artifacts were apparent at the early post-contrast phase especially near the edges. Because different k-space segments were collected at different signals, the reconstruction artifact was expected to be more severe at the edges. The larger RMS errors near the edges were observed mostly in the first few post-contrast time points and were not observed at later time points.

Comparing the three different methods, the proposed elliptical segmented scheme using a normalization factor yielded the smallest RMS error in the first few post-contrast time points. It helped reduce reconstruction artifacts, especially error at the edges. Using the proposed normalization factor, the average RMS error was reduced by up to 0.6% at the lower noise level (2.5% Gaussian noise + 0.5% white noise) and 0.4% at the higher noise level (5% Gaussian noise + 1% white noise). Neither the segmentation scheme nor the reconstruction method seemed to affect the image quality after the early post-contrast phase.

Table 3.1 The relative RMS error in intensity between the reference original images and the images with noise (org + n), the reconstructed images using traditional TRICKS (TRICKS), elliptical segmented TRICKS (ES-TRICKS), and the elliptical segmented TRICKS with normalization factor (Norm-ES). 2.5% Gaussian noise plus 0.5% white noise are applied to the image at each time point. The first four acquisition phases showed more variation in terms of RMS error compared to the rest of the reconstructed images. The error in the rest of the phases reached a plateau and thus only the averages of phases 5 to 42 are shown (rest).

	org+n	TRICKS		ES-TRICKS		Norm-ES	
phase	whole	whole	edges	whole	edges	whole	edges
1	2.5%	2.7%	4.2%	2.4%	3.5%	2.2%	2.9%
2	2.5%	2.2%	3.2%	2.1%	2.8%	2.0%	2.3%
3	2.5%	2.0%	2.4%	2.0%	2.2%	1.9%	1.9%
4	2.5%	1.9%	2.3%	2.0%	2.1%	2.0%	2.0%
rest	2.5% ±0.1%	2.0% ±0.1%	1.9% ±0.1%	2.0% ±0.1%	1.9% ±0.1%	2.0% ±0.1%	1.9% ±0.1%

Table 3.2 The relative RMS error in intensity in images with 5% Gaussian noise plus 1% white noise added to the image at each time point. The first two times points showed higher error than the rest. The error oscillated around the same level thereafter.

	org+n	TRICKS		ES-TRICKS		Norm-ES	
phase	whole	whole	edges	whole	edges	whole	edges
1	5.1%	3.7%	4.8%	3.5%	4.3%	3.5%	3.9%
2	5.1%	3.7%	4.1%	3.6%	3.9%	3.5%	3.6%
Rest	5.1% ±0.1%	4.0% ±0.2%	3.8% ±0.1%	4.0% ±0.2%	3.9% ±0.1%	4.0% ±0.2%	3.9% ±0.2%

3.5 Discussion

To obtain the dynamics of tracer concentration, a series of post-contrast T_1-weighted images must be acquired rapidly. In order to accelerate the acquisition speed without losing spatial resolution, a view sharing acquisition scheme based on the elliptical segmented 3D TRICKS method was implemented. The acquisition order was re-designed so that only the center of k-space was acquired during the influx phase to better sample the rapid signal change and the outer segments were sampled alternatively with the center thereafter. In addition, a k-space normalization method to correct for intensity changes in the view sharing data was also developed.

Temporal resolution of the DCE-MRI data has great impact on the accuracy of the results. View sharing techniques in DCE-MRI can increase the temporal resolution while maintaining the spatial resolution. In addition to increased temporal resolution, view sharing acquisition can also reduce speckle noise in the MR images because of the nature of temporal averaging. This can be very beneficial in DCE-MRI analysis because of its high sensitivity to noise. One of the disadvantages of view sharing method is the potential reconstruction artifacts. Because the different sections of the k-space data are acquired at different post-contrast phases, the reconstruction artifacts will be prominent at the edges between different structures. In this work, the k-space normalization method in view sharing acquisition was introduced to reduce the artifacts that can improve the DCE-MRI accuracy.

From the simulation results of this study, the artifacts were more severe in the first few post-contrast phases where rapid change in signal intensity occurred. The proposed k-space normalization method introduces a scaling factor to bring the intensity of the substituted k-space segments to the intensity level at the current time frame. Applying the proposed normalization factor was shown to reduce the overall error of the reconstructed images. This improvement was especially noticeable at the edges during the early post-contrast time points.

To summarize, I implemented the view sharing acquisition method on the Bruker 7T MRI scanner. The view sharing acquisition allows rapid data acquisition and can reduce random noise in the DCE-MRI images. Reconstruction with a k-space normalization factor was proposed and its application showed improvement in image quality during the fast changing early post-contrast phase.

CHAPTER 4

LOCAL SEARCH CLUSTERING ALGORITHM FOR DYNAMIC CONTRAST-ENHANCED MRI ANALYSIS ON CENTRAL NERVOUS SYSTEM

4.1 Introduction

Fast image acquisition in DCE-MRI requires very short TR. Reduced TR sacrifices the SNR in the image and results in poor contrast-to-noise ratio (CNR). The poor CNR in DCE-MRI makes it difficult to obtain consistent results. Traditionally, ROI is drawn and the average permeability within the ROI is computed. However, the results can vary considerably from one observer to the other [65].

To reduce the variability in the DCE-MRI results, some authors have relied on pattern recognition methods to classify DCE-MRI data. Measurements such as rate of early enhancement, area under the curve and time to peak are all used in DCE-MRI analysis. Lavini et al. proposed a pattern recognition method that utilized five classifiers to place the voxels into seven categories [12]. However, these techniques are qualitative analyses and are not sensitive to small permeability changes. The curve pattern analysis (CPA) was proposed by Guo et al. as an alternative to the compartment model [66]. In this method, four CPA parameters are computed based on the pattern of the concentration-time curve instead of the pharmacokinetic parameters. Unfortunately, the proposed parameters have poor correlations to the K^{trans} value.

Another way to reduce parameter variability is to increase the effective CNR by data clustering. Several authors have developed automatic clustering algorithms to extract specific features from the tracer concentration-time curve. Chen et al. proposed the fuzzy c-means clustering based technique to DCE-MRI of breast lesions [67]. Stoutjesdijk et al. applied the mean shift multi-dimensional clustering technique to assign spatially contiguous voxels to clusters [68]. Similarly, Castellani et al. applied the mean shift clustering approach to cluster data based on four features in the concentration-time curve [69]. The self-organized map was implemented by Nattkemper et al. to distinguish between malignant and benign tumors based on multiple features of the concentration-time curve [70]. These techniques operate on the feature space of the concentration-time curve where the whole curve is reduced to few parameters.

In the DCE-MRI of CNS, however, the BBB and the BSCB can limit the tracer from entering the parenchymal tissue. This leads to very low increase in signal intensity in the post-contrast images and further aggravates the already low CNR. The insufficient CNR makes it difficult to effectively extract the necessary features from individual concentration-time curve and thus the aforementioned clustering techniques may not be suitable.

To circumvent the low sensitivity of CNS imaging, a local search clustering algorithm that groups proximal voxels with similar tracer uptake curves and T_1 values was developed. The proposed clustering algorithm is aimed to produce reliable segmentations without sacrificing heterogeneity in vascular permeability. The apparent CNR in the clustered segments increases and therefore improves the consistency of pharmacokinetic parameter estimation.

4.2 Innovations

Local Search Clustering Algorithm

The proposed local search clustering algorithm takes into account the whole concentration-time curve instead of selective features. This can reduce the bias associated with certain time points when only specific features are used. The algorithm also considers the T_1 value of the voxel as a classifier so that the cluster would contain only one tissue type. A seed growing procedure is employed to recruit local voxels into a cluster.

The algorithm begins with a t-test that identifies all voxels with higher intensity in the post-contrast phase compared to the baseline. All positive voxels are potential seed points. First, the algorithm starts with a center seed point. It then searches for new members of a cluster by expanding from the seed, one voxel outward in each cycle. After each cycle, all members of the current cluster form a "seed collection" and the seed point of the cluster is replaced by this seed collection. The expansions and replacements continue until stopping condition is reached. To be included in the cluster, the cost function of voxel i within the search region must satisfy the cost threshold:

$$f_i = \frac{\sqrt{\sum_t \left(E_i(t) - E_{\text{seed}}(t)\right)^2 / N_t}}{\Delta E_{i+\text{seed}}}$$

$$+ \frac{1}{4} \frac{\sqrt{\sum_t^{t_1} \left(E_i(t) - E_{\text{seed}}(t)\right)^2 / N_{t_1}}}{\Delta E_{i+\text{seed}}} + \frac{\left|T_{1,i} - T_{1,\text{seed}}\right|}{\Delta T_1} + \frac{\text{Dis}(i - \text{seed})}{\Delta \text{Dis}} < f_{\text{thre}} \tag{4.1}$$

Three classifying terms are used to compute the cost function: the post-contrast relative intensity change, the T_1 and the distance classifiers. The first two terms are the intensity classifiers which ascertain that the relative intensity change-time courses are similar in all voxels within the same cluster. $E_i(t)$ is the relative intensity change of voxel i at post-contrast time point t computed from:

$$E_i(t) = \frac{I_i(t) - I_i(0)}{I_i(0)} \tag{4.2}$$

ΔE_i is the standard deviation of the change in relative intensity averaged through each time point assuming 5% error in the signal:

$$\Delta E_i = \sqrt{2} \times 0.05 \times (1 + \bar{E}_i) \tag{4.3}$$

The relative intensity standard deviation of a seed collection ΔE_{seed} is computed through ordinary multi-sample standard deviation instead of the assumed 5%. To control the possible inflation of ΔE_{seed} as voxels in the seed collection accumulate, ΔE_{seed} is capped at 7.5% of the signal error. The combined relative intensity standard deviation is:

$$\Delta E_{i+\text{seed}} = \frac{\Delta E_i + N_{\text{seed}} \cdot \Delta E_{\text{seed}}}{1 + N_{\text{seed}}} \tag{4.4}$$

where N_{seed} is the number of voxel in the seed collection. N_t and N_{t_1} are number of time points in their respective summation. The first intensity classifier term is summed through all time points (N_t) while the second term is only summed to t_1 after tracer administration (N_{t_1}), which is defined to be 8 min. There are two reasons that the first 8 min post-contrast phase is weighed more, because: 1) this is the more important phase in terms of pharmacokinetic parameter computation; 2) most clinical DCE-MRI protocol is completed within 10 min; therefore, the early post-contrast phase is more clinically relevant. The third term in Eq. 4.1 is the T_1 classifier. The T_1 classifier ensures that all clustered voxels have similar T_1. As mentioned in chapter 2 (see Table 2.5), the T_1 value has an impact on the accuracy of DCE-MRI analysis. Similar T_1 in a cluster is therefore necessary to maintain the accuracy of the results. The final term in Eq. 4.1 is the distance classifier, where $\text{Dis}(i\text{-seed})$ is the minimum distance between voxel i and the seed point or the surface of the seed collection. The distance classifier was used to ensure that clustered voxels are localized since there may not be physiological relevance to have a cluster with distant isolated parts. ΔT_1 and ΔDis are user defined weighting factors, whereas f_{thre} is the threshold of the cost function. Adjusting ΔT_1, ΔDis and f_{thre} can change the relative weighting of each classifier in the cost function and the performance of the clustering. Although the starting center seed point must pass the t-test for positive change in intensity, any voxel with properties that satisfy Eq. 4.1 can be a member of a cluster.

All voxels within the search region that satisfy the cost limit will form the new seed collection for the current segment. E_{seed}, ΔE_{seed} and $T_{1,\text{seed}}$ will be recalculated based on these new voxels. It is possible that some voxels that were members of the seed collection from previous search cycle no longer satisfy the cost limit in the current cycle after the seed collection updates. In this scenario, the memberships of those voxels would be withdrawn. After a stopping condition is met, the algorithm will search for the voxel within the current cluster that yields the smallest cost function f_i in Eq. 4.1. This voxel will be the refreshed center seed point for the current segment. If the refreshed center point is different from the previous center points, the operation will start from scratch with this refreshed center point and all current seed collection in the current cluster will be discarded. On the other hand, if the refreshed center point is the same as one of the previous center points, this cluster will be finalized and the procedure will continue with another new cluster starting from another new center seed point.

Several stopping conditions are employed to break the loop of cluster recruitment, if: 1) the total number of seed collection is less than a pre-defined value after a search cycle; 2) the surface of the seed collection does not grow outward after a search cycle; 3) the refreshed center seed point cycles back to one of the previous center seed point (if not stopped, the algorithm will run into an infinite loop);

4) the number of voxels in the seed collection exceeds some pre-defined number to retain heterogeneity of the data.

The final step of the clustering algorithm is to find a pre-existing cluster for all the remaining unclustered voxels that passed the t-test. A left-out voxel i can join an immediate neighboring cluster if the cost function satisfies Eq. 4.1 with no contribution from the distance classifier (the distance classifier is null because the voxel and the cluster here must be neighbors) and usually a slight relaxation on the threshold f_{thre}. When multiple clusters satisfy the limit, the voxel will join the cluster that yields the lowest cost function.

A flow chart of the segment formation procedure with the proposed cluster algorithm is depicted in Fig. 4.1.
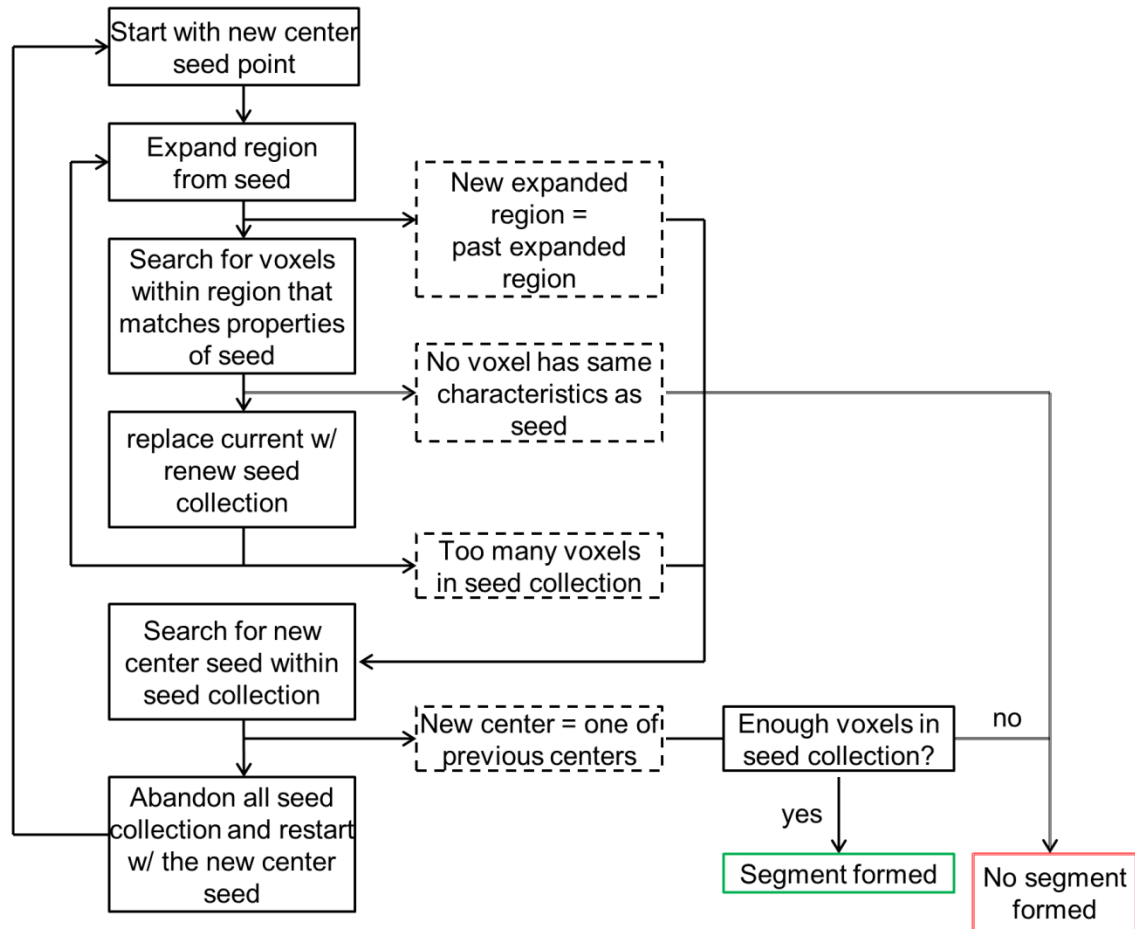
Figure 4.1 Schematic representation of the process of cluster formation using the local search clustering algorithm. The dashed boxes are the four stopping conditions that can break the loop of cluster recruitment.

4.3 Methods and Materials

The effectiveness of the clustering algorithm and its impact on the DCE-MRI analysis was investigated by simulations. The simulations were prepared to imitate the DCE-MRI experiment of SCI so all the applied parameters were similar to those found in the actual experiment. The 2D Shepp-Logan phantom shown in Fig. 2.4 was employed for simulations. In order to investigate the effect of contrast uptake on the estimation accuracy, different K^{trans} and k_{ep} were applied to different structures but the same f_{b} was used. The applied pharmacokinetic parameters are listed in Table 4.1. A pixel-by-pixel variation of 120 msec was applied to the T_1 values and a 2.5% variation was applied to the permeability parameters. A bi-exponential function described in Eq. 3.4 was used to model the AIF. The time resolution was set to be 30 sec and 82 post-contrast data were created. After the DCE-MRI images were generated, 4% Gaussian noise plus 1% white noise were applied. The level of noise was chosen assuming data were acquire with the view sharing acquisition and the inherent noise level was 5% Gaussian distributed.

The following parameters were used to perform the clustering algorithm: $\Delta T_1 = 250$ msec, $\Delta \mathrm{Dis} = 2$ pixel, $f_{\mathrm{thre}} = 3$. The minimum number of pixels to form a cluster was set to 3 to ensure adequate CNR. The threshold used to group the left-out pixel was also set to 3. After the data were clustered, the average intensity change and average T_1 were computed in each cluster. DCE-MRI analysis was performed on the average data of the clustered ROIs. For comparison, the results were compared against the results obtained from the pixel-by-pixel analysis.

Table 4.1 The pharmacokinetic parameters applied to the Shepp-Logan phantom (Fig. 2.4) in the simulations. f_b is proton fraction of blood, K^{trans} is the transfer constant, and k_{ep} is the rate constant in the region.

region	f_b	K^{trans} (min^{-1})	k_{ep} (min^{-1})	T_1 (msec)
1	0.03	0.006	0.025	800
2	0.03	0.008	0.016	1200
3	0.03	0.003	0.045	1600
4	0.03	0.004	0.043	800
5	0.03	0.002	0.042	1400
6	0.03	0.012	0.030	2200

4.4 Results

Fig. 4.2 illustrates a representative relative intensity-time curve from the simulation that shows a typical example of noise affecting the final curve fitting result. Although the curve fit yielded a χ^2 value that had less than 0.01% chance of being incorrect, the final results of the pharmacokinetic parameters were deviated by 37% for f_b, 15% for K^{trans} and 49% for k_{ep}.

Fig. 4.3 shows the K^{trans} map of the simulated data. The results from pixel-by-pixel analysis (Fig. 4.3b) appeared noisy and the boundaries between region 1 and region 2 were smeared. The pink pixels in Fig. 4.3b represented pixels where the curve fit errors were above 95% in the χ^2 distribution. Even with these pixels removed, the result still showed high variability. Fig. 4.3c showed the results using the clustered ROIs. This result appears closer to the truth and it preserves the contrast between boundaries. The pink pixels in Fig. 4.3c represent unclustered pixels. The unclustered pixels were mostly from regions with small number of similar pixels.

The relative RMS errors of the pharmacokinetic parameter estimation are summarized in Table 4.2. On average, the estimation of f_b was found to be the most error prone, whereas K^{trans} estimate on average had the smallest RMS error among the three. In general, the RMS error increased with decreased permeability, or K^{trans}. In high permeability region (region 6), the RMS error in K^{trans} and k_{ep} was relatively small; while the RMS error was high in low permeability region (region 5). The low permeability in region 5 led to low CNR, and consequently led to poor curve fitting to the data. The RMS error could be reduced by removing curve fits that yielded high χ^2 values (95% cutoff). However, the improvement was less than 1% in K^{trans} and about 2% in k_{ep}. With the exception of k_{ep} in region 3, analysis on the clustered data produced smaller RMS errors in all parameters compared to analysis on individual pixel. The error for clustered data was high in region 3 because only three of the seven pixels were clustered, the small cluster led to low CNR and thus increased the estimation uncertainty. On average, the local search clustering algorithm reduced the RMS error by more than half compared to the pixel-by-pixel analysis.
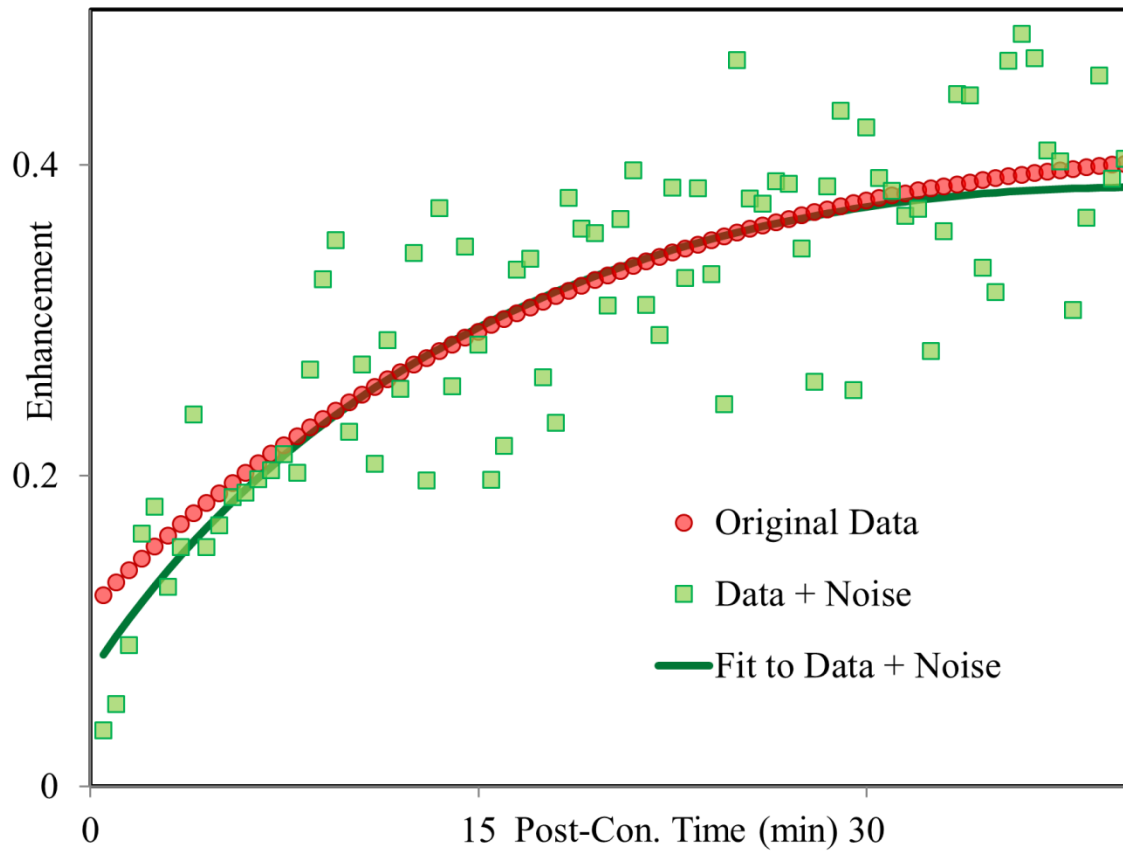
Figure 4.2 Example of a DCE-MRI relative intensity change vs. time curve. The addition of noise to the data can affect the performance of curve fitting, leading the fitted curve to deviate from the original data.
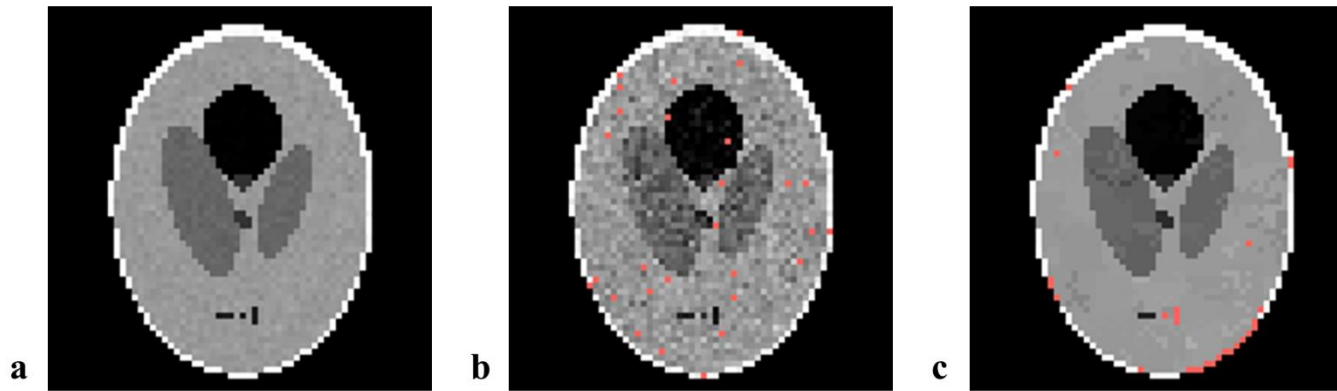
Figure 4.3 The K^{trans} maps of the simulation. a) The original K^{trans} map. b) The K^{trans} map calculated with pixel-by-pixel analysis. c) The K^{trans} map obtained from analysis of the clustered data. The pink pixels are pixels with high fitting errors (in b) or unclustered pixels (in c) and are considered unknown.

Table 4.2 Relative RMS error of the pharmacokinetic estimates using pixel-by-pixel analysis (px×px), with high χ^2 cutoff (p×p cutoff) and using the clustered data (cluster). The curve fitting procedure was reliable as the estimates using noiseless data yielded error of less than 0.5%.

		px×px	p×p cutoff	cluster
region 1 (322 px)	f_b	45.1%	45.1%	14.3%
	K^{trans}	13.8%	13.8%	4.5%
	k_{ep}	26.3%	26.3%	6.3%
	remark		**no pixel cut**	
region 2 (1346 px)	f_b	30.6%	29.9%	8.6%
	K^{trans}	8.6%	8.1%	3.4%
	k_{ep}	25.8%	22.8%	5.9%
	remark		**22 pixel cut**	**3 px unclustered**
region 3 (7 px)	f_b	14.3%	14.3%	11.1%
	K^{trans}	14.0%	14.0%	7.7%
	k_{ep}	16.3%	16.3%	17.1%
	remark		**no pixel cut**	**4 px unclustered**
region 4 (14 px)	f_b	38.1%	38.1%	24.0%
	K^{trans}	23.2%	23.2%	5.8%
	k_{ep}	29.2%	29.2%	7.3%
	remark		**no pixel cut**	
region 5 (158 px)	f_b	25.0%	24.6%	5.2%
	K^{trans}	27.0%	27.1%	9.9%
	k_{ep}	38.6%	38.9%	8.6%
	remark		**2 pixel cut**	
region 6 (178 px)	f_b	26.5%	18.9%	8.4%
	K^{trans}	8.1%	4.7%	2.9%
	k_{ep}	18.2%	7.3%	3.8%
	remark		**5 pixel cut**	**20 px unclustered**
overall	f_b	32.7%	31.8%	9.7%
	K^{trans}	12.1%	11.7%	4.4%
	k_{ep}	26.5%	24.2%	6.2%
	remark		**1.4% px cut**	**1.3% unclustered**

4.5 Discussion

A local search clustering algorithm was developed to segment relative intensity-time curves of the DCE-MRI data. Unlike some other DCE-MRI clustering techniques [12,67,70] that aim at extracting a particular feature, the purpose of our clustering algorithm is to enhance the apparent sensitivity to Gd induced signal enhancement for detecting subtle changes in the barrier permeability. Simulation was performed to verify the necessity of clustering in low permeability DCE-MRI study.

In general, the DCE-MRI analysis is sensitive to noise in the concentration-time curve and can result in incorrect pharmacokinetic parameter estimation. Previous studies have demonstrated the effect of image noise on the results [45]. Galbraith et al. has reported more than 20% within-patient coefficient of variation (CV) in K^{trans} and k_{ep} estimates [11]. Poor reproducibility was also observed in a clinical study by Padhani et al. [18]. Jackson et al. reported an acceptable reproducibility ($< 7\%$ CV) in a glioma study [71]. But their study involved highly permeable tumor vasculature where sufficient CNR is expected. The current simulation employed a noise level of 4% Gaussian noise and 1% white noise in the DCE-MRI images. At high permeability ($K^{\text{trans}} > 0.01\text{min}^{-1}$), the RMS error in K^{trans} using pixel-by-pixel analysis was about 8% (see region 6 in Table 4.2). And this was considered to be acceptable in [71]. However, at low permeability ($K^{\text{trans}} < 0.01\text{min}^{-1}$), the RMS error in K^{trans} and k_{ep} was above 10% using pixel-by-pixel analysis. And the error was even above 20% in some regions (see region 4 and 5 in Table 4.2). One may reduce the amount of erroneous estimations by disregarding the estimates that yield high χ^2 values. However, as shown in Fig. 4.2, even if the fitted curve is a good match to the data, the result can still deviate much from the truth. Clustering for curve fitting can reduce the apparent noise within the clustered data. As a result, the errors were reduced by a half compared to analysis on individual pixel.

The algorithm assumes that permeability abnormality in CNS is spatially contiguous and is confined to small region. Under this assumption, the algorithm is allowed to form clusters locally in small regions. One disadvantage of the local search algorithm is that it has difficulty clustering small isolated regions as in region 3 and region 6 of the simulation. However, even if they were to be clustered, the small number of voxels would imply low CNR. This can increase the uncertainty of the estimated pharmacokinetic parameters. One way to circumvent this problem is to perform a global search with the distance classifier removed. However, global search demands extensive processing time and usually requires the number of clusters predefined to reduce the computation time. A predefined number of clusters can potentially impair the heterogeneity of DCE-MRI data. Besides, there is no physiological reason to group distant voxels into the same cluster.

In this work, a local search clustering algorithm was implemented to reduce the apparent noise of DCE-MRI data. Clustering for curve fitting is especially useful in CNS DCE-MRI where the contrast uptake is low and the resulting pharmacokinetic parameters are highly sensitive to noise. Simulations

have shown that the clustering algorithm can effectively reduce the error of the parameter estimates compared to using pixel-by-pixel analysis.

CHAPTER 5

ASSESSMENT OF BLOOD-SPINAL CORD BARRIER PERMEABILITY IN EXPERIMENTAL SPINAL CORD INJURY USING DYNAMIC CONTRAST-ENHANCED MRI

5.1 Introduction

This chapter describes the application of the improved acquisition and analysis of DCE-MRI techniques described in the previous chapters to investigate the BSCB permeability in experimental SCI. The long standing interest of our laboratory in the role of vasculature in SCI motivated this particular study.

The direct damage to the spinal cord that results from the initial impact is referred to as the primary injury in traumatic SCI. The initial compression on the spinal cord damages the blood vessels, axons and neurons. Release of excitatory amino acids from the disrupted neural membranes and the compromise of the BSCB initiates a secondary cascade that damages tissue away from the site of primary injury [72-75].

The secondary processes take place within minutes to hours following the primary insult. Secondary injury spreads both spatially and temporally, causing damage to tissue away from the site of primary insult. Vascular insult that includes BSCB barrier compromise is thought to be an important component of the secondary injury. The BSCB is a selective barrier that protects the spinal cord tissue by inhibiting blood borne substances from entering. Compromised BSCB allows abnormal leakage of intravascular cells and proteins into the tissue and can be harmful to the CNS [22,76,77]. The compromise of BSCB is not just confined to the initial site of injury, but spreads spatially [23,72,78-80]. With greater understanding of the spatial and temporal extent of increased BSCB permeability after SCI, it may be possible to develop treatments to arrest or attenuate its progression and repair the vasculature.

The BSCB permeability can be evaluated quantitatively with DCE-MRI [4,8,9,53,64,81]. Because DCE-MRI is minimally invasive, it has the advantage over other modalities that involve radiation such as computed tomography and positron emission tomography. However, even though the BSCB is compromised, the barrier is not completely dysfunctional, especially distal to the site of injury. At the distal locations, the intravascular tracer is still not allowed to enter the tissue freely; and as a result, the CNR in the DCE-MRI images is relatively low in the spinal cord tissue. This low CNR compounded with T_1 uncertainty and curve fitting variability will have negative influence on the accuracy of the permeability assessment.

5.2 Methods and Materials

The protocol of this study was reviewed and approved by the Institutional Animal Welfare Committee. The guidelines provided by the National Institutes of Health Guide for the Care and Use of Laboratory Animals were strictly followed.

5.2.1 Animals and Spinal Cord Injury Procedure

A total of 12 male Sprague-Dawley rats weighing 300-350 g were used in this study. All surgical procedures in this experiment were performed by trained professionals. Detailed surgical procedure was described in [82,83]. To perform the experimental SCI, the animal was first anesthetized at 5% isoflurane, 30% oxygen and medical grade air through an endotracheal tube for induction, and maintained under anesthesia with a mixture of 2.5% isoflurane, 30% oxygen, and medical grade air. Laminectomy was performed at the thoracic level 7 (T7). A moderately severe contusion injury was then inflicted to the exposed spinal cord using an Infinite Horizon Impactor (Precision Systems and Instrumentation, LLC, Lexington, KY). The injury device delivered a force of 150 kdyn with a dwell time of 1 sec to the spinal cord. In order to improve the SNR of the spinal cord images, a 11×35 mm RF coil was implanted over the injury location, stabilized with sutures, and tuned to the operating frequency of the MRI receiver.

5.2.2 Pre-MRI Preparation

MRI scans were performed 5 days post-injury. Prior to the MRI protocol, the left jugular vein was cannulated with a catheter for delivering the Gd tracer. Throughout the MRI session, the animal was anesthetized with 2.5% isoflurane, 30% oxygen and medical grade air through an endotracheal tube. The animal was then placed on a Plexiglas bed in supine position and secured by taping. An external coupling coil that was inductively coupled to the implanted coils was placed on the back of the animal for both RF pulse transmission and reception of the MR signal. Respiration and rectal temperature were monitored during the experiment with a physiologic monitoring unit (SA Instruments, Stony Brook, NY). The monitor unit consisted of a feedback heating mechanism to maintain the body temperature at 37°C. A pulse oximeter (Nonin Medical, Plymouth, MN) was used to monitor heart rate and oxygen saturation in the blood.

5.2.3 MRI Acquisition Protocol

A 2D dual echo fast spin echo (FSE) sequence (TR/TE = 3200/ 21, 64 msec) was acquired with 25.6×25.6 mm^2 FOV and a matrix size of 256×256. Twenty three axial slices of 1 mm thickness centered on the injury epicenter were acquired. The FSE images served as anatomical images that were used to identify and assess the lesion in the spinal cord. The T_1 map, B_1 map and the DCE-MRI images

were all acquired in 3D with FOV of $32 \times 25.6 \times 25.6\,\mathrm{mm}^3$ and the frequency encoding direction (first dimension) was along the length of the spinal cord to avoid wrap around artifact. The low resolution B_1 map was acquired to provide an approximated flip angle map for T_1 curve fitting. The B_1 map was acquired using the AFI described in section 2.3.2 (TR/TE = 20, 100/ 2.25 msec, flip angle = 45°, matrix size = $64 \times 32 \times 32$ interpolated to $64 \times 128 \times 128$). T_1 map was acquired using the modified 3D LL sequence with elliptical segmentation ($\tau = 11$ msec, $t_d = 10$ msec, $t_r = 1200$ msec, TE = 2.3 msec, $\alpha = 7.5°$, $N_{time} = 8$, $N_{TL} = 16$, $N_{dummy} = 5$, matrix size = $64 \times 64 \times 64$ interpolated to $64 \times 128 \times 128$). T_1 weighted DCE-MRI images were acquired using the view sharing scheme described in chapter 3 (TR/TE = 10/2.5 msec, flip angle = 10°, matrix size = $64 \times 128 \times 128$). Four fully sampled baseline images were acquired before tracer administration. A dose of 0.2 mmol/kg bolus of Omniscan (GE Healthcare, Oslo, Norway) was then injected within 2 sec through the catheter into the jugular vein while the data acquisition was in progress. A total of eighty post-contrast phase images were acquired.

5.3 Procedures of DCE-MRI Analysis

Multiple procedures were performed step by step to calculate the pharmacokinetic parameters. Briefly, T_1 map was first generated using the χ^2 weighed multi-step curve fitting procedure. The DCE-MRI data were constructed using the proposed normalization factor. The population AIF was then extracted from the DCE-MRI images. Segmentation was performed with the local search clustering algorithm. The clustered segments underwent a filtering process to remove sinusoidal artifacts. Finally, the extended compartment model described in Eq. 1.11 was fitted to the filtered DCE-MRI segments to obtain the pharmacokinetic parameters.

Several parameters were considered to be constants in this study and were adapted from the published literatures. The change in T_1 relaxation rate per tracer concentration of Omniscan was deduced from [84,85] and was set to $4.0\,\text{sec}^{-1}\,\text{mM}^{-1}$. The T_1 relaxation rate of blood was $0.45\,\text{sec}^{-1}$ and the hematocrit fraction was 0.45. Both of these values were obtained from [86].

5.3.1 Extraction of Arterial Input Function

AIF or C_b in Eq. 1.11 is required to calculate the contrast dynamic described by the two-compartment model. Accurate C_b is needed to separate the plasma contribution from the tissue uptake in the concentration-time course; and it is also the source of tracer uptake as:

$$C_{\text{pl}} = \frac{1}{1 - Hct} \cdot C_b \tag{5.1}$$

AIF was extracted from the DCE-MRI data automatically using a method similar to that described in [2,16]. First, the algorithm searched for voxels with their relative intensity-time curves monotonically falling after the first 30 sec of post-contrast phase. It is expected that the AIF reaches its peak within the first 10 sec following tracer administration. Therefore, a voxel composed of vessels should have the relative intensity-time curve in its washout phase of the tracer. These voxels were considered to be the possible candidate voxels for extracting the AIF. Only the top 128 candidates that yielded the highest peak tracer concentration (enhancement within the first 2 min post-contrast phase) were chosen for the next step. Ideally, each of these voxels would contain vessels only. Unfortunately, the small size of vessels introduces significant partial volume effect. Therefore, the concentrations in these candidate voxels are generally lower than the concentration in an actual vessel. Assuming that the voxel composed of only vessel should have the highest peak tracer concentration, the peak tracer concentration of all candidate voxels were normalized to the highest peak tracer concentration within all the candidates. Normalization can reduce the effect of partial volume and avoid the underestimation of intravascular tracer concentration. The concentration of a candidate voxel $C_i(t)$ was normalized to $C_{i,\text{norm}}(t)$ following:

$$C_{i,\text{norm}}(t) = \frac{\sum_{t<2\text{min}} C_{\text{ref}}(t)}{\sum_{t<2\text{min}} C_i(t)} C_i(t) \tag{5.2}$$

The first 2 min of post-contrast phase corresponded to three time points in our DCE scan. 2 min was chosen instead of shorter time because multiple time points are needed to reduce the effect of noise. To further reduce the effect of noise on normalization, the reference concentration-time curve $C_{\text{ref}}(t)$ must have the highest peak concentration that satisfied the following requirement: there must be at least one other vessel curve with peak concentration within 2% above and at least one within 2% below the reference peak concentration. This constraint ensured that the chosen peak concentration was not a result of random noise. After normalization, only half of the vessel candidates that yielded the lowest washed out concentrations were used to compute the AIF.

The AIF was then fitted to a bi-exponential function [64]. Since it has been shown that using the average AIF from the entire group produces more consistent result [16], the population AIF was computed and applied to all subjects in the study.

From this experiment, the population AIF was fitted to the following bi-exponential form:

$$C_{\text{b}}(t) = 0.29e^{-0.22t} + 0.55e^{-0.016t} \tag{5.3}$$

The unit of the concentration is in mM and t is expressed in min. Although having the same magnitude, the coefficients in Eq. 5.3 are slightly different from those reported in [64]. These differences are expected due to the differences in the DCE-MRI protocol and higher tracer dose administered in this study.

5.3.2 DCE-MRI Clustering

The DCE-MRI data were clustered to increase the apparent CNR in order to improve the consistency of the results. Manual contouring of the spinal cord was performed on twenty-seven slices (13.5mm) centered at the lesion epicenter. The contouring was needed to avoid the inclusion of the meninges during the analysis. The clusters were generated using the local search clustering algorithm with the following parameters: ($\Delta T_1 = 250$ msec, $\Delta\text{Dis} = 2.5$ vox, $f_{\text{thre}} = 3$, N_{min} to form segment $= 4$, N_{max} to stop recruit $= 9$). The threshold to group the left-out voxel was also set to 3.

5.3.3 Sinusoidal Artifact Removal

One common artifact observed in the DCE-MRI images is the presence of signal oscillations that appeared in random part of the spinal cord. This oscillating artifact is not related to BSCB permeability and can significantly compromise the final results. Since the signal oscillations appeared periodic, a multi-taper spectral analysis described in [87,88] was applied to remove the oscillating components in the data. The multi-taper spectral analysis was used to estimate the spectrum of a finite discrete time series with statistical significance.

The multi-taper spectral analysis was performed on the clustered relative intensity-time curve tapered by the discrete prolate spheroidal sequences (DPSS). First, the average increase in intensity was subtracted from the relative intensity-time curve to emphasize the periodic components. The relative intensity-time curve was then zero padded from 80 time points to 256 time points to increase the pseudo-resolution of the data in the frequency space. DPSS ($N_{time} = 256$, $N_{time}W_{band} = 7$) were multiplied with the processed curve before being transformed to the frequency space. If the F-statistics of a frequency exceeded the 5% cutoff, it would become a potential sinusoidal component. To further verify if this potential frequency component was indeed statistically significant, the non-padded tapered curve ($N_{time} = 80$) was phase-shifted to this potential frequency before Fourier transformation. If this potential frequency in the non-padded frequency space also had its F-statistics exceed the 5% cutoff, it was considered as an actual periodic component in the relative intensity-time curve. The amplitude and phase of this frequency component were then computed in the non-padded transformed space. All actual periodic components identified were removed from the relative intensity-time curve for the final DCE-MRI analysis.

As an example, a relative intensity-time curve of a clustered data was shown in Fig. 5.1. As shown in this figure, there was an obvious sinusoidal component present in the relative intensity-time course. This periodic component was unlikely to be the result of change in BSCB permeability and it would affect the final results if it is not accounted for. In this example, the multi-taper spectral analysis identified the periodic component with period of 27 min and amplitude of 0.16 in relative intensity change as statistically significant. The periodic component was removed from the intensity-time curve and this curve was used to compute the final pharmacokinetic parameters.
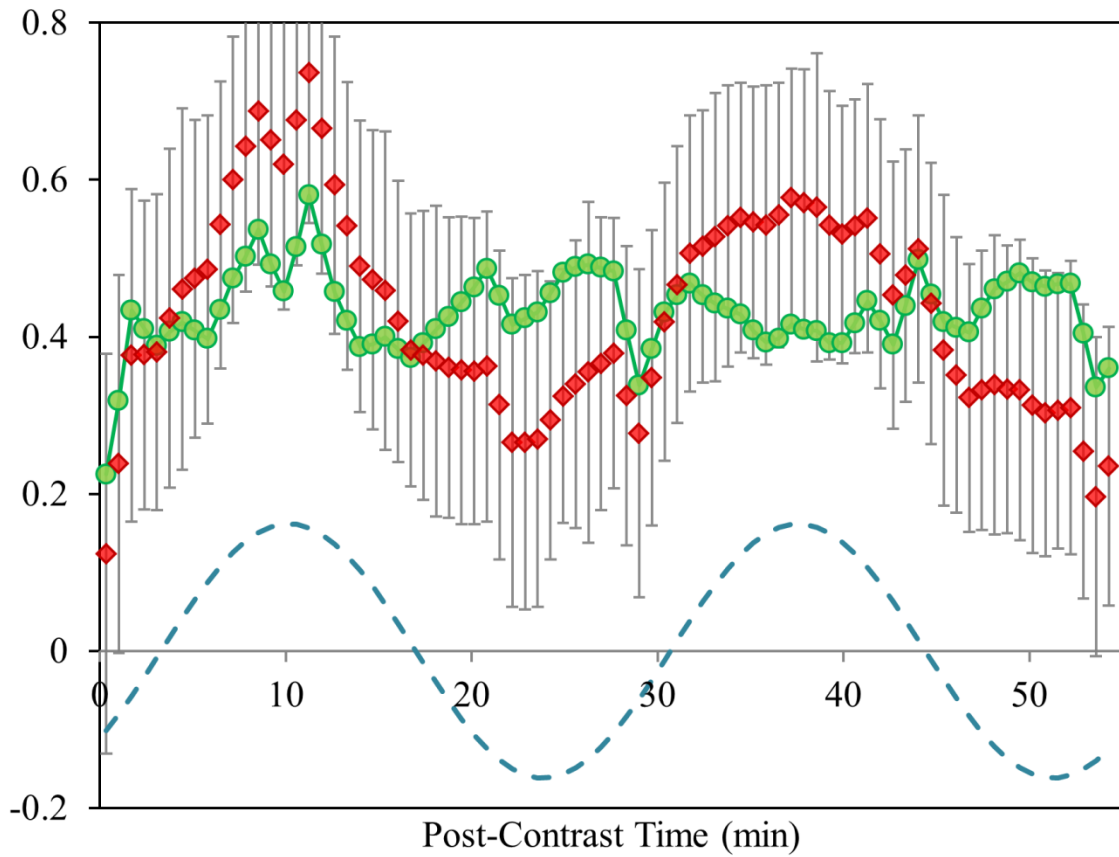
Figure 5.1 The time evolution of change in relative intensity of a clustered segment. The average change in the cluster at each time point (red rhombus) is presented with its standard deviation. The multi-taper analysis was able to identify the sinusoidal component (blue dashed line) in the relative intensity-time curve. The difference (green circle) obtained by subtracting the periodic curve from the data was used for final curve fitting.
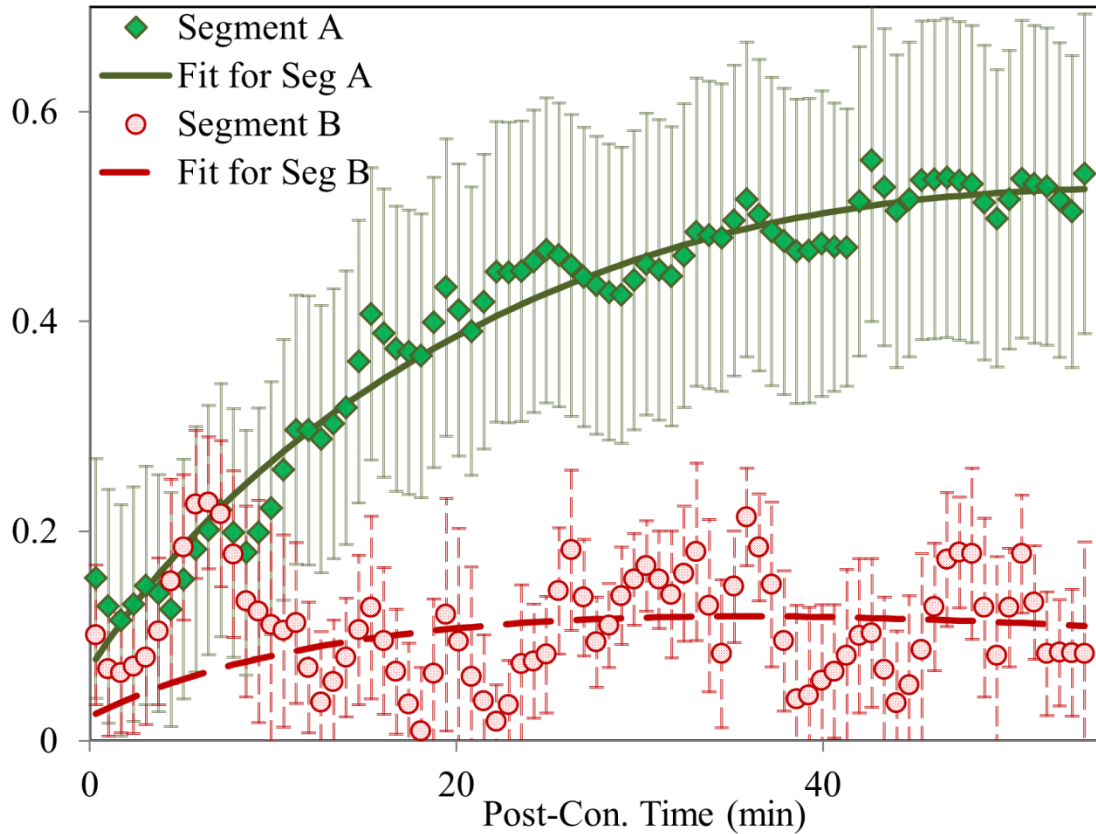
5.3.4 Curve Fitting Requirement

The pharmacokinetic parameters of each cluster were computed with three-parameter curve fitting (f_b, K^{trans} and k_{ep}) using Eq. 1.11. In order to reduce the estimation error as a result of false curve fitting, multiple requirements were incorporated to eliminate concentration-time curves that showed high χ^2 values. The estimated K^{trans} and k_{ep} of a cluster were rejected if 1) the three-parameter fit yielded the overall χ^2 statistics above 10% cutoff and 2) the fitted curve in the first 8 min post-contrast phase had χ^2 above 10% cutoff. Extra requirement is applied on the first 8 min because the final curve fit is most sensitive to the early post-contrast phase and the early phase is also more clinically relevant. Fig. 5.2 shows two examples of curves fitted to their respective DCE-MRI data clusters. One data set passed the χ^2 requirement, while the other one did not and was rejected. In Fig. 5.2, the general curve fit of the rejected data was visually acceptable and it passed the overall χ^2 requirement. However, its early phase deviated greatly from the rest of the data and that did not pass the χ^2 requirement in the first 8 min post-contrast phase.

Within a voxel, both the tissue uptake and the AIF contribute to the relative intensity change. Because the tissue uptake rate could be very small, there were voxels with relative intensity-time curves that showed more AIF than tissue uptake characteristics. The tissue uptake component in these cases is very difficult to resolve. Extra requirements were therefore applied to disregard curves that exhibited more AIF characteristics. First, the relative intensity of the cluster was fitted to the AIF function to obtain the χ^2 value of the AIF fit. The χ^2 value of the regular three-parameter fit was then compared to the χ^2 value of the AIF fit. If the χ^2 value of the AIF fit was smaller, that would imply the concentration-time curve was better fit to the AIF than tissue uptake. The estimated K^{trans} and k_{ep} were therefore rejected. In addition, the curve with small tissue uptake was expected to have slowly rising intensity. Therefore, the fitted curve was rejected if it did not ascend for more than 3 min. Curves that ascended for less than 3 min would imply very high K^{trans} and k_{ep} and were likely to be results of venous blood or cerebrospinal fluid (CSF). Fig. 5.3 shows an example of a rejected curve that did not show obvious tissue uptake. This curve was rejected because the three-parameter fitted curve was monotonically decreasing throughout the whole DCE-MRI course.

On average, about 16% of the clustered voxels were rejected. All the rejected segments and unclustered voxels would be treated as regions with unknown pharmacokinetic parameters.

Figure 5.2 Examples of relative intensity change-time curves of two clustered segments and their respective fitted curves. The curve fit to segment A was accepted because it passed all the χ^2 requirements. The curve fit to segment B however was rejected. The fitted curve for segment B passed the χ^2 requirement for the whole curve but the χ^2 value in the first 8min was above the statistical cutoff. It can be seen that the data of segment B in the early phase deviated greatly from the rest of the data. It would be very difficult to fit a valid two-compartment model to this data and therefore the curve fitting result of segment B was disregarded.
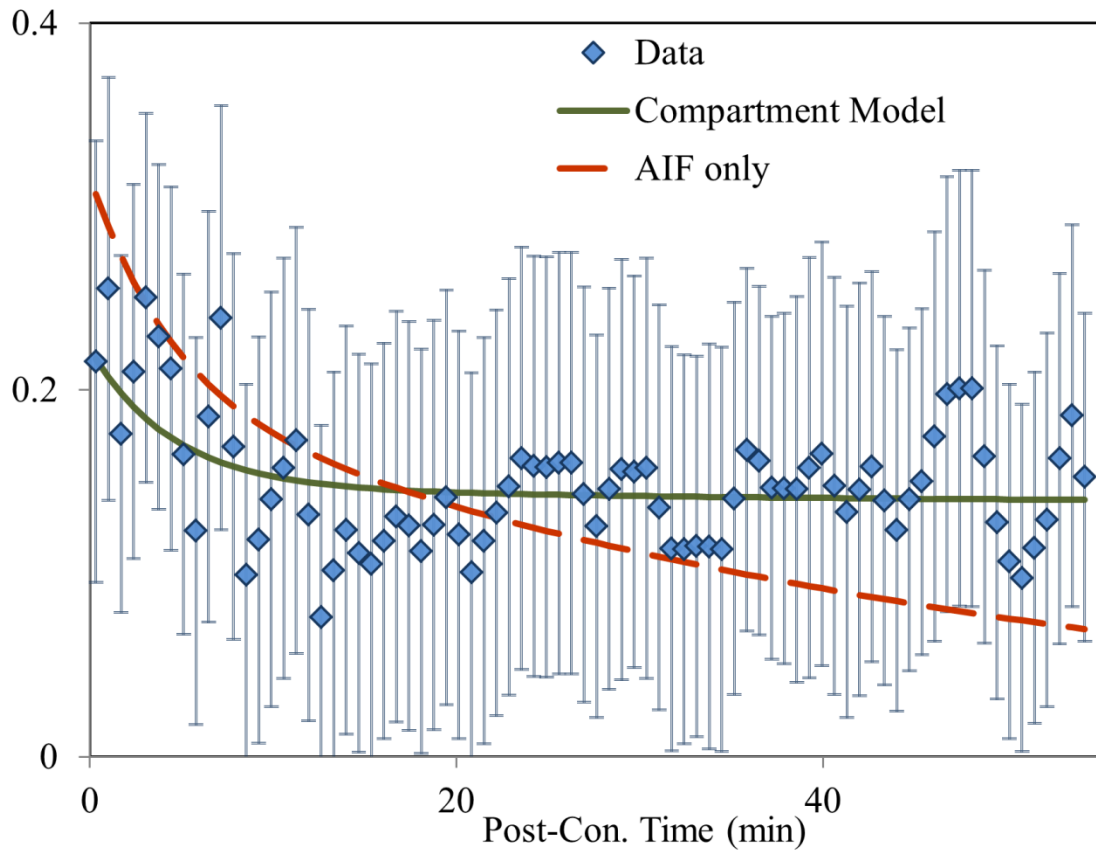
Figure 5.3 Example of relative intensity change-time curve with the 3-parameter curve fit (compartment model) and the 1-parameter curve fit (AIF only). Both curve fits passed the χ^2 cutoff and the 3-parameter fit was a better fit than the 1-paramenter fit. However, the 3-parameter fit did not pass the requirement of rising curve as it lacked the trend of increasing enhancement throughout the whole experiment period. It would be difficult to distinguish if there is any uptake component in this data set and therefore the result from this data set was disregarded.

5.4 Results

5.4.1 In Vivo Spinal Cord T_1 Map

Fig. 5.4 shows an example of the T_1 maps of two spinal cord sections and representative LL data. All the curves in the example show good agreement with the data. Based on the examination of several slices located more than 1.5 cm away from the injury epicenter, the average T_1 value of the gray matter (GM) was 1252 ± 69 ms; and the average white matter (WM) T_1 value was 1098 ± 85 ms. These values were in reasonable agreement with other published literature [89]. The epicenter which appeared hyper-intense on the T_2-weighted images had higher T_1 values, indicating a possible edematous environment.

When examining the results using different flip angle maps, the proposed χ^2 weighted multi-step curve fitting procedure generally produced better fit to the LL recovery data compared to using the prescribed angle (7.5°) and the angle corrected by the B_1 map obtained from the AFI acquisition. Fig. 5.5 illustrates the effect of flip angle on the curve fitting result. The curve fits of the lesion data in Fig. 5.4b are plotted using different angles obtained from three different methods. In this example, the multi-step method produced flip angle of 9.8° and resulted in T_1 of 1640 msec. The B_1 corrected angle was 8°, and yielded T_1 of 1380 msec. Although the B_1 map corrected some of the flip angle discrepancy, it was not sufficient as the estimated T_1 was still very close to the normal GM T_1 value.

Although the variation in the inversion angle was found to be higher than that in the phantom study, the variation had a relatively small effect on the T_1 estimation.
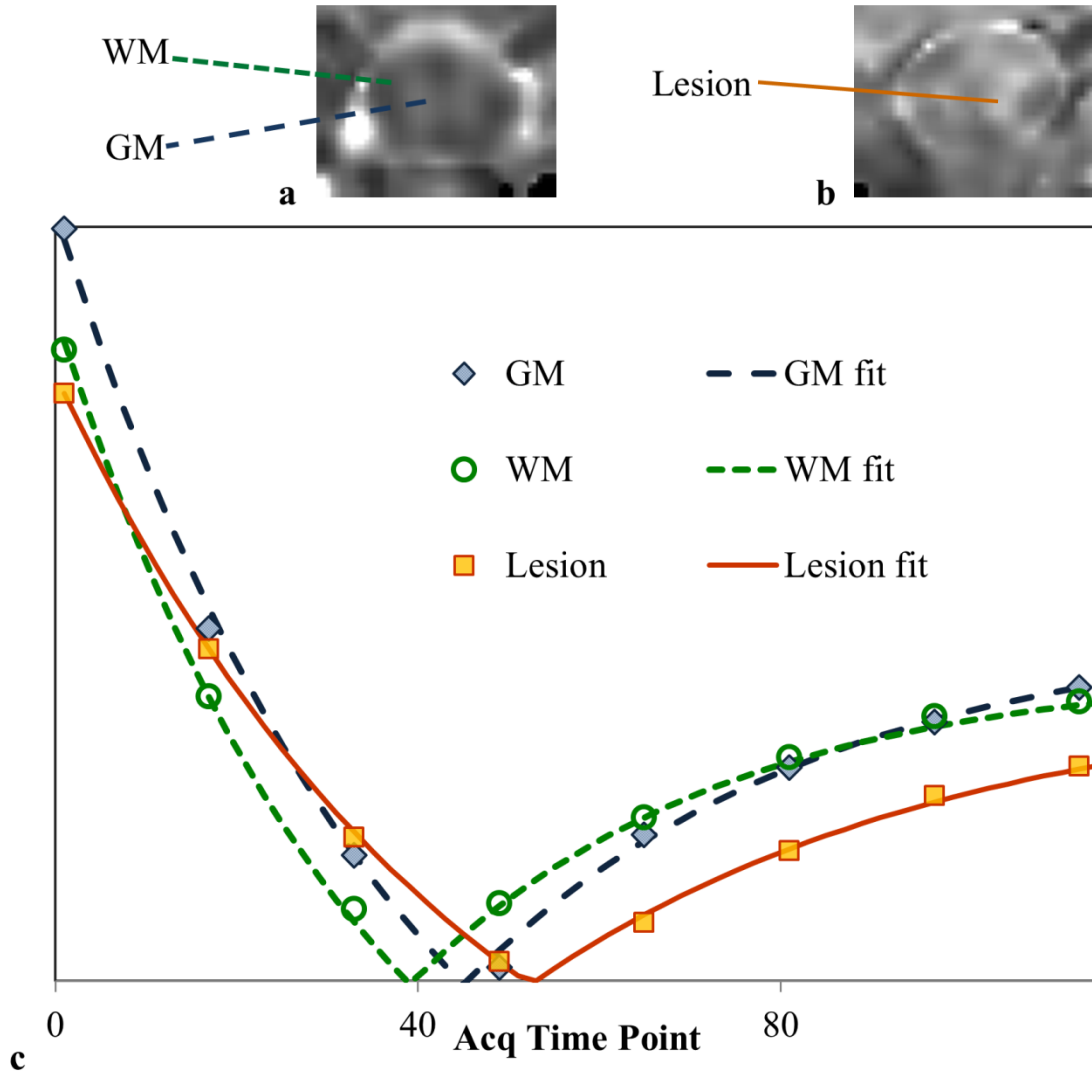
Figure 5.4 T_1 map of the spinal cord cross section and examples of representative LL recovery curves. The spinal cord images shown were located at a) 15 mm caudal to the epicenter and b) at the injury epicenter. c) T_1 recovery curves of three different tissue types are shown. Computed using the χ^2 weighted multi-step method, the GM data yielded $T_1 = 1258$ msec, $\gamma = 177.0°$, $\alpha = 10.4°$; the white matter data yielded $T_1 = 979$ msec, $\gamma = 178.6°$, $\alpha = 10.8°$ and the lesion data yielded $T_1 = 1648$ msec, $\gamma = 178.2°$, $\alpha = 9.8°$.
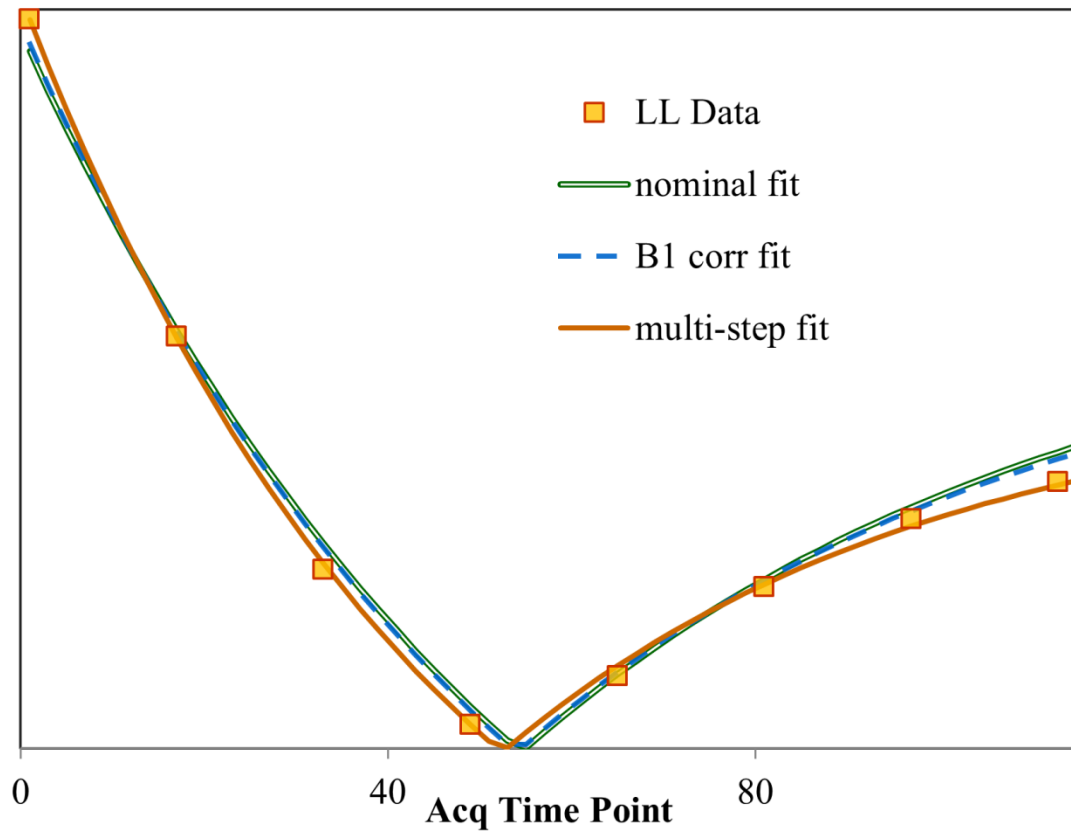
Figure 5.5 T_1 recovery curves of the lesion data in Fig. 5.4b using three different flip angles for curve fitting. All three curves were fitted with $\gamma = 180°$, and were computed with the identical two-parameter fitting procedure. The nominal fit used the prescribed 7.5°, yielded $T_1 = 1258$ msec with $\chi^2 = 4.6$. The flip angle used in the B_1 corrected fit was corrected by the acquired B_1 map. The corrected angle was 8.0° and the results were $T_1 = 1383$ msec with $\chi^2 = 2.9$. With the χ^2 weighted multi-step method, the estimated flip angle was 9.8° and the results were $T_1 = 1646$ msec with $\chi^2 = 0.3$.

5.4.2 DCE-MRI Analysis

Representative images of the DCE-MRI time series at the injury epicenter are shown in Fig. 5.6. In the DCE-MRI scans, the meninges consistently exhibited substantial enhancement due to the absence of BSCB in this structure. The parenchyma however showed relatively little enhancement even in the presence of injury. Tracer uptake in the CSF around the meninges was shown to be independent of the injury [8]. Careful contouring is therefore necessary to exclude the highly permeable surrounding meninges from the spinal cord tissue; otherwise, the tissue permeability would be overestimated by the contamination of meninges permeability.

On average, 72% of voxels inside the contoured spinal cord showed positive change in intensity ($p < 0.05$) after tracer administration. After segmentation, 81% of voxels were clustered into segments. About 7% more voxels were being clustered than the number of positively enhanced voxels. As mentioned before, although clustering starts with a positive enhanced voxel, the algorithm is allowed to include voxels that did not pass the t-test. The clustered voxels that did not pass the t-test were likely recruited by clusters with only slight increase in intensity.

Out of the three parameters calculated from the DCE-MRI analysis, the transfer constant K^{trans} is closely related to the BSCB permeability to the tracer. The rate constant k_{ep} is a combination of two biological effects: 1) the ability to clear out the tracer after it entered the spinal cord and, 2) the fractional volume of EES.

Overall, about 68% of the contoured spinal cord showed positive K^{trans} and k_{ep} values. Fig. 5.7 shows examples of K^{trans} and k_{ep} maps overlaid on the spinal cord T_1 map. In Fig. 5.7a, high K^{trans} value can be observed at the epicenter of SCI and the value decreased in slices away from the epicenter. Within the same slice, the dorsal side always had higher K^{trans} value than the ventral side. Fig. 5.7b shows the k_{ep} spatial distribution of the spinal cord. The calculated k_{ep} distribution was completely opposite to that of K^{trans} as the k_{ep} value was lower at the epicenter and at the dorsal part
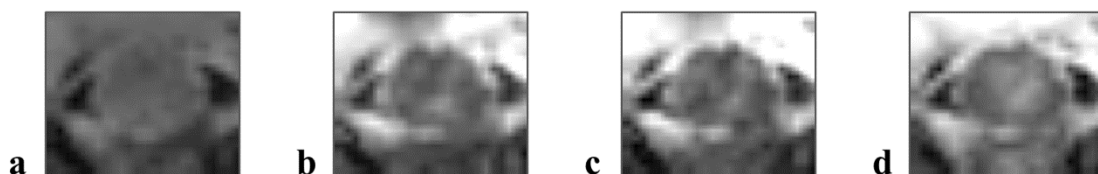
Figure 5.6 DCE-MRI images of the spinal cord at the injury epicenter: 1) Pre-contrast baseline image; b-d) Post-contrast images at 20 sec, 100 sec and 20 min after tracer delivery. The meninges surrounding the spinal cord enhanced shortly after tracer administration, while the muscle at the dorsal (top of images) enhanced relatively slower. The enhancement within the spinal cord parenchyma was smaller by comparison.

of the spinal cord.

To further investigate the distributions of K^{trans} and k_{ep} at different locations within the spinal cord, the average percentile values as a function of distance from epicenter were calculated. The percentile of the parameter was computed based on the volume of each spinal cord segment in each subject. The average percentile was the averaged percentile over all the animals included in this study. Fig. 5.8 shows the average percentile values of the K^{trans} estimate and Fig. 5.9 shows the average percentile values of k_{ep}. The injury epicenter (0 mm) was identified from the location of laminectomy. Each segment was composed of 1.5 mm or three slices of spinal cord MRI. From Fig. 5.8, the BSCB permeability declined away from the epicenter. In addition, the permeability in the caudal section appeared to be higher than that in the rostral section. Fig. 5.9 shows lower k_{ep} around the epicenter, and higher k_{ep} away from it. The rate constant was slightly higher in the rostral region, but it appears that the asymmetry was mostly a result of the unusual bloom in k_{ep} value around the rostral 1.5 mm section. Unlike the K^{trans} distribution, which had similar percentile range along the spinal cord, the percentile range of k_{ep} values was smaller at the epicenter and noticeably wider away from it.

The average percentiles of K^{trans} and k_{ep} are summarized in Table 5.1 and Table 5.2 respectively. In terms of percent standard deviation, the inter-subject variation of k_{ep} was on average higher than K^{trans}. The inter-subject variation of K^{trans} was generally higher at the epicenter. k_{ep} variation on the other hand was generally lower around the epicenter. The unusually high k_{ep} around the +1.5 mm section also presented higher inter-subject variation than its neighboring regions.

caudal ←——————————— epicenter ——————————→ rostral

a

K^{trans} $8\times10^{-3}\text{min}^{-1}$

0min^{-1}

k_{ep} $5\times10^{-2}\text{min}^{-1}$

caudal ←——————————— epicenter ——————————→ rostral

b
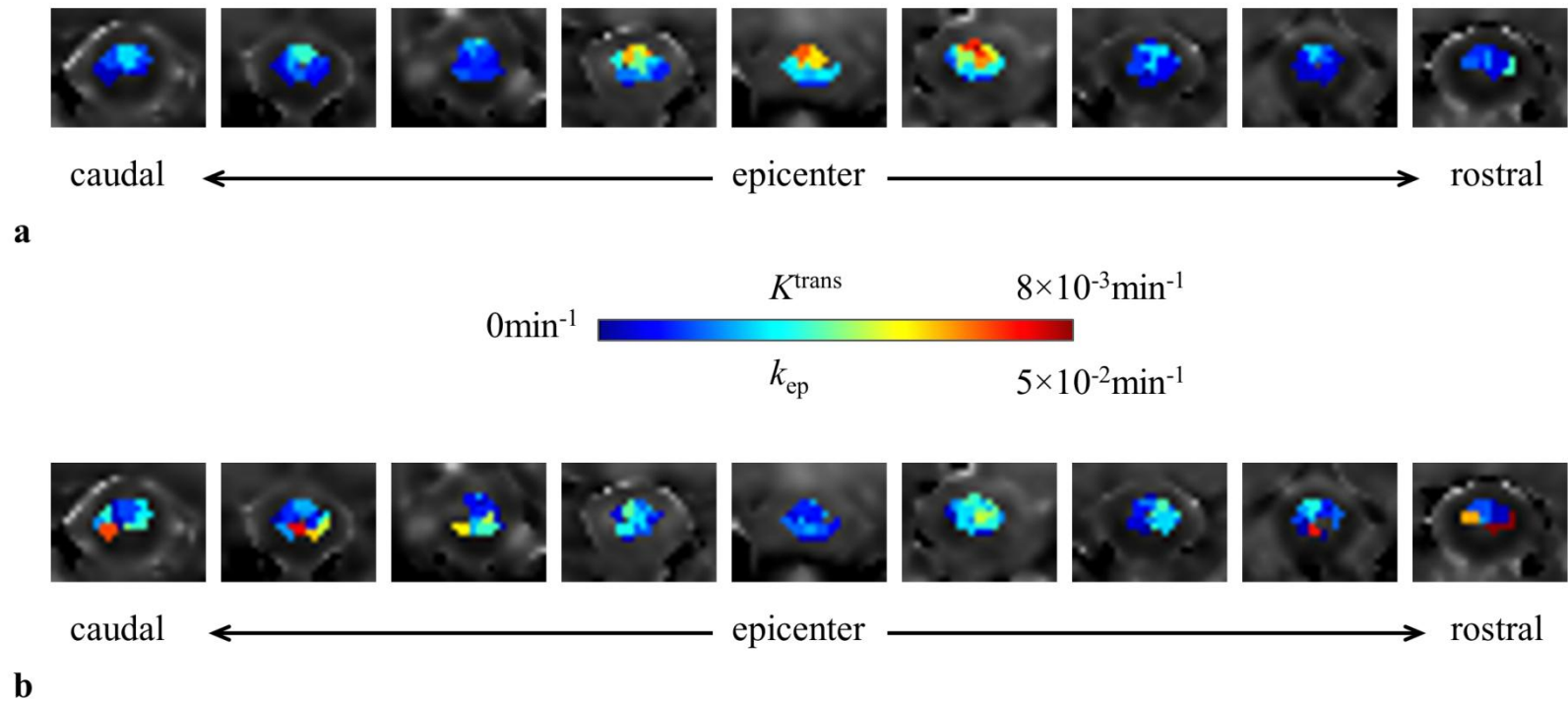
Figure 5.7 Example of pharmacokinetic parameters of the spinal cord after SCI. Injury was at the epicenter in the dorsal side (top of image) of the spinal cord. From caudal to rostral, each image is separated by 1.5 mm. a) The K^{trans} map overlaid on the T_1 map. High K^{trans} value was seen at the dorsal part of the spinal cord and at the injury epicenter. b) The k_{ep} map of the same regions of the spinal cord. Contrary to K^{trans}, k_{ep} value was lower at the epicenter and dorsal of the spinal cord.
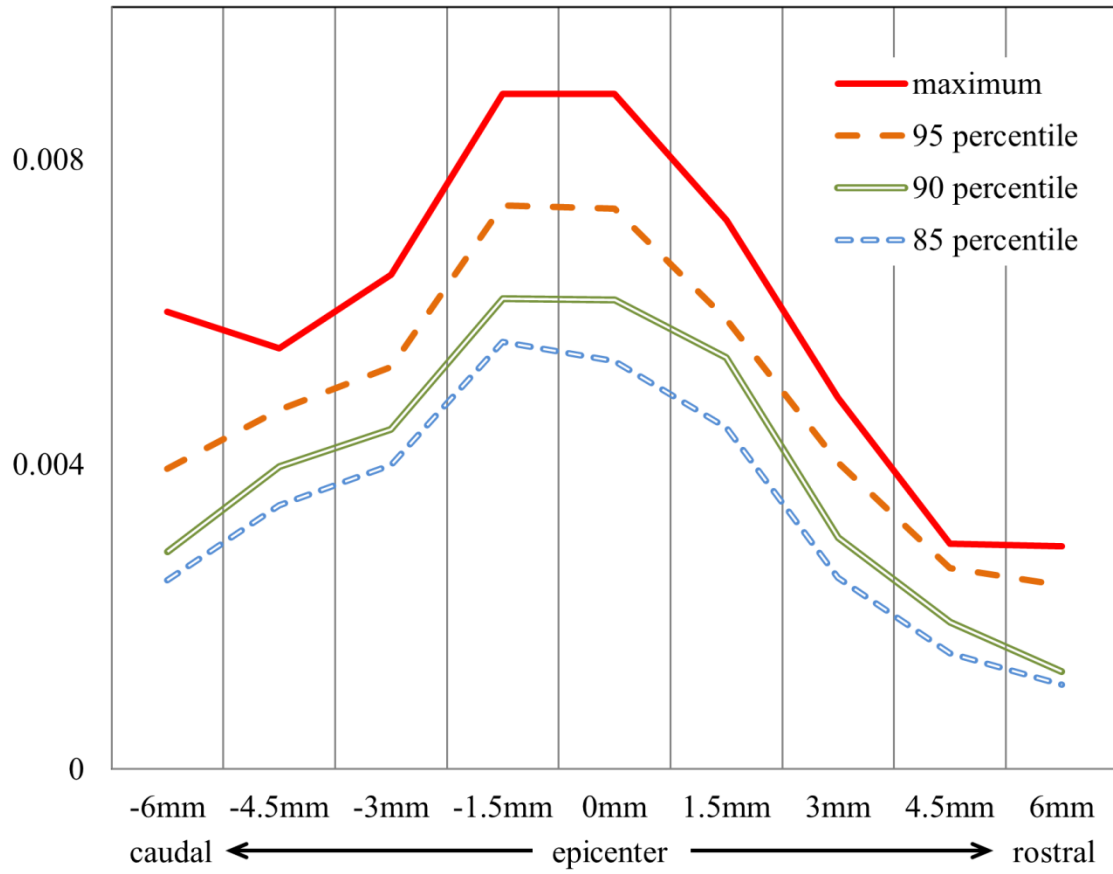
Figure 5.8 The different percentiles of the K^{trans} values (in min^{-1}), averaged over all animals. The transfer constant was highest at the epicenter and decreased away from it.
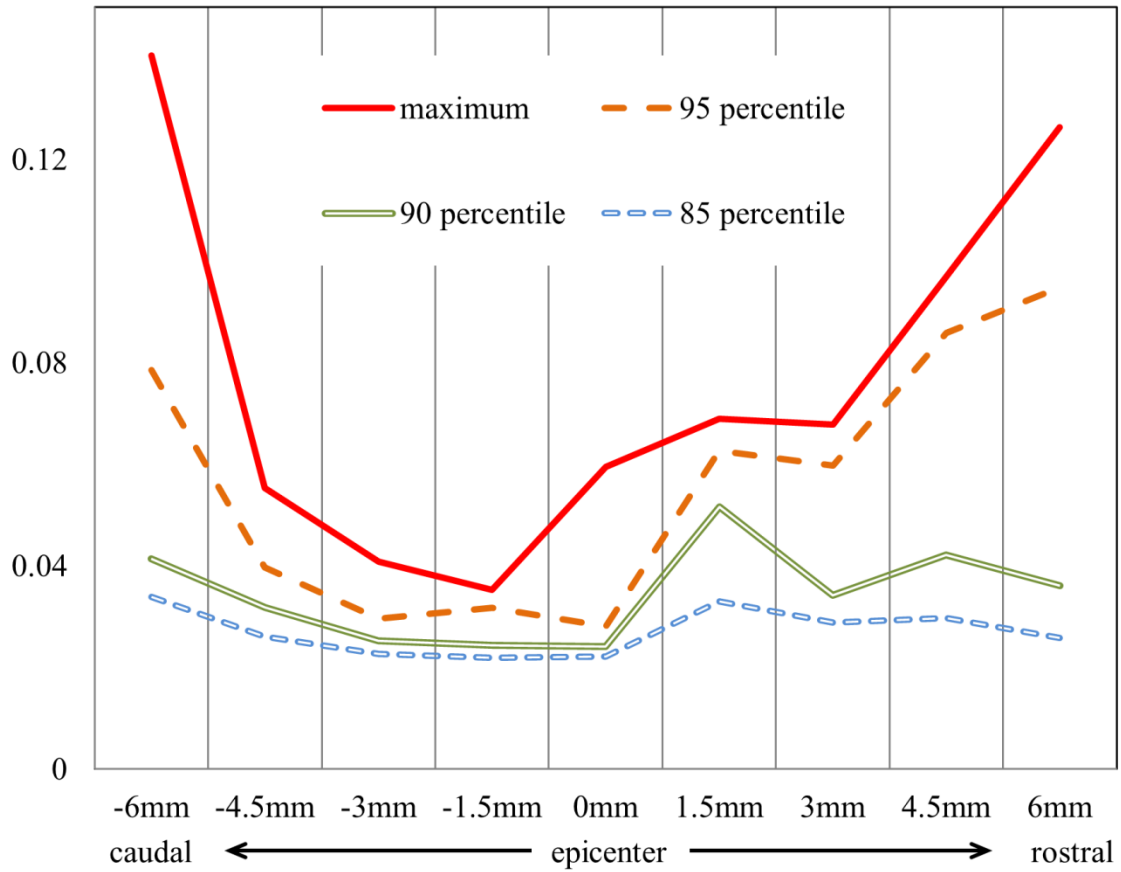
Figure 5.9 The different percentiles of the k_{ep} values (in min^{-1}), averaged over all animals. The rate constant was lowest around the epicenter and increased away from it.

Table 5.1 The average percentiles of the K^{trans} values in all subjects (in $10^{-3}\,min^{-1}$).

Position (mm)	-6	-4.5	-3	-1.5	0	1.5	3	4.5	6
Maximum	6.0 ± 3.7	5.5 ± 2.4	6.5 ± 2.6	8.9 ± 3.7	8.9 ± 4.5	7.2 ± 3.6	4.9 ± 2.3	3.0 ± 1.2	2.9 ± 2.1
95 percentile	3.9 ± 1.5	4.7 ± 1.8	5.3 ± 1.8	7.4 ± 3.6	7.4 ± 4.3	5.9 ± 2.8	4.0 ± 1.8	2.6 ± 1.2	2.4 ± 2.4
90 percentile	2.9 ± 1.3	4.0 ± 1.7	4.5 ± 1.9	6.2 ± 3.1	6.2 ± 3.5	5.4 ± 2.6	3.0 ± 1.8	1.9 ± 0.9	1.3 ± 0.8
85 percentile	2.5 ± 1.2	3.5 ± 1.4	4.0 ± 1.7	5.6 ± 2.9	5.4 ± 3.0	4.5 ± 2.4	2.5 ± 1.5	1.5 ± 0.7	1.1 ± 0.9

Table 5.2 The average percentiles of the k_{ep} values in all subjects (in $10^{-2}\,min^{-1}$).

Position (mm)	-6	-4.5	-3	-1.5	0	1.5	3	4.5	6
Maximum	14.0 ± 13.5	5.5 ± 3.1	4.1 ± 1.1	3.5 ± 1.1	6.0 ± 6.1	6.9 ± 6.1	6.8 ± 5.6	9.7 ± 8.3	12.6 ± 11.9
95 percentile	7.9 ± 9.6	4.0 ± 1.2	3.0 ± 0.8	3.2 ± 1.2	2.8 ± 1.2	6.3 ± 6.3	6.0 ± 6.0	8.6 ± 8.7	9.5 ± 11.9
90 percentile	4.1 ± 2.9	3.2 ± 0.8	2.5 ± 0.8	2.4 ± 0.6	2.4 ± 1.2	5.2 ± 6.3	3.4 ± 1.2	4.2 ± 2.3	3.6 ± 3.2
85 percentile	3.4 ± 2.7	2.6 ± 0.8	2.3 ± 0.8	2.2 ± 0.6	2.2 ± 1.1	3.3 ± 1.6	2.9 ± 1.0	3.0 ± 1.4	2.6 ± 2.2

5.5 Discussion

The BSCB permeability in experimental SCI is investigated. Traditionally, BSCB integrity is determined by administering intravascular proteins or molecules that can cross the compromised barriers [23,90-92]. Such method requires animals to be sacrificed for histological evaluation. In contrast, DCE-MRI has the advantage of collecting in vivo data that allows longitudinal assessment on the same animals. In addition, the size of Gd tracer (Omniscan 0.6 kDa) is smaller than the size of these intravascular proteins (Evans blue/albumin 70 kDa), making it more sensitive for detecting subtle changes in the BSCB permeability.

DCE-MRI enables quantitative measurement of the barrier permeability. However, as shown through simulations and MRI studies on phantom, DCE-MRI needs significant improvements both in acquisition and analysis strategies for robust estimation of the pharmacokinetic parameters. In these in vivo studies, we have incorporated all these improvements. I believe that this distinguishes the current study from the previous studies. While the current studies are in qualitative agreement with the published studies, a quantitative comparison is quite difficult in the absence of ground truth.

The pharmacokinetic parameters K^{trans} and k_{ep} were investigated in this study. By definition of the two-compartment model, K^{trans} represents the vascular permeability into the tissue and k_{ep} is equal to the clearance rate divided by the EES volume. It is expected that the permeability would be higher closer to the site of the primary injury. In the current study, K^{trans} was higher closer to the dorsal side and at the epicenter as shown in Fig. 5.7. k_{ep} followed an opposite trend as k_{ep} was higher closer to the ventral side and away from the epicenter. This likely indicates higher EES volume as a result of necrotic tissue near the site of initial trauma.

To compute the average values of all animals, we decided to show different percentiles of the K^{trans} and k_{ep} values because the percentiles are less likely to be affected by low CNR and it allows the visualization of the distribution of these parameters along the length of the spinal cord. One interesting observation in this experiment is that K^{trans} is on average higher towards the caudal side than to the rostral side. The caudal-rostral asymmetry was observed in a recent study by Cohen et al. [9], where their DCE-MRI showed average K^{trans} value in the caudal area to be higher than that in the rostral area 3 days after SCI. DTI study by Deo et al. has also presented caudal-rostral asymmetry [93]. They found that after SCI, the caudal section had lower fractional anisotropy (FA) values than the rostral section. Our observation of higher vascular permeability in the caudal section may be a contributing factor in lower FA values. It is also worth noting that some animals presented isolated area with high K^{trans} away from the epicenter. As an example, Fig. 5.7a shows an isolated region with higher K^{trans} (light blue) in the caudal side. Interestingly, most of these isolated higher permeability regions are caudal to the epicenter.

The asymmetric pattern after SCI was also seen in some histological studies on oxidative stress. Like compromised BSCB, oxidative stress is a secondary injury in SCI. Baldwin et al. have detected greater number of 4-hydroxynonenal/protein positive neurons in the caudal sections compared to the rostral sections 2 days after SCI, indicating an asymmetry in lipid peroxidation [94]. Aimone et al. have observed an up-regulation of osteopontin, a gene related to oxidative stress-induced angiogenesis, in the caudal and epicenter segments from 4 hours to 35 days after SCI [95].

One possible artifact that might falsely contribute to the asymmetry was the lower SNR in the rostral region. As the cervical section of the spinal cord was relatively far away from the implanted coil, the sensitivity suffered. As shown in Table 5.1, the low SNR and CNR in the rostral distal end led to higher inter-subject variation in K^{trans}. However, the average percentile should be rather insensitive to SNR as it did not take into account of low uptake values. Moreover, low SNR could not explain the higher K^{trans} at -1.5 mm compared to +1.5 mm, where the SNR should be very similar.

The low k_{ep} values observed at the epicenter can perhaps be explained by the larger volume of EES due to necrotic tissues. Conversely, the higher k_{ep} values at the distal ends can be explained by smaller EES because of the higher population of intact cells. The range of k_{ep} values was larger at both distal ends compared to the range at the epicenter. One of the reasons may be because the k_{ep} value is related to both EES and clearance rate. Since the permeability is small at distal ends (almost normal tissue), the k_{ep} could also be small. There was an increase in k_{ep} that appeared localized to the region immediately rostral to the epicenter. The increased k_{ep} in this particular area could potentially indicate better tissue repair at the immediate rostral region. As shown in Table 4.2, the error in k_{ep} estimation is generally higher than in K^{trans}. This leads to the high inter-subject variability in k_{ep} values. Therefore, it is possible that the high k_{ep} observed at +1.5 mm is also a result of the high k_{ep} variability.

One of the observations made in this study was the periodic artifact in the relative intensity change-time curve in some clustered DCE-MRI segments. These artifacts occurred in isolated parts of the spinal cord and did not appear to be associated with the barrier permeability. This oscillation is difficult to notice in normal clinical DCE-MRI study because the period of the oscillation was relative long compared to the scan time. However, the oscillation can have significant effect on the pharmacokinetic parameters.

A potential source of signal oscillation is the temperature fluctuation within the rat. It is known that the primary relaxation mechanism in spin-lattice relaxation depends on transfer of thermal energy [96]. Since the intensity in DCE-MRI is directly related to T_1, the change in temperature can have great impact on the calculation of tracer concentration. In the example shown in Fig. 5.1, the oscillation component had amplitude of 0.16 in relative intensity change and the average intrinsic T_1 in this segment was 1230 msec. If the intensity oscillation was a result of T_1 oscillation alone, T_1 would

need to fluctuate between 1060 msec to 1470 msec. According to [97], such T_1 fluctuation would approximately correspond to 20°C change in temperature. However, it is very unlikely that the temperature changed by this extent within the spinal cord. Further study must be conducted to investigate this periodic artifact.

Chapter 6

CONCLUSIONS AND FUTURE DIRECTIONS

6.1 Conclusions

Quantitative DCE-MRI is an important tool for measuring vascular permeability. Unfortunately, large variability in the estimated pharmacokinetic parameters has been observed in published literatures. A number of factors can affect the accuracy of DCE-MRI analysis. These include the baseline T_1 value [45], temporal sampling rate [21], spatial resolution [19], and noise. The work presented in this thesis has three innovative features for improving DCE-MRI. The innovations include 1) modifications of the fast T_1 mapping method; 2) view sharing method for improved temporal resolution; 3) clustering analysis to reduce apparent noise. These methods, through simulations and phantom studies were shown to yield more robust results in DCE-MRI. Finally, these methods were applied to investigate the BSCB permeability in experimental SCI.

The tracer concentration is proportional to the inverse of intrinsic longitudinal relaxation time (see Eq. 1.7). As a result, the uncertainty in K^{trans} estimate increases with the error in T_1. In this study, the 3D LL sequence was implemented to provide T_1 estimations. I optimized the k-space segmentation scheme and developed a χ^2 weighted multi-step curve fitting procedure to reduce reconstruction and estimation errors. These improved techniques were shown to provide more accurate T1 estimation. Phantom study has shown that the standard deviation of T_1 measurement was less than 2% on average in normal circumstances. One drawback of the 3D LL sequence is the reconstruction artifact at the edges. The elliptical segmentation scheme should reduce the edge error to less than 4% in the actual T_1 map (should be more than 5% using traditional segmentation method). Simulations suggested that the estimation error in K^{trans} was inversely proportional to the error in T_1 in a one-to-one ratio approximately. Therefore, the T_1 uncertainty should lead to about 2% K^{trans} uncertainty on average and 4% K^{trans} uncertainty at the edges. Previous studies have reported larger K^{trans} error due to error in T_1 [45,46]. However, these studies computed the T_1 error based on VFA T_1 mapping. In fact, 3D LL acquisition was shown to be more reproducible than 3D VFA [98]. Application of the proposed 3D LL modifications can therefore reduce the uncertainty in K^{trans}.

Coarse temporal resolution can increase the uncertainty in the calculated pharmacokinetic parameters [19-21]. In this work, a view sharing acquisition based on the elliptical 3D TRICKS method was implemented to increase the DCE-MRI sampling rate. In addition to the increased sampling rate, simulations in this work have shown that the view sharing technique can also reduce noise in the images. As shown in in this work (see Fig. 4.2) and previously reported in [20], data in the early post-contrast phase has the greatest impact on the pharmacokinetic parameters estimation. Unfortunately, the error in image intensity is highest in the early post-contrast period. The k-space normalization method was developed to reduce these reconstruction artifacts. It is shown that error in the early post-contrast phase can be reduced with application of the normalization factor. Consequently, this proposed view sharing

acquisition method with k-space normalization has the potential to provide low noise, high temporal resolution images with reduced artifacts.

Simulations in this study showed that noise in the DCE-MRI data could lead to substantial error in pharmacokinetic parameters. At high K^{trans}, the estimated K^{trans} error in a voxel was similar to that reported in [45]. But as the K^{trans} value decreased, the accuracy of K^{trans} estimation also decreased due to decline in CNR. After SCI, the permeability of the BSCB was still relatively low compared to non-CNS vasculature. This low permeability could lead to more than 10% error in K^{trans} as shown by the simulations. A local search clustering algorithm was developed to cluster relative intensity change-time curves into segments to improve the apparent CNR while maintaining the heterogeneity in the tissue uptake. The clustered segments were shown to reduce estimation error of the pharmacokinetic parameters compared to pixel-by-pixel or user-defined ROI analysis.

Finally, all the methods developed in this thesis for DCE-MRI were applied to in vivo investigation of BSCB permeability in experimental SCI. Multiple studies have assessed the post-SCI BSCB permeability using DCE-MRI because of its importance in probing the secondary injury [4,8,9,53,64,81]. However, in these published studies, the intrinsic T_1 was not measured and a universal T_1 was applied to compute tracer concentration. In addition, many of these studies used 2D acquisition. In contrast, the current experiments acquired T_1 map during each DCE-MRI section and all data were performed using 3D acquisition. DCE-MRI data were clustered to reduce noise while preserving the spatial heterogeneity. By applying these new techniques, the current experiment should provide more accurate results in DCE-MRI.

6.2 Future Directions

The temporal resolution in the current 3D DCE-MRI acquisition was 40 sec even with the application of view sharing technique. In principle, faster sampling rates can be achieved at the expense of spatial resolution. However, reduced matrix size will lead to truncation artifact that is especially prominent in the post-contrast images. Moreover, a previous study has also suggested that poor spatial resolution would degrade the estimation of the pharmacokinetic parameters [19]. Future improvements in the temporal resolution are possible. For example, the introduction of compressed sensing [99] provides a framework for sparse data sampling, thus improving the temporal resolution. Multiple studies have shown the effectiveness of constrained iterative reconstruction in MRI using the compressed sensing technique [100-102]. Application of compressed sensing to DCE-MRI can potentially improve the temporal resolution even further. In addition, it is possible to incorporate concentration-time curve clustering into the constraint of iterative reconstruction. This can potentially reduce noise without compromising spatial resolution.

In future, a through longitudinal study of BSCB permeability can be performed using the proposed techniques. A more accurate quantitative result can advance our understanding of the temporal and spatial evolution of BSCB permeability after SCI.

Appendix

Derivation of the Transverse Magnetization in a Look-Locker Acquisition

A LL sequence is composed of an inversion pulse γ followed by a series of small flip angles α to acquire the SPGR images. Let M_n^- be the longitudinal magnetization right before the nth α pulse after the γ pulse and M_n^+ be the longitudinal magnetization right after the nth α pulse, then:

$$M_n^+(0) = M_n^- \cos \alpha \qquad (A1.1)$$

The $(n + 1)^{\text{th}}$ pulse is applied at time τ after the nth pulse, so:

$$M_n^+(\tau) = M_0\left(1 - e^{-\tau/T_1}\right) + M_n^- \cos \alpha \, e^{-\tau/T_1} = M_{n+1}^- \qquad (A1.2)$$

Let N_{tot} be the total number of α pulses applied after each inversion, and M_γ^- be the longitudinal magnetization right before the γ pulse. The γ pulse is applied at time t_r after the last α pulse (N_{tot}) is applied, so:

$$M_\gamma^- = M_{N_{\text{tot}}}^+(t_r) = M_0\left(1 - e^{-t_r/T_1}\right) + M_{N_{\text{tot}}}^- \cos \alpha \, e^{-t_r/T_1} \qquad (A1.3)$$

The magnetization after the γ pulse would be:

$$M_\gamma^+(0) = M_\gamma^- \cos \gamma = \left[M_0\left(1 - e^{-t_r/T_1}\right) + M_{N_{\text{tot}}}^- \cos \alpha \, e^{-t_r/T_1}\right] \cos \gamma \qquad (A1.4)$$

Notice that Eq. A1.4 also holds in saturation recovery sequence where γ is 90° instead of 180°. The first α pulse is applied at time t_d after the γ pulse, therefore the longitudinal magnetization right before the first α pulse would be:

$$M_1^- = M_0\left(1 - e^{-t_d/T_1}\right) + M_\gamma^- \cos \gamma \, e^{-t_d/T_1} \qquad (A1.5)$$

The following simplification is made:

$$E\tau = \exp(-\tau/T_1)$$
$$Ed = \exp(-t_d/T_1)$$
$$Er = \exp(-t_r/T_1)$$

So, the magnetization right before the nth α pulse would be:

$$M_n^- = M_0(1 - E\tau)\left[1 + \cos \alpha \, E\tau + (\cos \alpha \, E\tau)^2 + \cdots + (\cos \alpha \, E\tau)^{n-2}\right]$$
$$+ \left[M_0(1 - Ed) + M_\gamma^- \cos \gamma \, Ed\right](\cos \alpha \, E\tau)^{n-1} \qquad (A1.6)$$

The series in the first term can be summed and Eq. A1.6 would yield:

$$M_n^- = M_0(1 - E\tau)\left[\frac{1 - (\cos \alpha \, E\tau)^{n-1}}{1 - \cos \alpha \, E\tau}\right] + \left[M_0(1 - Ed) + M_\gamma^- \cos \gamma \, Ed\right](\cos \alpha \, E\tau)^{n-1} \qquad (A1.7)$$

Combining Eq. A1.3 with Eq. A1.6, M_γ^- under steady state condition can be calculated:

$$M_\gamma^- = M_0(1 - Er)$$

$$+ \left\{ M_0(1 - E\tau) \left[\frac{1 - (\cos \alpha\, E\tau)^{N_{\text{tot}}-1}}{1 - \cos \alpha\, E\tau} \right] \right.$$

$$+ \left[M_0(1 - Ed) + M_\gamma^- \cos \gamma\, Ed \right](\cos \alpha\, E\tau)^{N_{\text{tot}}-1} \bigg\} \cos \alpha\, Er$$

$$\Rightarrow (1 - \cos \gamma\, Ed \cos \alpha\, Er(\cos \alpha\, E\tau)^{N_{\text{tot}}-1}) M_\gamma^-$$

$$= M_0 \left\{ (1 - Er) + (1 - E\tau) \left[\frac{1 - (\cos \alpha\, E\tau)^{N_{\text{tot}}-1}}{1 - \cos \alpha\, E\tau} \right] \right.$$

$$+ (1 - Ed)(\cos \alpha\, E\tau)^{N_{\text{tot}}-1} \cos \alpha\, Er \bigg\}$$

which leads to

$$M_\gamma^- = \frac{M_0}{1 - \cos \gamma\, Ed \cos \alpha\, Er(\cos \alpha\, E\tau)^{N_{\text{tot}}-1}} \left\{ (1 - Er) + (1 - E\tau) \left[\frac{1 - (\cos \alpha\, E\tau)^{N_{\text{tot}}-1}}{1 - \cos \alpha\, E\tau} \right] \right.$$

$$+ (1 - Ed)(\cos \alpha\, E\tau)^{N_{\text{tot}}-1} \cos \alpha\, Er \bigg\} \tag{A1.8}$$

Substituting M_γ^- in Eq. A1.8 into Eq. A1.7 yields:

$$M_n^- = M_0 \left\{ \frac{1 - E\tau}{1 - \cos \alpha\, E\tau} (1 - (\cos \alpha\, E\tau)^{n-1}) \right.$$

$$+ \frac{(\cos \alpha\, E\tau)^{n-1}}{1 - \cos \gamma\, Ed \cos \alpha\, Er(\cos \alpha\, E\tau)^{N_{\text{tot}}-1}} \left[1 - (1 - \cos \gamma)Ed - \cos \gamma\, EdEr \right. \tag{A1.9}$$

$$+ (1 - E\tau) \cos \gamma\, Ed \cos \alpha\, Er \left(\frac{1 - (\cos \alpha\, E\tau)^{N_{\text{tot}}-1}}{1 - \cos \alpha\, E\tau} \right) \bigg] \bigg\}$$

The transverse magnetization $M_\perp(n)$ is equal to $M_n^- \sin \alpha$, which is represented in Eq. 2.1.

Bibliography

1   O'Connor, J.P.B., A. Jackson, G.J.M. Parker, and G.C. Jayson. 2007. DCE-MRI biomarkers in the clinical evaluation of antiangiogenic and vascular disrupting agents. *British Journal of Cancer* 96(2):189-195.

2   Rijpkema, M., J.H.A.M. Kaanders, F.B.M. Joosten, A.J. van der Kogel, and A. Heerschap. 2001. Method for quantitative mapping of dynamic MRI contrast agent uptake in human tumors. *Journal of Magnetic Resonance Imaging* 14(4):457-463.

3   Barrett, T., H. Kobayashi, M. Brechbiel, and P.L. Choyke. 2006. Macromolecular MRI contrast agents for imaging tumor angiogenesis. *European Journal of Radiology* 60(3):353-366.

4   Bilgen, M., R. Abbe, and P.A. Narayana. 2001. Dynamic contrast-enhanced MRI of experimental spinal cord injury: In vivo serial studies. *Magnetic Resonance in Medicine* 45(4):614-622.

5   Kassner, A., T. Roberts, K. Taylor, F. Silver, and D. Mikulis. 2005. Prediction of Hemorrhage in Acute Ischemic Stroke Using Permeability MR Imaging. *American Journal of Neuroradiology* 26(9):2213-2217.

6   Larsson, H.B.W., A.E. Hansen, H.K. Berg, E. Rostrup, and O. Haraldseth. 2008. Dynamic contrast-enhanced quantitative perfusion measurement of the brain using T_1-weighted MRI at 3T. *Journal of Magnetic Resonance Imaging* 27(4):754-762.

7   Tofts, P.S., and A.G. Kermode. 1991. Measurement of the blood-brain barrier permeability and leakage space using dynamic MR imaging. 1. Fundamental concepts. *Magnetic Resonance in Medicine* 17(2):357-367.

8   Bilgen, M., B. Dogan, and P.A. Narayana. 2002. In vivo assessment of blood-spinal cord barrier permeability: serial dynamic contrast enhanced MRI of spinal cord injury. *Magnetic Resonance Imaging* 20(4):337-341.

9   Cohen, D.M., C.B. Patel, P. Ahobila-Vajjula, L.M. Sundberg, T. Chacko, S.J. Liu, and P.A. Narayana. 2009. Blood-spinal cord barrier permeability in experimental spinal cord injury: dynamic contrast-enhanced MRI. *NMR in Biomedicine* 22(3):332-341.

10   Buckley, D.L. 2002. Uncertainty in the analysis of tracer kinetics using dynamic contrast-enhanced T1-weighted MRI. *Magnetic Resonance in Medicine* 47(3):601-606.

11   Galbraith, S.M., M.A. Lodge, N.J. Taylor, G.J.S. Rustin, S. Bentzen, J.J. Stirling, and A.R. Padhani. 2002. Reproducibility of dynamic contrast-enhanced MRI in human muscle and tumours: comparison of quantitative and semi-quantitative analysis. *NMR in Biomedicine* 15(2):132-142.

12   Lavini, C., M.C. de Jonge, M.G.H. van de Sande, P.P. Tak, A.J. Nederveen, and M. Maas. 2007. Pixel-by-pixel analysis of DCE MRI curve patterns and an illustration of its application to the imaging of the musculoskeletal system. *Magnetic Resonance Imaging* 25(5):604-612.

13   Kety, S.S. 1951. The theory and applications of the exchange of inert gas at the lungs and tissues. *Pharmacological Reviews* 3(1):1-41.

14   Tofts, P.S., G. Brix, D.L. Buckley, J.L. Evelhoch, E. Henderson, M.V. Knopp, H.B.W. Larsson, T.-Y. Lee, N.A. Mayr, G.J.M. Parker, R.E. Port, J. Taylor, and R.M. Weisskoff. 1999. Estimating kinetic parameters from dynamic contrast-enhanced t1-weighted MRI of a diffusable tracer: Standardized quantities and symbols. *Journal of Magnetic Resonance Imaging* 10(3):223-232.

15   Larsson, H.B.W., M. Stubgaard, J.L. Frederiksen, M. Jensen, O. Henriksen, and O.B. Paulson. 1990. Quantitation of blood-brain barrier defect by magnetic resonance imaging and gadolinium-DTPA in patients with multiple sclerosis and brain tumors. *Magnetic Resonance in Medicine* 16(1):117-131.

16   Parker, G.J.M., C. Roberts, A. Macdonald, G.A. Buonaccorsi, S. Cheung, D.L. Buckley, A. Jackson, Y. Watson, K. Davies, and G.C. Jayson. 2006. Experimentally-derived functional form for a population-averaged high-temporal-resolution arterial input function for dynamic contrast-enhanced MRI. *Magnetic Resonance in Medicine* 56(5):993-1000.

17   Tofts, P.S. 1997. Modeling tracer kinetics in dynamic Gd-DTPA MR imaging. *Journal of Magnetic Resonance Imaging* 7(1):91-101.

18   Padhani, A.R., C. Hayes, S. Landau, and M.O. Leach. 2002. Reproducibility of quantitative dynamic MRI of normal human tissues. *NMR in Biomedicine* 15(2):143-153.

19   Aref, M., J.D. Handbury, J. Xiuquan Ji, S. Aref, and E.C. Wiener. 2007. Spatial and temporal resolution effects on dynamic contrast-enhanced magnetic resonance mammography. *Magnetic Resonance Imaging* 25(1):14-34.

20   Heisen, M., X. Fan, J. Buurman, N.A.W. van Riel, G.S. Karczmar, and B.M. ter Haar Romeny. 2010. The influence of temporal resolution in determining pharmacokinetic parameters from DCE-MRI data. *Magnetic Resonance in Medicine* 63(3):811-816.

21   Henderson, E., B.K. Rutt, and T.-Y. Lee. 1998. Temporal sampling requirements for the tracer kinetics modeling of breast disease. *Magnetic Resonance Imaging* 16(9):1057-1073.

22   Sharma, H.S. 2005. Pathophysiology of blood-spinal cord barrier in traumatic injury and repair. *Current Pharmaceutical Design* 11(11):1353-1389.

23   Popovich, P.G., P.J. Horner, B.B. Mullin, and B.T. Stokes. 1996. A quantitative spatial analysis of the blood-spinal cord barrier. I. Permeability changes after experimental spinal contusion injury. *Experimental Neurology* 142(2):258-275.

24   Markwardt, C.B. 2009. Non-linear Least-squares Fitting in IDL with MPFIT. *In* Astronomical Data Analysis Software and Systems XVIII.Quebec, Canada.

25 Steen, R.G., S.A. Gronemeyer, P.B. Kingsley, W.E. Reddick, J.S. Langston, and J.S. Taylor. 1994. Precise and accurate measurement of proton T1 in human brain in vivo: Validation and preliminary clinical application. *Journal of Magnetic Resonance Imaging* 4(5):681-691.

26 Christensen, K.A., D.M. Grant, E.M. Schulman, and C. Walling. 1974. Optimal determination of relaxation times of fourier transform nuclear magnetic resonance. Determination of spin-lattice relaxation times in chemically polarized species. *The Journal of Physical Chemistry* 78(19):1971-1977.

27 Kaldoudi, E., and S.C.R. Williams. 1993. Relaxation time measurements in NMR imaging. Part I: Longitudinal relaxation time. *Concepts in Magnetic Resonance* 5(3):217-242.

28 Parker, G.J.M., G.J. Barker, and P.S. Tofts. 2001. Accurate multislice gradient echo T1 measurement in the presence of non-ideal RF pulse shape and RF field nonuniformity. *Magnetic Resonance in Medicine* 45(5):838-845.

29 Venkatesan, R., W. Lin, and E.M. Haacke. 1998. Accurate determination of spin-density and T1 in the presence of RF-field inhomogeneities and flip-angle miscalibration. *Magnetic Resonance in Medicine* 40(4):592-602.

30 Cheng, H.L., and G.A. Wright. 2006. Rapid high-resolution T1 mapping by variable flip angles: accurate and precise measurements in the presence of radiofrequency field inhomogeneity. *Magnetic Resonance in Medicine* 55(3):566-574.

31 Deoni, S.C.L. 2007. High-resolution T1 mapping of the brain at 3T with driven equilibrium single pulse observation of T1 with high-speed incorporation of RF field inhomogeneities (DESPOT1-HIFI). *Journal of Magnetic Resonance Imaging* 26(4):1106-1111.

32 Look, D.C., and D.R. Locker. 1970. Time Saving in Measurement of NMR and EPR Relaxation Times. *Review of Scientific Instruments* 41(2):250-251.

33 Deichmann, R. 2005. Fast high-resolution T1 mapping of the human brain. *Magnetic Resonance in Medicine* 54(1):20-27.

34 Shah, N.J., M. Zaitsev, S. Steinhoff, and K. Zilles. 2001. A New Method for Fast Multislice T1 Mapping. *NeuroImage* 14(5):1175-1185.

35 Steinhoff, S., M. Zaitsev, K. Zilles, and N.J. Shah. 2001. Fast T1 mapping with volume coverage. *Magnetic Resonance in Medicine* 46(1):131-140.

36 Henderson, E., G. McKinnon, T.-Y. Lee, and B.K. Rutt. 1999. A fast 3D Look-Locker method for volumetric T1 mapping. *Magnetic Resonance Imaging* 17(8):1163-1171.

37 Deoni, S.C.L., B.K. Rutt, and T.M. Peters. 2003. Rapid combined T1 and T2 mapping using gradient recalled acquisition in the steady state. *Magnetic Resonance in Medicine* 49(3):515-526.

38   Gai, N.D., and J.A. Butman. 2009. Modulated repetition time look-locker (MORTLL): A method for rapid high resolution three-dimensional T1 mapping. *Journal of Magnetic Resonance Imaging* 30(3):640-648.

39   Nkongchu, K., and G. Santyr. 2005. An improved 3-D Look-Locker imaging method for T1 parameter estimation. *Magnetic Resonance Imaging* 23(7):801-807.

40   Warntjes, J.B.M., O. Dahlqvist, and P. Lundberg. 2007. Novel method for rapid, simultaneous T1, T2*, and proton density quantification. *Magnetic Resonance in Medicine* 57(3):528-537.

41   Wilman, A.H., and S.J. Riederer. 1997. Performance of an elliptical centric view order for signal enhancement and motion artifact suppression in breath-hold three-dimensional gradient echo imaging. *Magnetic Resonance in Medicine* 38(5):793-802.

42   Wendt, R.E. 2002. SpinWright: A Simulation of the Bloch Equations for Teaching Magnetic Resonance Principles. *In* 44th Annual Meeting, American Association of Physicists in Medicine.Montreal, Canada.

43   Nehrke, K. 2009. On the steady-state properties of actual flip angle imaging (AFI). *Magnetic Resonance in Medicine* 61(1):84-92.

44   Yarnykh, V.L. 2007. Actual flip-angle imaging in the pulsed steady state: A method for rapid three-dimensional mapping of the transmitted radiofrequency field. *Magnetic Resonance in Medicine* 57(1):192-200.

45   Dale, B.M., J.A. Jesberger, J.S. Lewin, C.M. Hillenbrand, and J.L. Duerk. 2003. Determining and optimizing the precision of quantitative measurements of perfusion from dynamic contrast enhanced MRI. *Journal of Magnetic Resonance Imaging* 18(5):575-584.

46   Haacke, E.M., L.F. Cristina, G. Ramtilak, C. Carlo, A.-B. Areen, S. Krithivasan, L. Meng, L. Zahid, D. Zach, S. Vivek, L. Tao, T. Vidya, K. Rajesh, J. Jing, and N. Jaladhar. 2007. New algorithm for quantifying vascular changes in dynamic contrast-enhanced MRI independent of absolute T1 values. *Magnetic Resonance in Medicine* 58(3):463-472.

47   Blüml, S., L.R. Schad, B. Stepanow, and W.J. Lorenz. 1993. Spin-lattice relaxation time measurement by means of a TurboFLASH technique. *Magnetic Resonance in Medicine* 30(3):289-295.

48   Cunningham, C.H., J.M. Pauly, and K.S. Nayak. 2006. Saturated double-angle method for rapid B_1+ mapping. *Magnetic Resonance in Medicine* 55(6):1326-1333.

49   Stollberger, R., and P. Wach. 1996. Imaging of the active B1 field in vivo. *Magnetic Resonance in Medicine* 35(2):246-251.

50   Wang, D., S. Zuehlsdorff, and A.C. Larson. 2009. Rapid 3D radiofrequency field mapping using catalyzed double-angle method. *NMR in Biomedicine* 22(8):882-890.

51 Ogg, R.J., and P.B. Kingsley. 2004. Optimized precision of inversion-recovery T1 measurements for constrained scan time. *Magnetic Resonance in Medicine* 51(3):625-630.

52 Lüdemann, L., W. Grieger, R. Wurm, P. Wust, and C. Zimmer. 2005. Quantitative measurement of leakage volume and permeability in gliomas, meningiomas and brain metastases with dynamic contrast-enhanced MRI. *Magnetic Resonance Imaging* 23(8):833-841.

53 Tatar, I., C.-t.P. Chou, M. Mokhtar Desouki, H. El Sayed, and M. Bilgen. 2009. Evaluating regional blood spinal cord barrier dysfunction following spinal cord injury using longitudinal dynamic contrast-enhanced MRI. *BMC Medical Imaging* 9(1):1-15.

54 Yankeelov, T.E., J.J. Luci, M. Lepage, R. Li, L. Debusk, P.C. Lin, R.R. Price, and J.C. Gore. 2005. Quantitative pharmacokinetic analysis of DCE-MRI data without an arterial input function: a reference region model. *Magnetic Resonance Imaging* 23(4):519-529.

55 Singh, A., M. Haris, D. Rathore, A. Purwar, M. Sarma, G. Bayu, N. Husain, R.K.S. Rathore, and R.K. Gupta. 2007. Quantification of physiological and hemodynamic indices using T1 dynamic contrast-enhanced MRI in intracranial mass lesions. *Journal of Magnetic Resonance Imaging* 26(4):871-880.

56 Kuribayashi, H., D.P. Bradley, D.R. Checkley, P.L. Worthington, and J.J. Tessier. 2004. Averaging Keyhole Pulse Sequence with Presaturation Pulses and EXORCYCLE Phase Cycling for Dynamic Contrast-Enhanced MRI. *Magnetic Resonance in Medical Sciences* 3(4):207-210.

57 Song, H.K., and L. Dougherty. 2004. Dynamic MRI with projection reconstruction and KWIC processing for simultaneous high spatial and temporal resolution. *Magnetic Resonance in Medicine* 52(4):815-824.

58 Jones, R.A., O. Haraldseth, T.B. Müller, P.A. Rinck, and A.N. Øksendal. 1993. K-space substitution: A novel dynamic imaging technique. *Magnetic Resonance in Medicine* 29(6):830-834.

59 Van Vaals, J.J., M.E. Brummer, W. Thomas Dixon, H.H. Tuithof, H. Engels, R.C. Nelson, B.M. Gerety, J.L. Chezmar, and J.A. Den Boer. 1993. "Keyhole" method for accelerating imaging of contrast agent uptake. *Journal of Magnetic Resonance Imaging* 3(4):671-675.

60 Madore, B., G.H. Glover, and N.J. Pelc. 1999. Unaliasing by Fourier-encoding the overlaps using the temporal dimension (UNFOLD), applied to cardiac imaging and fMRI. *Magnetic Resonance in Medicine* 42(5):813-828.

61 Kozerke, S., J. Tsao, R. Razavi, and P. Boesiger. 2004. Accelerating cardiac cine 3D imaging using k-t BLAST. *Magnetic Resonance in Medicine* 52(1):19-26.

62 Tsao, J., P. Boesiger, and K.P. Pruessmann. 2003. k-t BLAST and k-t SENSE: Dynamic MRI with high frame rate exploiting spatiotemporal correlations. *Magnetic Resonance in Medicine* 50(5):1031-1042.

63   Korosec, F.R., R. Frayne, T.M. Grist, and C.A. Mistretta. 1996. Time-resolved contrast-enhanced 3D MR angiography. *Magnetic Resonance in Medicine* 36(3):345-351.

64   Bilgen, M., and P.A. Narayana. 2001. A pharmacokinetic model for quantitative evaluation of spinal cord injury with dynamic contrast-enhanced magnetic resonance imaging. *Magnetic Resonance in Medicine* 46(6):1099-1106.

65   Mussurakis, S., D.L. Buckley, and A. Horsman. 1997. Dynamic MRI of Invasive Breast Cancer: Assessment of Three Region-of-Interest Analysis Methods. *Journal of Computer Assisted Tomography* 21(3):431-438.

66   Guo, J.-Y., and W.E. Reddick. 2009. DCE-MRI pixel-by-pixel quantitative curve pattern analysis and its application to osteosarcoma. *Journal of Magnetic Resonance Imaging* 30(1):177-184.

67   Chen, W., M.L. Giger, U. Bick, and G.M. Newstead. 2006. Automatic identification and classification of characteristic kinetic curves of breast lesions on DCE-MRI. *Medical Physics* 33(8):2878-2887.

68   Stoutjesdijk, M.J., J. Veltman, H. Huisman, N. Karssemeijer, J.O. Barentsz, J.G. Blickman, and C. Boetes. 2007. Automated analysis of contrast enhancement in breast MRI lesions using mean shift clustering for ROI selection. *Journal of Magnetic Resonance Imaging* 26(3):606-614.

69   Castellani, U., M. Cristiani, A. Daducci, P. Farace, P. Marzola, V. Murino, and A. Sbarbati. 2009. DCE-MRI data analysis for cancer area classification. *Methods of Information in Medicine* 48(3):248-253.

70   Nattkemper, T.W., and A. Wismüller. 2005. Tumor feature visualization with unsupervised learning. *Medical Image Analysis* 9(4):344-351.

71   Jackson, A., G.C. Jayson, K.L. Li, X.P. Zhu, D.R. Checkley, J.J.L. Tessier, and J.C. Waterton. 2003. Reproducibility of Quantitative Dynamic Contrast-Enhanced MRI in Newly Presenting Glioma. *British Journal of Radiology* 76(903):153-162.

72   Beattie, M.S., G.E. Hermann, R.C. Rogers, J.C. Bresnahan, and G.D.a.S.R. L. McKerracher. 2002. Chapter 4 Cell death in models of spinal cord injury. *In* Progress in Brain Research. Elsevier. 37-47.

73   Bilgen, M., R. Abbe, S.-J. Liu, and P.A. Narayana. 2000. Spatial and temporal evolution of hemorrhage in the hyperacute phase of experimental spinal cord injury: In vivo magnetic resonance imaging. *Magnetic Resonance in Medicine* 43(4):594-600.

74   Dumont, R.J., D.O. Okonkwo, S. Verma, R.J. Hurlbert, P.T. Boulos, D.B. Ellegala, and A.S. Dumont. 2001. Acute Spinal Cord Injury, Part I: Pathophysiologic Mechanisms. *Clinical Neuropharmacology* 24(5):254-264.

75   McDonald, J.W., and C. Sadowsky. 2002. Spinal-cord injury. *The Lancet* 359(9304):417-425.

76   Pan, W., A.J. Kastin, R.L. Bell, and R.D. Olson. 1999. Upregulation of tumor necrosis factor alpha transport across the blood-brain barrier after acute compressive spinal cord injury. *Journal of Neuroscience* 19(9):3649-3655.

77   Pan, W., W.A. Banks, and A.J. Kastin. 1997. Blood-brain barrier permeability to ebiratide and TNF in acute spinal cord injury. *Experimental Neurology* 146(2):367-373.

78   Banks, W.A., A.J. Kastin, and A. Arimura. 1998. Effect of Spinal Cord Injury on the Permeability of the Blood-Brain and Blood-Spinal Cord Barriers to the Neurotropin PACAP. *Experimental Neurology* 151(1):116-123.

79   Hausmann, O.N. 2003. Post-traumatic inflammation following spinal cord injury. *Spinal Cord* 41(7):369-378.

80   Jaeger, C.B., and A.R. Blight. 1997. Spinal Cord Compression Injury in Guinea Pigs: Structural Changes of Endothelium and Its Perivascular Cell Associations after Blood-Brain Barrier Breakdown and Repair. *Experimental Neurology* 144(2):381-399.

81   Patel, C.B., D.M. Cohen, P. Ahobila-Vajjula, L.M. Sundberg, T. Chacko, and P.A. Narayana. 2009. Effect of VEGF Treatment on the Blood-Spinal Cord Barrier Permeability in Experimental Spinal Cord Injury: Dynamic Contrast-Enhanced Magnetic Resonance Imaging. *Journal of Neurotrauma* 26(7):1005-1016.

82   Sundberg, L.M., J.J. Herrera, and P.A. Narayana. 2010. In Vivo Longitudinal MRI and Behavioral Studies in Experimental Spinal Cord Injury. *Journal of Neurotrauma* 27(10):1753-1767.

83   Sundberg, L.M., J.J. Herrera, and P.A. Narayana. 2011. Effect of Vascular Endothelial Growth Factor Treatment in Experimental Traumatic Spinal Cord Injury: In Vivo Longitudinal Assessment. *Journal of Neurotrauma* 28(4):565-578.

84   Laurent, S., L.V. Elst, and R.N. Muller. 2006. Comparative study of the physicochemical properties of six clinical low molecular weight gadolinium contrast agents. *Contrast Media & Molecular Imaging* 1(3):128-137.

85   Rohrer, M., H. Bauer, J. Mintorovitch, M. Requardt, and H.-J. Weinmann. 2005. Comparison of Magnetic Properties of MRI Contrast Media Solutions at Different Magnetic Field Strengths. *Investigative Radiology* 40(11):715-724.

86   Dobre, M.C., K.m. UÄŸurbil, and M. Marjanska. 2007. Determination of blood longitudinal relaxation time (T1) at high magnetic field strengths. *Magnetic Resonance Imaging* 25(5):733-735.

87   Thomson, D.J. 1982. Spectrum estimation and harmonic analysis. *Proceedings of the IEEE* 70(9):1055-1096.

88   Mitra, P.P., and B. Pesaran. 1999. Analysis of Dynamic Brain Imaging Data. *Biophysical Journal* 76(2):691-708.

89   de Graaf, R.A., P.B. Brown, S. McIntyre, T.W. Nixon, K.L. Behar, and D.L. Rothman. 2006. High magnetic field water and metabolite proton T1 and T2 relaxation in rat brain in vivo. *Magnetic Resonance in Medicine* 56(2):386-394.

90   Noble, L.J., and J.R. Wrathall. 1989. Distribution and time course of protein extravasation in the rat spinal cord after contusive injury. *Brain Research* 482(1):57-66.

91   Gordh, T., H. Chu, and H.S. Sharma. 2006. Spinal nerve lesion alters blood-spinal cord barrier function and activates astrocytes in the rat. *Pain* 124(1-2):211-221.

92   Sharma, H.S., Y. Olsson, F. Nyberg, and P.K. Dey. 1993. Prostaglandins modulate alterations of microvascular permeability, blood flow, edema and serotonin levels following spinal cord injury: An experimental study in the rat. *Neuroscience* 57(2):443-449.

93   Deo, A.A., R.J. Grill, K.M. Hasan, and P.A. Narayana. 2006. In vivo serial diffusion tensor imaging of experimental spinal cord injury. *Journal of Neuroscience Research* 83(5):801-810.

94   Baldwin, S.A., R. Broderick, D. Osbourne, G. Waeg, D.A. Blades, and S.W. Scheff. 1998. The presence of 4-hydroxynonenal/protein complex as an indicator of oxidative stress after experimental spinal cord contusion in a rat model. *Journal of Neurosurgery* 88(5):874-883.

95   Aimone, J.B., J.L. Leasure, V.M. Perreau, and M. Thallmair. 2004. Spatial and temporal gene expression profiling of the contused rat spinal cord. *Experimental Neurology* 189(2):204-221.

96   Zimmerman, J.R., and W.E. Brittin. 1957. Nuclear Magnetic Resonance Studies in Multiple Phase Systems: Lifetime of a Water Molecule in an Adsorbing Phase on Silica Gel. *The Journal of Physical Chemistry* 61(10):1328-1333.

97   Parker, D.L., V. Smith, P. Sheldon, L.E. Crooks, and L. Fussell. 1983. Temperature distribution measurements in two-dimensional NMR imaging. *Medical Physics* 10(3):321-325.

98   Siversson, C., C.-J. Tiderius, P. Neuman, L. Dahlberg, and J. Svensson. 2010. Repeatability of T1-quantification in dGEMRIC for three different acquisition techniques: Two-dimensional inversion recovery, three-dimensional look locker, and three-dimensional variable flip angle. *Journal of Magnetic Resonance Imaging* 31(5):1203-1209.

99   Donoho, D.L. 2006. Compressed sensing. *Information Theory, IEEE Transactions on* 52(4):1289-1306.

100   Adluru, G., T. Tasdizen, M.C. Schabel, and E.V.R. DiBella. 2010. Reconstruction of 3D dynamic contrast-enhanced magnetic resonance imaging using nonlocal means. *Journal of Magnetic Resonance Imaging* 32(5):1217-1227.

101   Gamper, U., P. Boesiger, and S. Kozerke. 2008. Compressed sensing in dynamic MRI. *Magnetic Resonance in Medicine* 59(2):365-373.

102   Lustig, M., D. Donoho, and J.M. Pauly. 2007. Sparse MRI: The application of compressed sensing for rapid MR imaging. *Magnetic Resonance in Medicine* 58(6):1182-1195.

Vita

Cheukkai Hui (許卓佳), the son of Yiu Fun Hui (許耀勳) and Tung Fung Cheng (鄭同放), was born in the city of Hong Kong on 28 December 1981. In primary school, he chose an old English name, Becket, as his English name. In winter 1998, he and his family moved to Tucson, Arizona to experience a new adventure in life. He entered the University of Arizona in 2000 and graduated in 2004 with a Bachelors of Science degree in Physics and Mathematics. In the same year, he entered the physics graduate program in the University of Texas at Austin. He spent three years there and worked in the UT Maya Muon Project led by Professor Roy Schwitters. He finished with his Master of Arts degree in Physics before moving to the University of Texas Health Science Center GSBS at Houston to study Medical Physics in 2007. In 2008, he joined the MR research group under the supervision of Professor Ponnada Narayana.

Permanent Email Address:
cheukkaihui@gmail.com